The Astrophysical Journal, 993:217 (43pp), 2025 November 10 https://doi.org/10.3847/1538-4357/ae0737

Excitation of Molecular Hydrogen in Seyferts: NGC 5506 and NGC 3081

Daniel E. Delaney[1,2], Erin K. S. Hicks[1,2], Lulu Zhang[3], Chris Packham[3], Ric Davies[4], Miguel Pereira Santaella[5], Enrica Bellocchi[6,7], Nancy A. Levenson[8], Steph Campbell[9], David J. Rosario[9], Houda Haidar[9], Cristina Ramos Almeida[10,11], Anelise Audibert[10,11], Claudio Ricci[12,13], Laura Hermosa Muñoz[14], Francoise Combes[15], Almudena Alonso-Herrero[14], Santiago García-Burillo[16], Federico Esposito[17,18], Ismael García-Bernete[19], Taro Shimizu[4], Martin Ward[20], Omaira Gonzalez Martin[21], Alvaro Labiano[22], Enrique Lopez-Rodriguez[23], Dimitra Rigopoulou[24,25], Marko Stalevski[26,27], Sebastian F. Hönig[28], Donaji Esparza-Arredondo[29], Takuma Izumi[30], Lindsay Fuller[3], and Daniel Rouan[31]
[1] Department of Physics, University of Alaska Fairbanks, AK 99775, USA
[2] Department of Physics and Astronomy, University of Alaska Anchorage, AK 99508, USA
[3] Department of Physics and Astronomy, The University of Texas at San Antonio, 1 UTSA Circle, San Antonio, TX 78249, USA
[4] Max Planck Institute for Extraterrestrial Physics (MPE), Giessenbachstr.1, 85748 Garching, Germany
[5] Instituto de Física Fundamental, CSIC, Calle Serrano 123, 28006 Madrid, Spain
[6] Departamento de Física de la Tierra y Astrofísica, Fac. de CC. Físicas, Universidad Complutense de Madrid, 28040 Madrid, Spain
[7] Instituto de Física de Partículas y del Cosmos IPARCOS, Fac. CC. Físicas, Universidad Complutense de Madrid, 28040 Madrid, Spain
[8] Space Telescope Science Institute, Baltimore, MD 21218, USA
[9] School of Mathematics, Statistics and Physics, Newcastle University, Newcastle upon Tyne, NE1 7RU, UK
[10] Instituto de Astrofísica de Canarias, Calle Vía Láctea, s/n, E-38205, La Laguna, Tenerife, Spain
[11] Departamento de Astrofísica, Universidad de La Laguna, E-38206, La Laguna, Tenerife, Spain
[12] Núcleo de Astronomía de la Facultad de Ingeniería, Universidad Diego Portales, Av. Ejército Libertador 441, Santiago, Chile
[13] Kavli Institute for Astronomy and Astrophysics, Peking University, Beijing 100871, People's Republic of China
[14] Centro de Astrobiología (CAB) CSIC-INTA, Camino Bajo del Castillo s/n, 28692 Villanueva de la Cañada, Madrid, Spain
[15] Observatoire de Paris, LUX, Collège de France, PSL Research University, CNRS, Sorbonne University, Paris, France
[16] Observatorio Astronómico Nacional (OAN-IGN)-Observatorio de Madrid, Alfonso XII, 3, 28014-Madrid, Spain
[17] Dipartimento di Fisica e Astronomia, Università degli Studi di Bologna, Via P. Gobetti 93/2, I-40129 Bologna, Italy
[18] Osservatorio di Astrofisica e Scienza dello Spazio (INAF-OAS), Via P. Gobetti 93/3, I-40129 Bologna, Italy
[19] Centro de Astrobiología (CAB), CSIC-INTA, Camino Bajo del Castillo s/n, E-28692 Villanueva de la Cañada, Madrid, Spain
[20] Centre for Extragalactic Astronomy, Department of Physics, Durham University, South Road, Durham, DH1 3LE, UK
[21] Instituto de Radioastronomía y Astrofísica (IRyA), Universidad Nacional Autónoma de México, Antigua Carretera a Pátzcuaro #8701, Colonia ExHda. San José de la Huerta, Morelia, Michoacán, México C.P. 58089, Mexico
[22] Telespazio UK for ESA, ESAC, Camino Bajo del Castillo s/n, 28692 Villanueva de la Cañada, Spain
[23] Kavli Institute for Particle Astrophysics & Cosmology (KIPAC), Stanford University, Stanford, CA 94305, USA
[24] Department of Physics, University of Oxford, Keble Road, Oxford, OX1 3RH, UK
[25] School of Sciences, European University Cyprus, Diogenes street, Engomi, 1516 Nicosia, Cyprus
[26] Astronomical Observatory, Volgina 7, 11060 Belgrade, Serbia
[27] Sterrenkundig Observatorium, Universiteit Gent, Krijgslaan 281-S9, Gent B-9000, Belgium
[28] Department of Physics & Astronomy, University of Southampton, Highfield, Southampton, SO171BJ, UK
[29] Instituto de Radioastronomía y Astrofísica (IRyA-UNAM), 3-72 (Xangari), 8701, Morelia, Mexico
[30] Department of Astronomy, School of Science, Graduate University for Advanced Studies (SOKENDAI), Mitaka, Tokyo 181-8588, Japan
[31] LESIA, Observatoire de Paris, Université PSL, CNRS, Sorbonne Université, Sorbonne Paris Citeé, 5 place Jules Janssen, F-92195 Meudon, France
Received 2025 April 16; revised 2025 September 9; accepted 2025 September 14; published 2025 November 6

Abstract

We utilize James Webb Space Telescope (JWST) Mid Infrared Instrument (MIRI) integral field unit observations to investigate the behavior and excitation of H_2 in the nearby Seyfert galaxies NGC 3081 and NGC 5506, both part of the Galactic Activity, Torus, and Outflow Survey (or GATOS). We compare population levels of the S(1) to S(8) rotational H_2 emission lines visible to JWST/MIRI spectroscopy to models assuming local thermodynamic equilibrium (LTE), in order to estimate the column density and thermal scaling of the molecular gas. For the nuclear regions, we incorporate Very Large Telescope Spectrograph for INtegral Field Observations in the Near Infrared (or VLT/SINFONI) *K*-band observations to estimate population levels for available rovibrational H_2 emission lines, and compare the resultant population curves to non-LTE radiative transfer models and shock modeling. We report a differing set of prominent active galactic nuclei (AGN)-driven excitation mechanisms between the two galaxies. For NGC 3081, we find that a non-LTE radiative transfer environment is adequate to explain observations of the nuclear region, indicating that the primary mode in which the AGN transfers excitation energy is likely irradiation. We estimate the extent of AGN photoionization along the ionization bicone to be ≈330 pc. In contrast, for NGC 5506, we find a shock scenario to be a more plausible excitation mechanism, a conclusion bolstered by an observed spatial correlation between higher-energy rotational

H_2 and [Fe II]$_{5.34\mu m}$ emission. In addition, we identify potential nuclear H_2 outflows resulting from an interaction between the ionization bicone and the rotational disk. By isolating the outflowing component of the H_2 emission, we estimate the warm molecular mass outflow rate to be 0.07 $M_\odot$ yr^{-1}.

Unified Astronomy Thesaurus concepts: AGN host galaxies (2017); Active galactic nuclei (16); Galaxy evolution (594); Galaxy circumnuclear disk (581); Molecular gas (1073)

1. Introduction

Active galactic nuclei (AGN) are the most luminous non-explosive objects observed in the Universe (e.g., R. C. Hickox & D. M. Alexander 2018). This immense luminosity is the result of mass accretion around the galaxies' central supermassive black holes (SMBHs). These energetic objects provide feedback from the growth of the SMBH to the rest of the galaxy, perturbing and influencing the material around the AGN (e.g., K. Wada 2012; C. Ramos Almeida & C. Ricci 2017). Radiative feedback and outflows (ionized, neutral, and molecular) from the AGN are thought to play an important role in galaxy evolution via the redistribution of material and the provision of excitation energy (S. Veilleux et al. 2005; A. C. Fabian 2012; S. Veilleux et al. 2013; C. Harrison et al. 2018). While it has become increasingly evident that AGN processes act as an important influence on galactic dynamics and evolution, the exact nature of their behavior and impacts of the AGN to the host have not been well constrained (C. Ramos Almeida & C. Ricci 2017; C. M. Harrison & C. Ramos Almeida 2024). AGN activity can act to expel molecular material out the galaxy and, it has been posited that star formation may be quenched by this mechanism (A. C. Fabian 2012; C. Cicone et al. 2014; C. Harrison et al. 2018). However, large-scale AGN studies suggest that while outflows may displace molecular material from the nuclear region (see, e.g., I. García-Bernete et al. 2021; C. Ramos Almeida et al. 2022; A. Audibert et al. 2025), that material is often reaccreted by the host galaxy and does not strictly quench star formation via gas removal. Instead, outflows have a more complex connection to galactic evolution, and can potentially enhance star formation (R. Davies et al. 2007; P. Esquej et al. 2013; C. Harrison 2017; S. L. Ellison et al. 2018; P. S. Bessiere & C. Ramos Almeida 2022; J. Molina et al. 2023). Nonetheless, this fountain-like churning of material has important implications for galactic evolution and, as such, detailed studies of molecular material in the central regions of AGN are warranted.

Hydrogen is the most abundant element in the Universe, and is therefore anticipated to account for the bulk of molecular material throughout the galactic structure. Emission tracing the presence and motion of molecular hydrogen acts as a tool to not only detect molecular gas outflows from the AGN, but also to assess the impacts of AGN activity on the galactic disk and other circumnuclear materials. In this context, spatially resolved observations in both the near- and mid-infrared (NIR and MIR) play a critical role in tracing the warm molecular gas circumnuclear to the AGN. With the advent of new observatories such as the James Webb Space Telescope (JWST), supplemented with existing ground-based observatories, we now have access to a suite of emission tracing warm and hot molecular gas at high spatial resolution with exceptional data quality (see, e.g., M. Pereira-Santaella et al. 2022; R. Davies et al. 2024; R. A. Riffel et al. 2025; D. Esparza-Arredondo et al. 2025; C. Ramos Almeida et al. 2025). In this study, we utilize integral field unit (IFU) observations from both space-based (JWST; J. P. Gardner et al. 2023; J. Rigby et al. 2023) and ground-based (the ESO's Very Large Telescope Spectrograph for INtegral Field Observations in the Near Infrared, or VLT/SINFONI; F. Eisenhauer et al. 2003) observatories to study the impacts of AGN activity on the molecular hydrogen in two nearby AGN: NGC 5506 and NGC 3081. We probe the circumnuclear gas to infer relevant AGN-driven excitation mechanisms and associated kinematics.

This work builds upon previous studies which aimed to understand AGN feedback, and more specifically the interactions between AGN outflows and the behavior of circumnuclear gas. These works are numerous and extend across a wide range of targets and focus on an array of AGN activities. Notably, S. García-Burillo et al. (2014), J. F. Gallimore et al. (2016), S. García-Burillo et al. (2016), M. Imanishi et al. (2018), A. Alonso-Herrero et al. (2019), S. García-Burillo et al. (2019), C. V. Impellizzeri et al. (2019), I. García-Bernete et al. (2021), S. García-Burillo et al. (2021), A. A. Alonso-Herrero et al. (2023), and F. Esposito et al. (2024) identified AGN molecular gas outflows across a variety of AGN, including the canonical NGC 1068. Additionally, R. Davies et al. (2014) and F. Esposito et al. (2024) identified potential interactions between outflows and ionization cones, and the rotational galactic disk. These studies also build upon previous works which used similar methods to investigate excitation and the influence of AGN on molecular gas. Notably, N. L. Zakamska (2010) investigated H_2 gas population levels in ultra-luminous infrared galaxies (ULIRGs). M. Pereira-Santaella et al. (2014), R. Davies et al. (2024), and A. Togi & J. Smith (2016) expanded these earlier studies to include a wider range of objects including low-ionization nuclear emission-line regions (LINERs) and Seyfert galaxies, and analyzed H_2 population levels in the nuclear and circumnuclear regions of AGN.

We organize this paper to first provide information on the sample selection and relevant background information for each target, followed by an overview of our methodology, and finally the results for each individual target. Section 2 highlights the sample selection process and provides background information on NGC 3081 and NGC 5506; in addition, an overview of the data collection and reduction procedure is provided in Section 3. The methodology used for analysis, including relevant equations and assumptions, is presented in Section 4. The analysis results are presented in Section 5 and organized to first present the distributions of molecular (Section 5.1) and ionized (Section 5.2) gas, followed by an analysis of H_2 population levels and excitation in Sections 5.4–5.5. Finally, we provide a summary of results and additional discussion in Section 6.

2. Sample Selection

The Galaxy Activity, Torus, and Outflow Survey (GATOS)[32] collaboration was awarded observing time on JWST to observe six nearby AGN in the MIR as part of the JWST Cycle 1 program 1670 (PI: T. Shimizu). This galaxy sample was selected from the 70 months Swift-BAT All-sky Hard X-ray

[32] More information regarding the GATOS collaboration and their ongoing research can be found at https://gatos.myportfolio.com/home.

Table 1
NGC 3081 and NGC 5506 Fundamental Parameters

Parameter	NGC 3081	NGC 5506	References
Host galaxy	(R)SAB(r)0/a	Sa peculiar	T. Caglar et al. (2020), S. García-Burillo et al. (2021)
Seyfert type	2	1.9/1i	S. García-Burillo et al. (2021)
Redshift	0.00802	0.00628	...
Distance	34 Mpc	26 Mpc	T. Caglar et al. (2020), F. Esposito et al. (2024)
Position angle	90°	265°	A. Schnorr-Müller et al. (2016), F. Esposito et al. (2024)
Inclination	<40°	80°	A. Schnorr-Müller et al. (2016), F. Esposito et al. (2024)
$\log[L_{AGN}/\mathrm{erg\ s^{-1}}]$	44.1	44.1	R. Davies et al. (2020)
$\log[L_{14-195\ keV}/\mathrm{erg\ s^{-1}}]$	42.8	43.2	A. Y. Lien et al. (2025)
$\log[M_{BH}/M_{\odot}]$	7.56 ± 0.8	7.3 ± 0.7	T. Caglar et al. (2020), J. Gofford et al. (2015)
$\log[N_H\ /\mathrm{cm^{-2}}]$	23.9	22.4	C. Ricci et al. (2017)
PA_{Out}	165°	22°	L. Zhang et al. (2024b), T. Fischer et al. (2013)
Ω_{Out}	30°	80°	A. Schnorr-Müller et al. (2016), T. Fischer et al. (2013)

Note. Redshift was calculated using the average offset of the centroid of S(1)-S(8) emission lines in the nuclear region.

Survey as targets of interest for constraining AGN outflow behavior (W. Baumgartner et al. 2013). These objects are local (distance <40 Mpc) and are of similar type (Seyfert 2 and 1.9/1i) and with similar bolometric luminosity; however, they span a range of outflow properties, making them an ideal sample for constraining the impacts of outflows (R. Davies et al. 2020). Since its acquisition, the GATOS JWST sample has been well utilized in the pursuit of the collaboration's goal to understand AGN dynamics, feedback, and outflows. Utilizing the full GATOS Cycle 1 sample, L. Zhang et al. (2024b) present a sample overview in which they examine the ionized gas distribution and kinematics. Numerous other works have been published studying the GATOS sample targets to explore water ice and silicate absorption features (I. García-Bernete et al. 2024), polycyclic aromatic hydrocarbon (PAH) features (I. García-Bernete et al. 2022; L. Zhang et al. 2024a), and polar dust emission (H. Haidar et al. 2024). AGN feeding and feedback has been explored in individual targets by A. A. Alonso-Herrero et al. (2023), L. Hermosa-Muñoz et al. (2024), and D. Esparza-Arredondo et al. (2025). R. Davies et al. (2024) and A. A. Alonso-Herrero et al. (2023) studied the impacts of AGN outflows to molecular gas in NGC 5728 and NGC 7172, respectively.

From the GATOS sample, we select NGC 3081 and NGC 5506 to investigate the impacts of AGN on H_2 excitation. These objects, similar in type, distance, and intrinsic X-ray luminosity, are of interest due to their different host-galaxy orientations and outflow properties. NGC 3081 is a more face-on galaxy, relative to the edge-on NGC 5506, and has an estimated ionized outflow rate roughly 5 times less than that of NGC 5506 (R. Davies et al. 2020). Previous work using JWST Medium Resolution Spectrometer (MRS) observations has highlighted the presence of AGN-related highly disturbed regions in three of the six objects within the GATOS Cycle 1 sample, including NGC 5506 though not NGC 3081 (L. Zhang et al. 2024b). These stark contrasts in outflow properties and the apparent AGN-induced disturbances to circumnuclear material in otherwise similar objects make them ideal targets for comparing the impacts of AGN on warm molecular gas.

2.1. NGC 3081

NGC 3081 is a relatively face-on barred lenticular galaxy with a Seyfert type 2 AGN. Its fundamental parameters are presented in Table 1. On a large scale, the morphology of NGC 3081 is often characterized by three outer resonance rings, and on a smaller scale (the relevant field of view to this study) an elongated nuclear ring (R. Buta & G. B. Purcell 1998; R. J. Buta et al. 2004). The inner nuclear ring has a major axis of ≈12″ and contains two star-forming spiral arms which connect to a weak nuclear bar (R. Buta & G. B. Purcell 1998; P. Ferruit et al. 2000; R. J. Buta et al. 2004). S. Eguchi et al. (2011), through a detailed X-ray spectral analysis, suggested NGC 3081 resembles a deeply buried AGN (shrouded in a very geometrically thick torus with a small opening angle; Y. Ueda et al. 2007) with an opening angle of ≈15°. S. García-Burillo et al. (2024) investigated the central concentration index (CCI ≡ log $[\Sigma^{H_2}_{50pc}/\Sigma^{H_2}_{200pc}]$) of cool molecular gas using $CO(2–1)_{230.5GHz}$ emission and the concentration index of hot molecular gas (HCI ≡ log $[\Sigma^{hot}_{50pc}/\Sigma^{hot}_{200pc}]$) using H_2 1–0 S(1) emission for nearby Seyfert-type galaxies. NGC 3081 was shown to have a nuclear deficiency of both cold and hot molecular gas relative to other Seyfert galaxies. Additionally, NGC 3081 has been shown to contain a weak, compact, symmetric (with some evidence of elongation) nuclear radio signal, which exhibited a decrease in nuclear radio flux over a 7 yr period from 1992 to 1999 during which the target was observed (R. Morganti et al. 1999; N. M. Nagar et al. 1999; I. M. Mutie et al. 2024). Through investigations of $[Fe\ VII]_{0.6087\mu m}$ and $[Fe\ X]_{0.6375\mu m}$ emission, A. Rodríguez-Ardila et al. (2025) showed the coronal line region of NGC 3081 extends to hundreds of parsecs (emission detections out to 472 pc and 365 pc, respectively) and is aligned with the radio jet.

AGN feeding and outflows were studied by P. Ferruit et al. (2000), J. Ruiz et al. (2005), and A. Schnorr-Müller et al. (2016) utilizing $[O\ III]_{5007Å}$ emission to trace outflows. The biconical outflow region extends ≈4″ from north to south through the nucleus (A. Schnorr-Müller et al. 2016). A. Schnorr-Müller et al. (2016) estimated the ionized mass outflow rate to be between (1.9–6.9) × 10^{-3} $M_{\odot}$ yr^{-1}, and established an upper limit for the mass inflow of ionized gas of 1.3 × 10^{-3} $M_{\odot}$ yr^{-1}. Similarly, R. Davies et al. (2020) utilized optical and NIR observations from the VLT and estimated the ionized mass outflow rate to be 0.04 $M_{\odot}$ yr^{-1}. Most recently, L. Zhang et al. (2024b) utilized $[Ne\ V]_{14.322\mu m}$ emission (I. García-Bernete et al. 2024) to estimate the ionized mass outflow rate in the range of 0.007–0.03 $M_{\odot}$ yr^{-1}.

2.2. NGC 5506

NGC 5506 is a peculiar edge-on spiral galaxy containing a Seyfert type 1.9/1i AGN (S. García-Burillo et al. 2021).[33] Its fundamental parameters are presented in Table 1. Observations of the nuclear region have revealed a ionization bicone, both ionized and molecular outflows, and a narrow-line region suggesting the AGN to be relatively young and highly accreting (A. Tarchi et al. 2011; S. García-Burillo et al. 2021; Q. Salomé et al. 2023; F. Esposito et al. 2024). Additionally, NGC 5506 has been shown to contain a subparsec radio jet with a bend aligning itself to the larger-scale outflow (A. Kinney et al. 2000; A. Roy et al. 2001). The geometry of the disk and ionization bicone was modeled by T. Fischer et al. (2013), who determined the extent of the bicone to be roughly 5″ north to south, nearly perpendicular to the disk. F. Esposito et al. (2024) indicated that there is likely interaction between the rotational disk and a portion of the ionization bicone to the north of the AGN. As a result, the ionized and molecular gas are weakly coupled (as described by C. Ramos Almeida et al. 2022) and molecular material may be exported from the nuclear region via the biconical ionized outflow. In addition, L. Zhang et al. (2024b) reported highly disturbed gaseous regions present to the northwest of the nucleus, consistent with a potential interaction between the AGN-driven radio jet and ambient interstellar medium (ISM) around the AGN. The line-of-sight geometry of NGC 5506 is well depicted in Figure 18 of F. Esposito et al. (2024).

Previous studies have utilized Hubble Space Telescope (HST) observations of $[\mathrm{O\ III}]_{5007\text{Å}}$ and the Hα-[N II] complex to estimate the velocity of ionized outflows to be in the range of 400–792 km s^{-1}, oriented roughly north–south (R. Maiolino et al. 1994; T. Fischer et al. 2013; R. Davies et al. 2020; F. Esposito et al. 2024). The mass outflow rate has been previously measured using optical and NIR observations (0.21 $M_\odot$ yr^{-1}; R. Davies et al. 2020); in the NIR, the ionized mass outflow rate was reported to range from 0.11 to 12.49 $M_\odot$ yr^{-1} (M. Bianchin et al. 2022; R. A. Riffel et al. 2023). The highest of these outflow rates, estimated by M. Bianchin et al. (2022), assumed a notably low mass density for ionized hydrogen (500 cm^{-3}). For an assumed higher mass density of ionized hydrogen (10,000 cm^{-3}), M. Bianchin et al. (2022) estimated the mass outflow rate to be 0.062 $M_\odot$ yr^{-1}, i.e., more consistent with other studies (R. Davies et al. 2020; R. A. Riffel et al. 2023). Minimizing effects from dust extinction, L. Zhang et al. (2024b) estimated a rate in the range of 0.12–0.28 $M_\odot$ yr^{-1}. R. A. Riffel et al. (2023) used K-band observations from the Gemini Near-Infrared Field Spectrograph and from H_2 1–0 S(1) observations to estimate a hot molecular mass outflow rate on the order of 0.3×10^{-3} $M_\odot$ yr^{-1}. The molecular gas was studied by both S. García-Burillo et al. (2021) and F. Esposito et al. (2024), who utilized $\mathrm{CO(2–1)}_{230.5\mathrm{GHz}}$ and $\mathrm{CO(3–2)}_{345.8\mathrm{GHz}}$ observations from the Atacama Large Millimeter Array (ALMA) and imaging data from HST. S. García-Burillo et al. (2021) found indications of a ring-like morphology, and clear evidence of molecular outflows with radial velocities on the order of 50–100 km s^{-1}.

Additionally, S. García-Burillo et al. (2021) and S. García-Burillo et al. (2024) investigated the CCI and HCI using observations of CO emission from ALMA and H_2 1–0 S(1) emission from VLT/SINFONI, respectively. NGC 5506 presented a notably low CCI, indicating a nuclear deficiency of cold molecular gas relative to other galaxies within the GATOS sample. In contrast to this, the HCI for NGC 5506 indicated no deficiency of hot molecular gas in the nuclear region relative to other Seyfert galaxies. Using the CO(3–2) emission between 0.″4 and 5″, F. Esposito et al. (2024) calculated a molecular mass outflow velocity of 25.6 ± 9.4 km s^{-1} with an average rate of $\dot{M}_{\mathrm{out}}^{\mathrm{mol}} = 8 \pm 3\ M_\odot\ \mathrm{yr}^{-1}$. At smaller radii, F. Esposito et al. (2024) reported a negative velocity for the molecular gas, potentially indicative of inflowing material from the rotating molecular disk.

[33] This object is classified as "S1i" since it shows broad Paschen lines in the infrared, according to the nomenclature of M.-P. Véron-Cetty & P. Véron (2006).

3. Data Collection and Reduction

This study utilizes JWST MIR IFU observations, further supplemented by NIR IFU observations from the VLT. The Mid Infrared Instrument (MIRI; G. H. Rieke et al. 2015) on board JWST, capable of performing medium-resolution spectroscopy (M. Wells et al. 2015; I. Argyriou et al. 2023), is optimized for spectrographic observations in the range of 4.9–27.9 μm (M. Wells et al. 2015; I. Argyriou et al. 2023). The MRS instrument utilizes four different channels to cover the full spectral range. The resolution and field of view (FOV) varies for each channel, with the smallest FOV being 3.″2 × 3.″7 (Channel 1) and the coarsest having a FOV of 6.″6 × 7.″7. NGC 3081 was observed by JWST/MIRI medium-resolution spectroscopy on 2023 December 9 with a total exposure time of 4586.9 s. A four-point 2 × 2 dither pattern was used for coverage of the nuclear region, and the extent of the widest FOV includes some of the nuclear ring. NGC 5506 was observed by JWST/MIRI medium-resolution spectroscopy on 2023 July 25 with a total exposure time of 2197.832 s. Due to the high position angle of the galaxy, an eight-point linear mosaic dither pattern was used to observe along the disk of the galaxy. Each MRS data cube was processed via the standard calibration pipeline (version 1.11.4). Prior to background subtraction, additional steps were added to identify and mask hot and cold pixels not identified by the standard pipeline. After masking, a linear interpolation was used in an attempt to recover flux values in these pixels. The data reduction process is described in detail in Appendix A of M. Pereira-Santaella et al. (2022) and I. García-Bernete et al. (2024).

NIR data were obtained via the SINFONI instrument on board VLT. SINFONI observations were carried out with a FOV of 3″× 3″ and a pixel size of 0.″05 (F. Eisenhauer et al. 2003). VLT/SINFONI observed the nuclear region of NGC 3081 (ESO program ID 098.B-0028(A), 2017 March 14; PI: R. Davies) and NGC 5506 (ESO program ID 093.B-0057(B), 2015 March 12; PI: R. Davies) with a 60 and 30 minutes exposure time, respectively. VLT/SINFONI NIR data were reduced using SPRED, a custom package developed at the Max Planck Institute for Extraterrestrial Physics for analysis of SINFONI data (R. Abuter et al. 2006). All standard reduction steps needed for NIR spectra as well as additional routines necessary to reconstruct the data cubes were applied. We further applied routines designed to improve the subtraction of hydroxyl radical sky emission lines, following the approach outlined in R. Davies (2007). Observations of both objects utilized the instrument's adaptive optics system for improved data quality.

Table 2
NGC 3081 Measured Line Flux for the H_2 0–0 S(1) through S(8) Emission for Each Aperture of Interest

Emission Line	λ_{rest} (μm)	Flux (10^{-16}erg s^{-1} cm^{-2})					
		Nuclear Region 1.46 sq. ″	SE [Ne V]$_{14.322\mu m}$ Aperture 0.96 sq. ″	SE [Ne II]$_{12.814\mu m}$ Region 1.3 sq. ″	East Warm Arm 2.26 sq. ″	South Warm Region 4.51 sq. ″	West Rotational Disk 1.25 sq. ″
H_2 0–0 S(1)	17.035	53.17 ± 1.23	42.63 ± 0.27	11.89 ± 0.05	21.53 ± 0.05	12.15 ± 0.12	4.78 ± 0.03
H_2 0–0 S(2)	12.279	28.12 ± 3.33	21.63 ± 0.54	4.36 ± 0.16	8.13 ± 0.16	4.44 ± 0.07	1.47 ± 0.13
H_2 0–0 S(3)	9.6649	86.82 ± 0.57	36.49 ± 0.06	5.83 ± 0.06	13.80 ± 0.07	7.64 ± 0.29	2.84 ± 0.07
H_2 0–0 S(4)	8.0251	37.44 ± 0.60	15.08 ± 0.23	1.76 ± 0.05	3.08 ± 0.20	2.19 ± 0.16	0.66 ± 0.05
H_2 0–0 S(5)	6.9095	90.05 ± 0.69	27.09 ± 0.47	2.45 ± 0.07	6.30 ± 0.10	4.76 ± 0.17	1.66 ± 0.08
H_2 0–0 S(6)	6.1086	16.11 ± 0.49	5.31 ± 0.08	0.46 ± 0.07	1.20 ± 0.14	<1.41	<0.38
H_2 0–0 S(7)	5.5112	86.97 ± 2.17	14.72 ± 0.23	1.34 ± 0.16	3.01 ± 0.39	1.11 ± 0.33	<0.46
H_2 0–0 S(8)	5.0530	16.45 ± 0.79	2.98 ± 0.08	0.46 ± 0.12	0.63 ± 0.16	<1.76	<0.34
LTE Fit Parameters							
β	…	4.2 ± 0.2	5.1 ± 0.08	5.7 ± 0.2	5.6 ± 0.06	5.7 ± 0.1	5.4 ± 0.2
$\log[N_{H_2}$ / cm$^{-2}]$	…	20.6 ± 0.1	20.8 ± 0.05	20.1 ± 0.1	20.1 ± 0.03	19.6 ± 0.1	19.7 ± 0.1
$\log[M_{H_2}$ / $M_\odot]$	…	$5.4^{+0.6}_{-0.7}$	$5.4^{+1.0}_{-1.0}$	$4.9^{+0.6}_{-0.7}$	$5.1^{+1.1}_{-1.1}$	$4.9^{+0.8}_{-0.8}$	$4.4^{+0.8}_{-0.9}$

Note. The LTE model best-fit parameters, as well as the total estimated molecular mass within each aperture, are also presented.

4. Methods

In this section, we describe the methodology used for the generation of emission-line maps and the associated velocity and velocity dispersion (σ), estimation of population levels (N_i/g_i), extinction corrections, and relevant modeling applied for data analysis. All underlying equations and assumptions utilized throughout the paper are outlined within this section. Any additional analysis focusing on the particular idiosyncrasies of either NGC 3081 or NGC 5506 will be discussed in the relevant sections (Section 5).

4.1. Emission-line Fitting and Mapping

To address the various spatial resolution of JWST channels, data cubes were resampled to a common pixel grid of 0.″13, corresponding to the smallest pixel grid of the data sets. Point-spread function (PSF) matching was applied by convolving emission-line maps with the FWHM of the largest relevant PSF, where spaxel-by-spaxel analysis was performed. Two-dimensional emission-line maps were generated from the IFU data cubes. We used a 3rd-order Chebyshev polynomial fit to characterize and subtract the local continuum and a Levenberg–Marquardt algorithm to apply a two-component Gaussian fit to each emission line of interest. Two components were utilized to obtain more accurate fits to the complex emission-line profiles, with the aim of separating emission from material within the rotating disk of the galaxy and that from outflowing material. Our fitting algorithm attempts to fit the emission line with both a single Gaussian component and with the inclusion of a secondary Gaussian component. From a likelihood-ratio test, if the secondary component was found to result in a statistically significant improvement of the χ^2 of the fit ($p > 0.05$), and the amplitude of both components was above 3 standard deviations of the continuum, then both components were used to fit the emission line. If these conditions were not satisfied, a single Gaussian component was used to model the emission line. For initial categorization, we assumed that the rotational disk of the galaxy will present more orderly kinematics, and therefore the narrower of the two Gaussians was assigned as the rotational component and the broader of the two was assigned to be the outflowing or noncircular component. A secondary routine was implemented to reassign components based on the velocity fields. We assume the emission associated with the rotational disk is likely to present an orderly rotational velocity gradient, and therefore we reassign components as necessary to ensure a smooth velocity field for the primary/rotational component. While this methodology attempts to isolate rotational and outflowing components, we recognize that the physical origin of the secondary component, although it improves the fit to the emission line, remains open for interpretation and may not necessarily be attributed to AGN outflows.

4.2. Estimating Population Levels and Excitation Energy

For optically thin media, the measured flux is intrinsically related to the amount of material available to produce emission. Therefore, from the flux measured from any given aperture, one can estimate the column density of the observed gas. The flux of transition is given by

$$F_i = \left(\frac{\Omega}{4\pi}\right) h\nu_i A_i N_i, \quad (1)$$

where F_i is the observed total flux, ν_i is the frequency of emission, A_i is the probability of transition, Ω is the beam solid angle, and N_i is the number of particles at the associated upper energy level. Therefore, by measuring the total flux and using Equation (1), we can estimate N_i for a given aperture for each emission line. From measured flux-integrated apertures of interest (described in Sections 2 and 3), we calculate associated population levels for the eight rotational molecular hydrogen transition lines in the MIR, H_2 0–0 S(1) through S(8), and the seven rovibrational molecular hydrogen transition lines visible in the NIR K band.

For a given continuous distribution of particles as a function of temperature, we are able to relate the number density of particles in a given state to the excitation temperature of the system via Boltzmann's equation. N_i for a given state can be estimated as

$$N_i = \frac{g_i}{Z(T)} N_{tot} \cdot e^{-E_i/kT}, \quad (2)$$

where T is temperature, g_i is the degeneracy value associated with the given state, $Z(T)$ is the temperature-dependent partition function, E_i is the energy level corresponding with

Table 3
NGC 5506 Measured Line Flux for the H_2 0–0 S(1) through S(8) Emission for Each Aperture of Interest

Emission Line	λ_{rest} (μm)	Flux (10^{-16}erg s^{-1} cm^{-2})					
		Nuclear Region 1.16 sq. ″	North Ionization Cone 2.28 sq. ″	Entrained Region 0.90 sq. ″	South Warm Arm 0.71 sq. ″	East Rotational Disk 0.90 sq. ″	West Rotational Disk 0.86 sq. ″
H_2 0–0 S(1)	17.035	112.70 ± 4.61	80.88 ± 0.63	45.57 ± 0.43	15.01 ± 0.12	25.86 ± 0.11	32.99 ± 0.09
H_2 0–0 S(2)	12.279	103.12 ± 7.93	28.33 ± 1.60	15.77 ± 1.72	7.55 ± 0.15	9.57 ± 0.07	13.84 ± 0.39
H_2 0–0 S(3)	9.6649	136.94 ± 1.46	68.65 ± 0.46	43.04 ± 0.27	15.02 ± 0.18	13.63 ± 0.40	13.96 ± 0.21
H_2 0–0 S(4)	8.0251	115.91 ± 2.52	24.46 ± 0.65	16.62 ± 0.27	5.71 ± 0.37	2.84 ± 0.66	6.47 ± 0.22
H_2 0–0 S(5)	6.9095	340.39 ± 2.89	39.97 ± 1.01	28.01 ± 0.39	18.23 ± 0.76	7.17 ± 0.33	11.53 ± 0.36
H_2 0–0 S(6)	6.1086	66.06 ± 2.32	4.83 ± 0.81	3.60 ± 0.54	<2.66	1.42 ± 0.33	1.86 ± 0.37
H_2 0–0 S(7)	5.5112	235.70 ± 3.93	16.91 ± 1.33	11.32 ± 0.91	<3.77	4.51 ± 1.32	3.91 ± 0.45
H_2 0–0 S(8)	5.0530	53.28 ± 4.22	<6.58	<1.86	<3.03	<2.32	<2.61
LTE Fit Parameters							
β	…	4.0 ± 0.1	5.4 ± 0.2	5.2 ± 0.2	4.5 ± 0.1	5.6 ± 0.2	5.7 ± 0.1
$\log[N_{H_2}$ cm$^{-2}]$	…	21.1 ± 0.1	20.7 ± 0.1	20.8 ± 0.1	20.4 ± 0.04	20.6 ± 0.1	20.8 ± 0.04
$\log[M_{H_2} / M_\odot]$	…	$5.6^{+0.7}_{-0.8}$	$5.5^{+0.6}_{-0.7}$	$5.2^{+0.6}_{-0.7}$	$4.7^{+1.0}_{-1.0}$	$4.9^{+0.7}_{-0.7}$	$5.1^{+1.0}_{-1.0}$

Note. The LTE model best-fit parameters, as well as the total estimated molecular mass within each aperture, are also presented.

the state i, k is Boltzmann's constant, and N_{tot} is the total number of particles across all states. From Equations (1) and (2), the temperature of an observed gas can be calculated from the flux ratio from two rotational hydrogen lines with corresponding energies E_i and E_j:

$$T = \frac{E_j - E_i}{k \cdot \ln\left(\frac{g_j A_j \lambda_i F_i}{g_i A_i \lambda_j F_j}\right)}. \quad (3)$$

For our analysis, we use the H_2 0–0 S(1)/S(5) line flux ratio (in lieu of the H_2 0–0 S(3) emission, which is potentially impacted by the 10 μm silicate absorption feature) to map the excitation temperature in the nuclear and circumnuclear region of each galaxy, as in R. Davies et al. (2024).

4.3. Thermal Equilibrium Modeling

By assuming the observed gas is in local thermodynamic equilibrium (LTE), we compare our measured relative population levels to that predicted by LTE modeling. The assumption of LTE implies that the observed gas is themalized and excitation of molecular gas is collisionally driven. We follow the approach outlined by A. Togi & J. Smith (2016) and assume a continuous single power-law temperature distribution for the H_2 population curve:

$$dN \propto T^{-\beta} dT, \quad (4)$$

where dN is the column density,and β is the power-law index. The power-law index β is of particular interest as it relates the proportions of warm to cool molecular gas mass: A lower value of β indicates that the observed emission is produced by molecular hydrogen with a higher proportion of warm gas mass. By integrating over a temperature range, we can update Equation (2) and estimate the relative population level as follows:

$$\frac{N_i}{g_i} = \left(\frac{N_{tot}(\beta - 1)}{T_l^{1-\beta} - T_u^{1-\beta}}\right) \int_{T_l}^{T_u} \frac{1}{Z(T)} \cdot e^{\frac{-E_i}{kT}} T^{-\beta} dT, \quad (5)$$

where $Z(T)$ is the temperature-dependent partition function, and T_l and T_u are the lower and upper temperature ranges of the distribution, respectively. For our analysis, we use $T_l = 200$ K, $T_u = 3500$ K, and approximate $Z(T) \approx \frac{0.0247T}{1 - e^{-6000/T}}$, valid for $T > 40$ K (T. Herbst et al. 1996; H. Roussel et al. 2007). The lower limit $T_l = 200$ K was utilized, as at this point the ortho-para hydrogen ratio (OPR) can be assumed to be 3 (M. G. Burton et al. 1992). The free parameters for this model include the total molecular hydrogen N_{tot} and β. For our analysis, a Levenberg–Marquardt optimization algorithm was used to select parameters which minimize the model χ^2. As this model provides an estimate of N_{tot}, we can therefore estimate the total number of particles via

$$n_{tot} = N_{tot} \Omega d^2, \quad (6)$$

where n_{tot} is the total number of particles and d is the distance to the object. Finally, we can estimate the total mass within the aperture as

$$M_{tot} = n_{tot} \cdot m, \quad (7)$$

where m is the particle mass (H_2 for our analysis). The estimated mass discussed in this paper represents the mass of warm H_2 (200–3500 K) without the additional correction factor of 1.36 for helium and other heavy metals (see R. Dickman et al. 1986; F. Bigiel et al. 2011).

4.4. Non-LTE Radiative Transfer Modeling

With the availability of VLT/SINFONI observations, we extend our analysis of the nuclear region to include seven additional rovibrational lines visible in the NIR. Previous studies have indicated that the rovibrational emission is produced by nonthermalized gas (R. I. Davies et al. 2005; R. Davies et al. 2024), precluding the usefulness of our single power-law LTE model. Instead, we follow the methodology outlined by M. Pereira-Santaella et al. (2014), in which RADEX (F. Van der Tak et al. 2007) is utilized to solve the radiative transfer equations for molecular hydrogen emission. The resulting grid, which estimates the fractional populations $[n_i(T, n_{H_2}, n_H)]$ for molecular hydrogen, considers temperatures ranging from 100

to 3600 K, and H_2 densities ranging from 10^2 to 10^9 cm^{-3}. The grid also considers collisions between both H_2 and atomic H, and assumes an OPR = 3. We again assume a single power-law temperature distribution (Equation (4)); however, we utilize estimated population levels from the RADEX grid to model relevant population levels. M. Pereira-Santaella et al. (2014) provides the modeled column density as

$$\frac{N_i(\beta, n_{H_2}, n_H)}{g_i} = \left(\frac{N_{tot}(\beta - 1)}{T_l^{1-\beta} - T_u^{1-\beta}}\right) \times \int_{T_l}^{T_u} T^{-\beta} n_i(T, n_{H_2}, n_H) dT, \quad (8)$$

where $n_i(T, n_{H_2}, n_H)$ is the fractional population level from the RADEX grid. Similarly to what we did in Section 4.3, we utilize the grid in the range of 200–3500 K and integrate from $T_l = 200$ K, $T_u = 3500$ K, and estimate population levels for comparison to our data. The free parameters for this non-LTE radiative transfer modeling include the number of molecular and atomic hydrogen (n_{H_2} and n_H), the power-law index β, and the total H_2 column density (N_{H_2}). We utilize a Levenberg–Marquardt minimization algorithm to select parameters which minimize the χ^2 of the model fit.

4.5. Shock Models

L. Kristensen et al. (2023) present an extensive library of ≈14,000 shock models which simulate H_2 emission and population levels for a variety of types of shocks and varied input parameters. These shocks are simulated in molecular gas zones and are relatively low velocity compared to those which may be expected in ionized zones. Model parameters include preshock density (n_H; ranging from 10^2 to 10^8 cm^{-3}), shock velocity (V_s; ranging from 2 to 90 km s^{-1}), a transverse magnetic field scaling parameter (b; ranging from 0.1 to 10.0, where the transverse magnetic field strength is $B = b \times \sqrt{n_H}$), the UV radiation field strength (G_0; ranging from 0 to 10^3) , the cosmic-ray ionization rate (ζ_{H_2}; ranging from 10^{-17} to 10^{-15} s^{-1}), and the fractional abundance of PAHs (ranging from 10^{-8} to 10^{-6}). We compare our population levels from the rotational (ν = 0–0) and rovibrational (ν = 2–1, 1–0) emission lines of the nuclear region to those predicted by shock models. Through comparison to the L. Kristensen et al. (2023) model, we constrain the four primary control parameters on H_2 emission intensity (n_H, V_s, b, and G_0). ζ_{H_2} and the fractional abundance of PAHs remain unconstrained as they are not a primary control on emission and we examine only a select number of rotational and rovibrational transition lines. The relevant model parameters also suggest whether the shock is continuous (C), a jump shock (J), or a hybrid continuous-jump-type shock (CJ). C-type shocks are those in which ionized particles are accelerated under the influence of a relatively large transverse magnetic field ($b \gtrsim 1$), and through collisions gradually disperse energy into the environment, resulting primarily in rotational excitation of H_2. J-type shocks typically occur in environments with a relatively weaker transverse magnetic field ($b \lesssim 0.3$), and where a sudden change in velocity triggers adiabatic heating. The resulting H_2 excitation is expected to be vibrationally dominated. Hybrid CJ-type shocks occur in environments which are already experiencing C-type shocks and an additional, relatively high-velocity shock event triggers adiabatic heating and the shock transitions to J type. Because of the numerous free parameters of the model and the variety of shock types, we select the model which minimizes χ^2 and also examine other shock scenarios which yield a low χ^2 with vastly different model parameters. This is done to highlight the different types of shock environments which may explain our observations.

4.6. Extinction Corrections

For the nuclear region, we utilize observations in both the MIR from JWST and NIR from VLT/SINFONI; therefore, the differential extinction between the two bands must be considered. T. K. Fritz et al. (2011) estimated the IR relative extinction curve derived for the Galactic center using hydrogen emission lines. We utilize this IR relative extinction curve to correct the relative extinction between the NIR and MIR. Also of interest, the H_2 0–0 S(3) line has the potential to be significantly impacted by extinction as a result of the 10 μm silicate absorption feature. The relative extinction parameter (A), which we use to scale the extinction curve to our individual targets, is calculated using the ratio of observed hydrogen recombination lines and the tabulated line fluxes presented by D. Hummer & P. Storey (1987). Other methodologies for correcting the relative extinction were explored by R. Davies et al. (2024), and no significant difference was found between methodologies.

5. Results and Interpretations

In this section, we present the results of the molecular and ionized emission-line mapping, relative population levels, and model comparisons for both NGC 3081 and NGC 5506. Additionally, our analysis focuses on identifying the primary excitation mechanism for molecular gas and explores the extent of AGN influence on the circumnuclear molecular material. Additional flux distribution, velocity, and σ maps for each of the two-component fits are presented in full in Appendix Figures A1–A20).

5.1. Molecular Hydrogen Distributions

The FOV of the observed JWST/MIRI IFU mosaic for NGC 3081 at its broadest extent allows for observations in the MIR to encompass the central nuclear ring of the galaxy. The normalized total flux distribution and associated velocity fields for the H_2 0–0 S(1), S(3), and S(5) rotational transition lines of NGC 3081 observed by JWST are presented in Figure 1. Within this centermost nuclear ring, the H_2 flux distribution is consistent with the structure outlined in Section 2.1. Molecular hydrogen is strongly centrally concentrated, and the weak nuclear bar of NGC 3081 is well defined by each rotational emission line. The elongation of this emission is along the axis of the AGN ionization cones. Spiral arms are clearly visible in the lower-energy S(1) rotational line flux (see also D. Esparza-Arredondo et al. 2025). Overlaid on the H_2 0–0 S(1) normalized emission map are the ALMA CO(2–1) intensity contours (from D. Rosario et al. 2018), which largely trace the distribution of the cool molecular gas. We find the distribution of the cool molecular gas to be spatially correlated with the H_2 0–0 S(1) associated warm molecular gas, with spiral arms and similar structures visible in both the S(1) and CO(2–1) distributions. These features highlight the nonuniform distribution of molecular gas in the circumnuclear region. These spiral arms become less apparent for the higher-energy

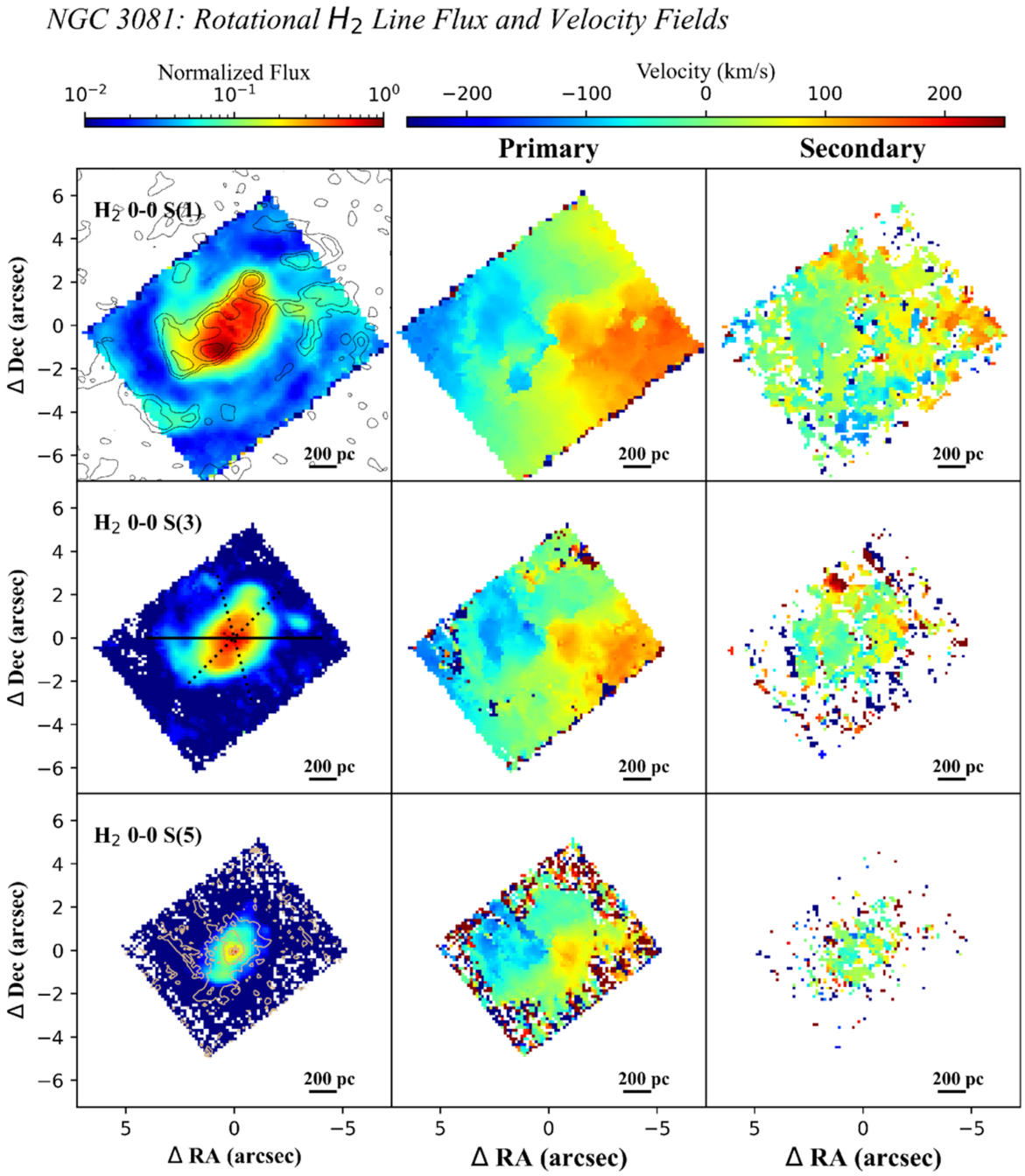

Figure 1. The left column presents the normalized flux distribution for the H_2 0–0 S(1), S(3), and S(5) emission lines normalized by the maximum flux value for NGC 3081. The black contours overlaid on the H_2 0–0 S(1) line map present the ALMA CO(2–1) intensity distribution (D. Rosario et al. 2018); contours range from $10^{-1.35}$ to $10^{-0.3}$ Jy (0.35 dex steps). The solid black line overlaid on the H_2 0–0 S(3) line map indicates the orientation of the disk (PA = 90°), and the dotted black lines indicate the edges of the ionization bicone (PA = 165°, $\Omega_{\rm Out}$ = 30°). The associated velocity fields for both the primary and secondary fit components are presented in the right two panels. The tan contours overlaid on the H_2 0–0 S(5) normalized flux distribution represent the [Fe II]$_{5.34\mu m}$ intensity distribution; contours range between $10^{-7.25}$ and $10^{-6.25}$ Jy (0.5 dex steps). The center column presents the rotational component for the two-component fit, and the right column presents the secondary/outflowing fit component.

rotational lines, and the flux distribution becomes primarily centrally concentrated, suggesting that H_2 outside of the nuclear region lacks the excitation energy necessary to produce these lines.

The kinematics of the H_2 gas is relatively orderly, displaying a clear rotational gradient around the nucleus. The center and right panels of Figure 1 depict the velocity fields for both the primary and secondary components of the emission-line fits. While the two-component fit is useful for better constraining the line flux for this galaxy, the secondary component does not reveal any consistent nonrotational molecular gas, highlighting no obvious noncircular motions of H_2. The secondary component becomes less defined/resolvable as the signal-to-noise ratio (S/N) decreases in the circumnuclear region for the higher-energy rotational lines. For completeness, the associated σ is presented in Appendix A.1 and highlights some bands of increased σ between the spiral arms/dust lanes observed in the flux distribution, suggesting a more orderly distribution of

molecular gas within the spiral arms compared to the other circumnuclear molecular gas orbiting the AGN, consistent with the observations of D. Esparza-Arredondo et al. (2025) for the Seyfert galaxy MCG-5-23-16.

Figure 2 presents the total flux distribution and associated velocity fields for the NGC 5506 H_2 0–0 S(1) through S(5) rotational transition lines. The galactic disk is clearly visible in the S(1) and S(2) emission-line maps, and we observe significant amount of molecular hydrogen to the north and south of the disk. Again, over the H_2 0–0 S(1) normalized emission map we overlay the ALMA CO(3–2) (from S. García-Burillo et al. 2021) intensity contours which trace cooler molecular gas distributions. Just as was observed for NGC 3081, we find the distribution of the cool molecular gas to be spatially correlated with the H_2 0–0 S(1) associated warm molecular gas. The higher-energy rotational lines become more centrally concentrated around the AGN. Flux distributions for the higher rotational lines also highlight tendrils of molecular gas spanning out from the nucleus. These are particularly well defined for H_2 0–0 S(3) and are strongly spatially correlated with the edges and center of the ionization bicone to the north and south of the AGN. This suggests that the AGN is either irradiating and/or shocking molecular gas to the north and south of the disk, or that the AGN is actively transporting warm molecular hydrogen from the nucleus and potentially out of the plane of the rotational disk. The emission topography of the higher rotational lines is spatially correlated with the [Fe II]$_{5.34\mu m}$ flux distribution (included in Figure 2 as tan contours for the S(5) line map), implying that shocks are an important excitation mechanism.

The center and right panels of Figure 2 portray the two component velocity fields for the S(1) through S(5) emission. We are able to successfully separate out the primary rotational component of the emission-line fit from the secondary component. For the rotational component of these H_2 emission lines, we observe a smooth rotational gradient clearly visible along the major axis of the disk. With the velocity gradient of the secondary component, we identify a velocity perturbation indicating a clear and consistent nonrotational feature in the molecular gas spatially consistent with the northeast edge of the ionization cone. We take this to be a strong indicator that H_2 is likely being entrained in an AGN outflow and exported from either the nuclear region or perhaps from the point of contact in which the AGN outflow intersects the rotational disk (Section 2.2). The relative motion of the outflow to the rotational disk is such that it makes separating this outflowing component relatively easy in this region. It is possible that other molecular outflows are present to the northwest edge of the ionization cone, however this cannot be easily distinguished as outflowing gas may share a similar line-of-sight velocity signature as the disk. Outflowing H_2 along the southern ionization cone is also possible, however the signature of these outflows may be impacted due to our line of sight through the galaxy disk resulting in our observations being dominated by the foreground disk kinematics. In the absence of other clear outflow signatures, we lend favor to the interpretation that this nonrotational velocity perturbation likely results from an interaction between the ionization cone and ionized outflows and the molecular disk (see Figure 4 in C. Ramos Almeida et al. 2022). We take this as further affirmation of the geometry presented by F. Esposito et al. (2024) in which a potential interaction between the northern ionization cone and rotational disk was suggested. Again for completeness, σ is presented in Appendix A.2 and displays some elevated dispersion for higher-energy rotational lines along the axis of the outflow.

5.2. Ionized Gas

We investigate ionized gas emission to garner insight as to the relevant excitation mechanisms and impact of ionization cones, outflows, and shocks to the circumnuclear region. Known to be a good tracer of fast shocks, emission of [Fe II]$_{5.34\mu m}$ has also been shown to correlate with rotational H_2 emission, suggesting shock excitation of molecular gas (M. Pereira-Santaella et al. 2014; B.-C. Koo et al. 2016). For the analysis of this emission line, a secondary component was not found to be useful for fitting or interpreting results, therefore we opt to use a single-component fit. Figure 3 shows the [Fe II]$_{5.34\mu m}$ flux distribution and kinematics for NGC 3081 and NGC 5506. Radio jets have been shown to be an important AGN feedback mechanism impacting molecular gas, both compressing and driving molecular outflows from the AGN (C. Ramos Almeida et al. 2022; A. Audibert et al. 2023; L. Peralta de Arriba et al. 2023; L. R. Holden et al. 2024). R. A. Riffel et al. (2025) concluded excess H_2 emission in kinematically disturbed regions to originate from the resultant shocks due to radio jets interacting with the interstellar medium. Motivated by this correlation between shock excitation of H_2, we overlay 8.46 GHz radio intensity contours from the Very Large Array (VLA; A. R. Thompson et al. 1980; P. J. Napier et al. 1983) on the [Fe II]$_{5.34\mu m}$ distribution maps in Figure 3.

For NGC 3081, [Fe II]$_{5.34\mu m}$ emission is not widespread and is only prevalent within the nuclear region. Nuclear emission is again elongated along the axis of the ionization cone, particularly to the southeast, which indicates some level of shock excitation resulting from the ionization cone interacting with ambient disk material. The associated velocity field shows some signs of rotation, albeit weakly. The velocity dispersion, σ, does not have an obvious or consistent structure. Following this, we do not anticipate a high potential for gas to be shocked outside of the nuclear region. The 8.46 GHz VLA radio emission[34] is compact and limited in range, not tightly spatially correlated with the [Fe II]$_{5.34\mu m}$ emission. We observe little spatial correlation between the radio and [Fe II]$_{5.34\mu m}$ emission.

In contrast, [Fe II]$_{5.34\mu m}$ emission in NGC 5506 is centrally concentrated with emission expanding outward across our FOV, particularly to the north. The topography of the flux distribution is spatially correlated with the 8.46 GHz VLA radio emission (from H. Schmitt et al. 2001) as well as with emission of the higher-energy rotational H_2 lines (overlaid on Figure 2 as tan contours). This spatial correlation further implies shock excitation as a potentially important excitation mechanism for H_2, as shown in previous studies (A. Audibert et al. 2023; R. A. Riffel et al. 2025). The associated velocity field clearly highlights the rotational gradient of the disk and presents two velocity perturbations to the north and south within the ionization bicone. These perturbations are due to their location and orientation, clearly associated with ionized outflows from the AGN, i.e., likely signatures of shocked material outflowing from the AGN. The line-of-sight motion is

[34] NRAO/VLA Archive Survey: https://archive.nrao.edu/.

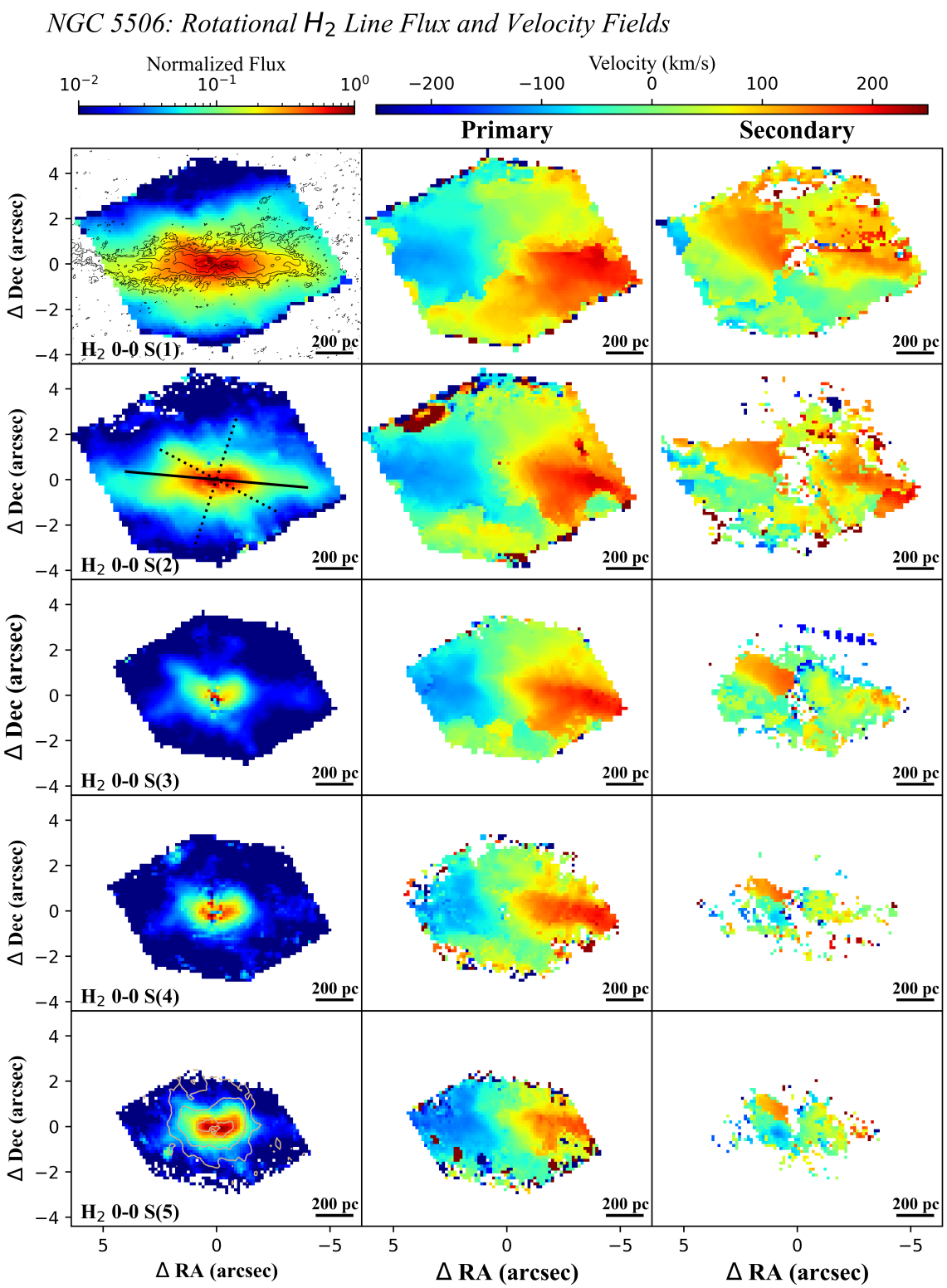

Figure 2. The left column presents the flux distribution for the H_2 0–0 S(1), S(2), S(3), S(4), and S(5) emission lines normalized by the maximum flux value for NGC 5506. The black contours overlaid on the H_2 0–0 S(1) line map present the distribution of ALMA CO(3–2) intensity distribution (S. García-Burillo et al. 2021); contours range from $10^{-1.35}$ to $10^{-0.3}$ Jy (0.35 dex steps). The solid black line overlaid on the H_2 0–0 S(2) line map indicates the orientation of the disk (PA = 90°), and the dotted black lines indicate the edges of the ionization bicone (PA = 22°, $\Omega_{\rm Out}$ = 80°). The tan dashed contours overlaid on the H_2 0–0 S(5) flux map represent the [Fe II]$_{5.34\mu m}$ intensity distribution; contours range from $10^{-6.25}$ to $10^{-5.25}$ Jy (0.5 dex steps). The associated velocity fields for both the primary and secondary fit components are presented in the right two panels. The center column presents the rotational component for the two-component fit, and the right column presents the secondary/outflowing fit component.

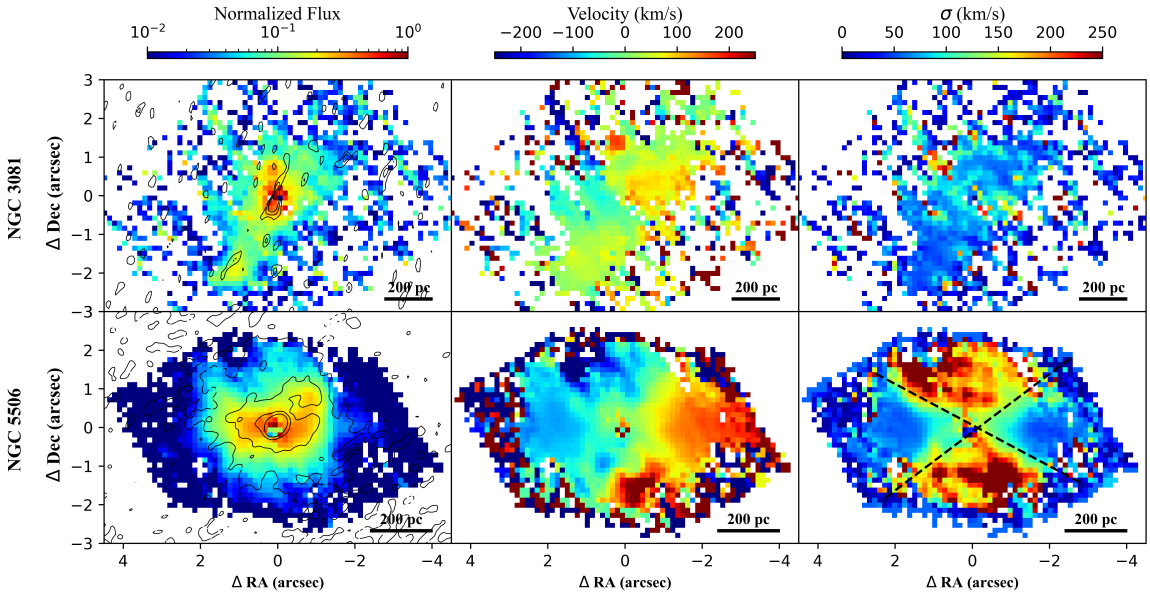

Figure 3. Total flux distribution (normalized by the maximum flux value) and kinematics for NGC 3081 (top panels) and NGC 5506 (bottom panels) derived from [Fe II]$_{5.34\mu m}$ emission. The left column presents the normalized flux distribution, the center column depicts the associated velocity field, and the right column depicts the associated velocity dispersion. Overlaid on the flux distribution are the 8.46 GHz radio intensity contour lines. For NGC 3081, the contour intervals (NRAO/VLA Archive Survey: https://archive.nrao.edu/) range from $10^{-4.5}$ to $10^{-4.0}$ Jy Beam^{-1} in 0.25 dex steps. For NGC 5506, the contour intervals (H. Schmitt et al. 2001) range from $10^{-4.5}$ to $10^{-2.5}$ Jy Beam^{-1} in 0.5 dex steps. Dashed lines overlaid on the dispersion map of NGC 5506 indicate a wider opening angle of $\Omega = 140°$.

consistent with the geometry of the ionization cones of NGC 5506 discussed in Section 2.2. The outflow region is also well defined by σ, which presents an hourglass shape of high σ reminiscent of eRosita bubbles (H.-Y. K. Yang et al. 2022; K. C. Sarkar 2024) along the path of the outflow, suggesting less orderly ionized or shocked gas expanding out from the AGN. The extent of this dispersion feature suggests a wider outflow opening angle than previously indicated (T. Fischer et al. 2013). We find this dispersion feature to be more fully constrained with a wider opening angle of $\Omega \approx 140°$ relative to the 80° opening angle estimated by T. Fischer et al. (2013), indicated in Figure 3 (bottom-right panel) with dashed lines.

Also visible to JWST/MRS, neon emission provides further insight into the relevant local excitation mechanisms. The presence of [Ne II]$_{12.814\mu m}$ (with an ionization potential of 21.56 eV) emission has often been considered a reliable tracer of star formation; or, to be more precise, [Ne II]$_{12.814\mu m}$ emission can result from protoplanetary disk environments (C. Baldovin-Saavedra et al. 2012). These same [Ne II]$_{12.814\mu m}$ excitation mechanisms (shocks, X-ray disk irradiation, and jets; A. E. Glassgold et al. 2007; D. Hollenbach & U. Gorti 2009; H. Shang et al. 2010) are shared by AGN activity (I. García-Bernete et al. 2017); therefore, we interpret this emission with caution, as it can arise in a variety of environments. On the other hand, with a higher ionization potential of 97.12 eV, [Ne V]$_{14.322\mu m}$ emission indicates high levels of extremely energetic photoionization associated with AGN activity or compact star-forming regions (Y. I. Izotov et al. 2012; G. R. Zeimann et al. 2014; N. J. Cleri et al. 2023). The normalized flux distributions for both [Ne II]$_{12.814\mu m}$ and [Ne V]$_{14.322\mu m}$ are presented in the left and center panels of Figure 4, respectively. The kinematics of ionized gas associated with neon emission is explored in detail in L. Zhang et al. (2024b). M.-Y. Zhuang et al. (2019) explored the relationship between MIR neon emission lines, AGN activity, and star formation rates, and report that typical Seyfert AGN emit within a narrow ratio of [Ne II]$_{12.814\mu m}$ to [Ne V]$_{14.322\mu m}$. The right panel of Figure 4 presents the ratio of [Ne II]$_{12.814\mu m}$ to [Ne V]$_{14.322\mu m}$ flux over the FOV. Following M.-Y. Zhuang et al. (2019), a [Ne II]$_{12.814\mu m}$/[Ne V]$_{14.322\mu m}$ in excess of 0.345 ± 0.118 indicates regions in which a significant portion of [Ne II]$_{12.814\mu m}$ emission may not result directly from the AGN.

The top panels of Figure 4 present the normalized flux distribution for [Ne II]$_{12.814\mu m}$ and [Ne V]$_{14.322\mu m}$ as well as the respective line ratio for NGC 3081. We observe strong nuclear [Ne II]$_{12.814\mu m}$ emission that is elongated along the axis of the AGN ionization cone, suggesting photoionization throughout the cone. Additionally, we observe bands of emission in the circumnuclear region, which we interpret to be the two star-forming arms that are present within the nuclear ring (Section 2.1). We note that the brightest portion of the southern star-forming arm is spatially coincident with the axis of the ionization cone. For [Ne V]$_{14.322\mu m}$, we observe the emission to be largely concentrated in the nucleus and elongated along the ionization cone, suggesting that gas within the path of the ionization cone is being strongly irradiated and photoionized by the AGN. In the case of NGC 3081, most of the excess emission is seen circumnuclear to the AGN, with the highest levels of excess emission corresponding to the inner star-forming arms.

The bottom panels of Figure 4 present the normalized flux distribution for both [Ne II]$_{12.814\mu m}$ and [Ne v]$_{14.322\mu m}$ and the respective line ratio for NGC 5506. Both the [Ne II]$_{12.814\mu m}$ and [Ne v]$_{14.322\mu m}$ emission are strongly centrally concentrated. [Ne II]$_{12.814\mu m}$ presents as largely symmetric with some elongation of the brightest emission along the primary rotation axis. The flux distribution of [Ne v]$_{14.322\mu m}$, on the other hand, while centrally concentrated is largely elongated to the north and south of the AGN, suggesting photoionization along the

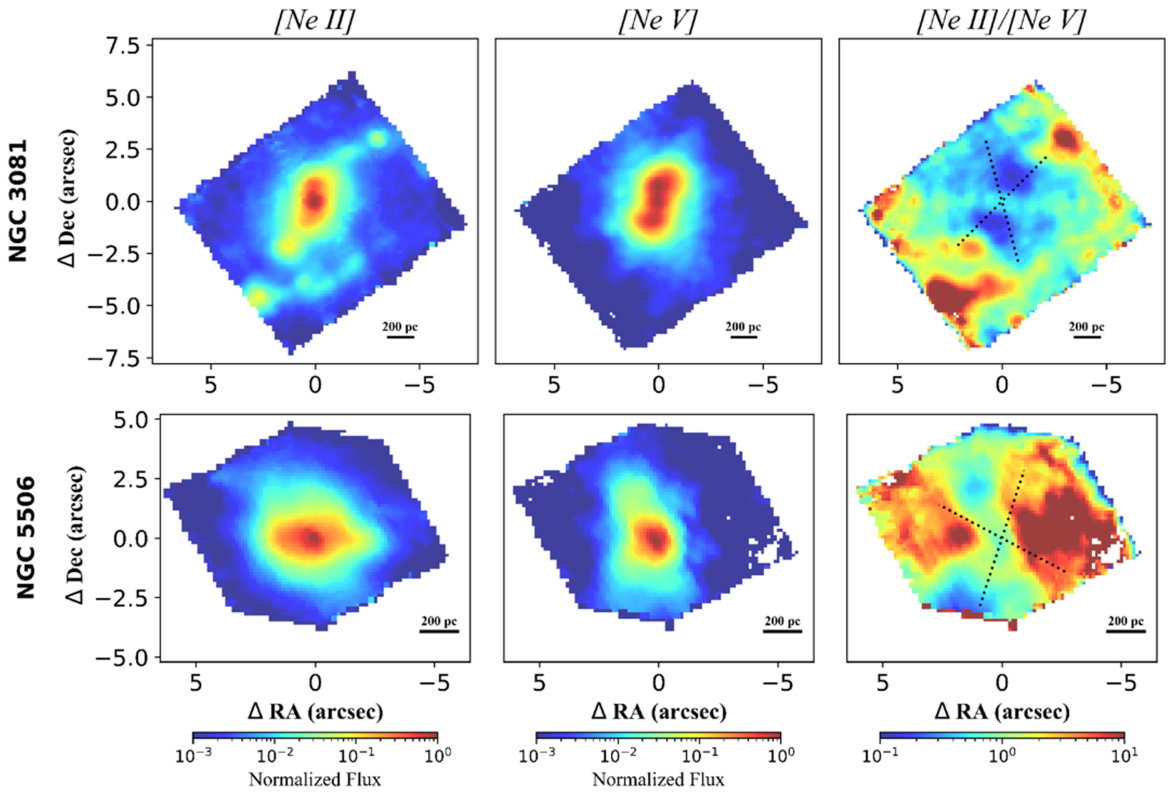

Figure 4. For NGC 3081 (top panels) and NGC 5506 (bottom panels), the left column presents the normalized $[\mathrm{Ne\ II}]_{12.814\mu\mathrm{m}}$ flux distribution, the center column presents the $[\mathrm{Ne\ V}]_{14.322\mu\mathrm{m}}$ flux distribution (line maps have been normalized by the maximum flux value for each respective map), and the right column presents the spatial distribution of the observed $[\mathrm{Ne\ II}]_{12.814\mu\mathrm{m}}/[\mathrm{Ne\ V}]_{14.322\mu\mathrm{m}}$ flux ratio. To address differences in the PSF, the $[\mathrm{Ne\ II}]_{12.814\mu\mathrm{m}}$ emission map has been convolved with the FWHM of the PSF of the $[\mathrm{Ne\ V}]_{14.322\mu\mathrm{m}}$ line prior to computing the flux ratio map. The dotted black lines indicate the edges of the ionization bicone, PA = 165°, $\Omega_{\mathrm{Out}} = 30°$ and PA = 22°, $\Omega_{\mathrm{Out}} = 80°$ for NGC 3081 and NGC 5506, respectively.

axes of the bicone. To the south, we observe a wider region over which $[\mathrm{Ne\ v}]_{14.322\mu\mathrm{m}}$ emission is bright, potentially suggesting a wider opening angle for the southern portion of the ionization cone. The right column of Figure 4 presents the $[\mathrm{Ne\ II}]_{12.814\mu\mathrm{m}}/[\mathrm{Ne\ v}]_{14.322\mu\mathrm{m}}$ observed flux ratio. Along the axis of the ionization bicone to the north and south for NGC 5506, we observe the lowest rates of excess $[\mathrm{Ne\ II}]_{12.814\mu\mathrm{m}}$, suggesting photoionization from the AGN is a dominant excitation mechanism. To the south, regions of low $[\mathrm{Ne\ II}]_{12.814\mu\mathrm{m}}/[\mathrm{Ne\ v}]_{14.322\mu\mathrm{m}}$ are noticeably offset from the assumed orientation of the ionization bicone. To the east and west, within the circumnuclear disk, we see excess $[\mathrm{Ne\ II}]_{12.814\mu\mathrm{m}}$. Interestingly, the distribution of excess $[\mathrm{Ne\ II}]_{12.814\mu\mathrm{m}}$ is asymmetric throughout the circumnuclear rotational disk, with significantly more excess emission and therefore excitation energy present in the western arm (see also I. García-Bernete et al. 2024).

5.3. Molecular Gas Excitation

Following the procedure outlined in Section 4.2, we use the H_2 0–0 S(1)/S(5) line ratio to map the thermal excitation energy around the AGN (Figure 5). We overlay contours of the $[\mathrm{Fe\ II}]_{5.34\mu\mathrm{m}}$ and $[\mathrm{Ne\ v}]_{14.322\mu\mathrm{m}}$ emission. For NGC 3081, we find the excitation energy to be largely centrally concentrated with some higher-temperature regions present circumnuclear to the AGN, particularly to the south. The excitation energy distribution displays some elongation along the axis of the outflow and closely matches the orientation and extent of the $[\mathrm{Ne\ V}]_{14.322\mu\mathrm{m}}$ distribution. Similarly, this elongation is generally consistent with that displayed by the $[\mathrm{Fe\ II}]_{5.34\mu\mathrm{m}}$ contours, which are elongated along the southeast ionization cone. The elongation of the nuclear thermal feature could suggest that the ionization cone and associated outflows may be responsible for transporting excitation energy into the circumnuclear region; however, the extent of this effect appears to be limited in radial extent. Warm regions outside of the ionization cone may be a result of increased rates of collisional excitation (potentially in dust lanes) or excitation driven by local star formation rather than outflow-driven excitation.

In NGC 5506, excitation energy is again largely centrally concentrated with some significant elongation of the thermal distribution into the disk of the galaxy. To the north and south, this elongation is spatially coincident with the ionization bicone. To the north of the nuclear region, we observe a saddle-like feature in which the excitation energy distribution extends to the northwest and northeast. This feature closely mimics that of the $[\mathrm{Fe\ II}]_{5.34\mu\mathrm{m}}$ emission contours, potentially indicating shock excitation to be the dominant excitation mechanism of the local molecular gas. The apparent hollowness of this feature could suggest that the molecular material has been cleared out by the outflow (consistent with the low CCI observed for this object; S. García-Burillo et al. 2021, 2024). Strong $[\mathrm{Ne\ v}]_{14.322\mu\mathrm{m}}$ emission encompass the nuclear warm region and is elongated to the north along the ionization bicone extending through the center of the saddle feature, implying that excitation within the nuclear region may be the result of both high-energy photoionization and shocks. These features are not clearly mirrored to the south. We do observe a

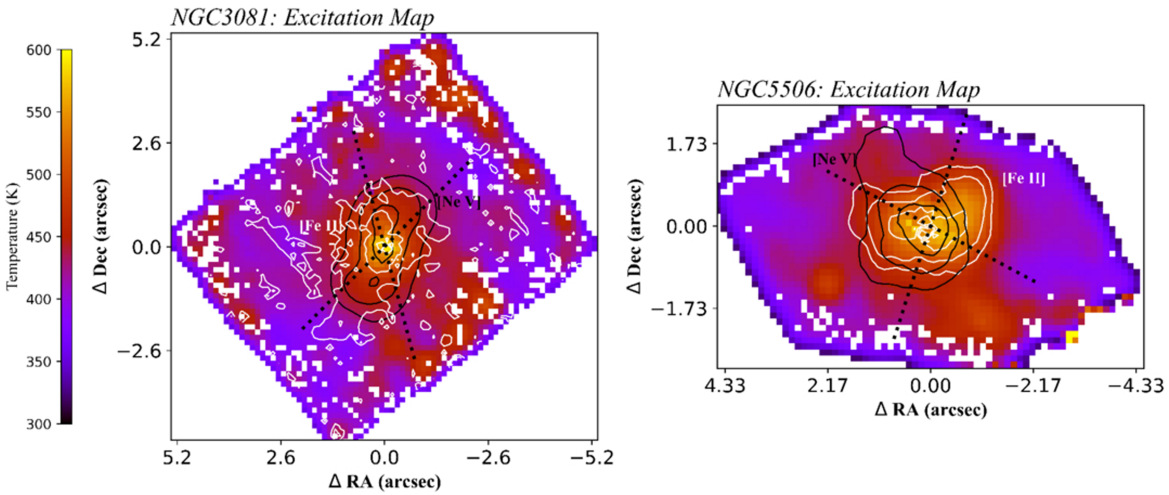

Figure 5. Thermal mapping for NGC 3081 (left panel) and NGC 5506 (right panel) generated from the H_2 0–0 S(1)/S(5) line ratio. To address differences in PSF, the S(5) emission maps have been convolved with the FWHM of the broader PSF of the S(1) line prior to computing excitation maps. Black and white contours outline the [Ne V]$_{14.322\mu m}$ and [Fe II]$_{5.34\mu m}$ emission, respectively. The dotted black lines indicate the edges of the ionization bicone, PA = 165°, $\Omega_{Out} = 30°$ and PA = 22°, $\Omega_{Out} = 80°$ for NGC 3081 and NGC 5506, respectively. For NGC 3081, the [Fe II]$_{5.34\mu m}$ intensity contours range from $10^{-7.25}$ to $10^{-6.25}$ Jy (in 0.5 dex steps) and the [Ne V]$_{14.322\mu m}$ intensity contours range from $10^{-5.0}$ to $10^{-4.0}$ Jy (in 0.5 dex steps). For NGC 5506, the [Fe II]$_{5.34\mu m}$ intensity contours range from $10^{-5.75}$ to $10^{-5.0}$ Jy (in 0.25 dex steps) and the [Ne V]$_{14.322\mu m}$ intensity contours range from from $10^{-4.8}$ to $10^{-3.8}$ Jy (in 0.5 dex steps).

particularly warm arm to the southwest (spatially coincident with the southern ionization bicone) and a less warm arm (and bright spot) to the southwest.

5.4. LTE Modeling

Taking a more quantitative approach, we investigate the relative proportions of warm molecular hydrogen present in regions in and around the nucleus. Following the methodology outlined in Section 4.2, we estimate population levels of molecular hydrogen based off the rotational emission lines in select regions of interest around the AGN.

5.4.1. NGC 3081: LTE Analysis

Figure 6 depicts the apertures selected for investigation, associated integrated spectra, and LTE modeling results for NGC 3081. These apertures were selected as regions of interest based on their proximity to the AGN outflows, structures of interest, and regions of elevated excitation energy (Figure 5). We select an arbitrary aperture within the western edge of the rotating disk (orange aperture), targeting no specific feature as a baseline measurement. We also select one enclosing the southern warm region blue aperture, two in the south-southeastern arm of the ionization cone (one of which marks the extent of bright [Ne V]$_{14.322\mu m}$ emission and the other the extent of bright nuclear [Ne II]$_{12.814\mu m}$ emission; purple and red apertures, respectively), an aperture enclosing a warm arm to the east (green aperture), and a circular nuclear aperture aligned with the disk which has been projected at 40° to match the maximum estimated inclination of the disk (black aperture). Regarding aperture selection within the ionization cone, we opt to investigate the southeastern arm of the ionization cone rather than the northwest as we observe [Fe II]$_{5.34\mu m}$ and [Ne II]$_{12.814\mu m}$ to be more elongated along this portion of the cone.

The top-right panel of Figure 6 displays the estimated relative population levels for each region of interest as well as the best-fit LTE model attained via the methodology described in Section 4.3. LTE modeling for this analysis was performed neglecting the S(3) population level; this decision was physically motivated, as the S(3) emission is significantly impacted by the 10 μm silicate absorption feature and may impact the model fit. The measured flux for each rotational emission line and the LTE best-fit parameters are presented in Table 2. Errors in the population level estimates are directly proportional to the error in the measured flux. The region with the highest relative proportion of warm molecular gas is the nuclear region, with $\beta = 4.2$. Extending outward from the nucleus, the LTE fit curves flatten out and trend toward a constant value. The [Ne V]$_{14.322\mu m}$ aperture (immediately adjacent to the nuclear aperture) presents the next shallowest curve with $\beta = 5.1$. Moving outwards, best-fit values of β are more consistent, in the range of 5.4–5.7, indicating emission is more dominated from molecular hydrogen at lower temperatures. We interpret the consistency in estimated values of β across apertures to suggest that the extent of impacts from AGN photoionization or outflows along the ionization cone may be limited as circumnuclear apertures at distance are indistinguishable based on LTE modeling. These estimates for β are consistent with those reported in previous works for ULIRGs (β in the range 2.5–5.0; N. L. Zakamska 2010) and those studying LINERs and Seyfert galaxies (β in the range 4.0–6.0; M. Pereira-Santaella et al. 2014; A. Togi & J. Smith 2016; R. Davies et al. 2024). Model estimates of $\log[N_{H_2}/cm^{-2}]$ display similar behavior as observed for β. The highest estimated $\log[N_{H_2}/cm^{-2}]$ is found within the nuclear region followed by the [Ne V]$_{14.322\mu m}$ and eastern warm arm aperture. Our circumnuclear apertures yield lower column density estimates in the range of $10^{19.6-20.1}$ cm^{-2}, with the arbitrary rotational disk aperture and southern warm aperture yielding the lowest values of $\log[N_{H_2}/cm^{-2}]$. L. Zhang et al. (2024a) performed a similar analysis on NGC 3081 using larger nuclear 3″ × 3″ and circumnuclear apertures, reporting estimates for β and $\log[N_{H_2}/cm^{-2}]$ ranging from 4.9 to 5.2 and 19.94 to 20.59, respectively, in good agreement with our findings. Additionally, T. Bohn et al. (2024) performed a similar analysis, studying the warm molecular gas in outflows from NGC 3526. They reported a similar trend in the thermal

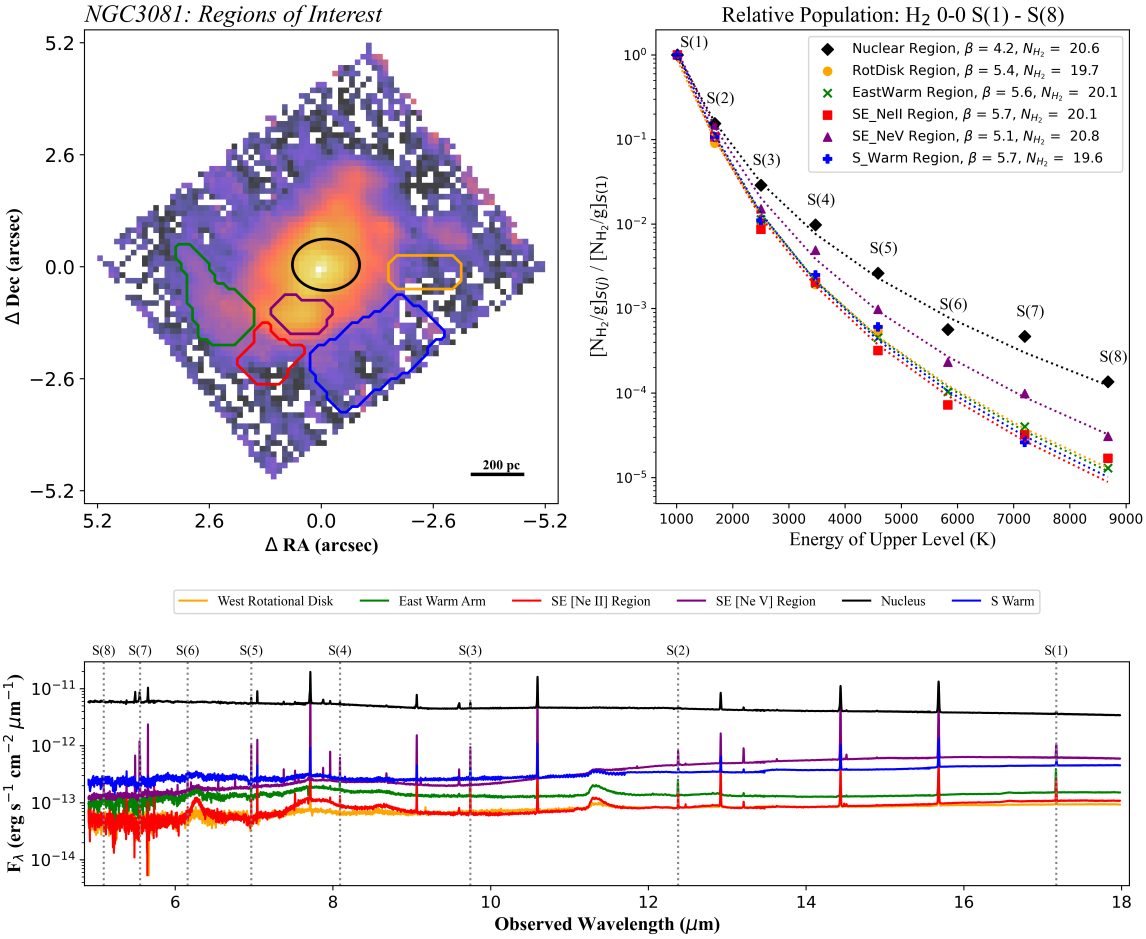

Figure 6. The top-left panel depicts the NGC 3081 H_2 0–0 S(5) normalized line flux and apertures utilized for analysis. The bottom panel depicts the integrated spectra for the associated apertures. The top-right panel presents the estimated population levels for each of the associated eight MIR rotational H_2 emission lines and the LTE best fit for each aperture of interest.

scaling parameter β along the outflow, with values ranging from approximately 4.5 near the nucleus to about 5.9 at larger distances.

To investigate the extent of the AGN photoionization as an excitation mechanism in NGC 3081, we perform our LTE analysis in graduated steps along the axis of the ionization cone. To isolate the ionization cone, we utilize a wide slit capturing the nuclear $[\mathrm{Ne\,V}]_{14.322\mu\mathrm{m}}$ emission and extract 2 pixel annular apertures for each rotational H_2 line. These annular apertures include portions of both the northwest and southeast ionization cones simultaneously to optimize the S/N for each annular aperture. Figure 7 depicts the wide-slit aperture capturing $[\mathrm{Ne\,V}]_{14.322\mu\mathrm{m}}$ emission, an example annular aperture, and the best-fit β and $\log[N_{\mathrm{H_2}}/\mathrm{cm}^{-2}]$ as a function of radial distance from the AGN. The estimated $\log[N_{\mathrm{H_2}}/\mathrm{cm}^{-2}]$ decreases consistently with radial distance along the axis of the ionization cone, suggesting a relatively smooth density gradient, a result consistent with the CCI-implied relatively flat distribution of cool molecular gas found for NGC 3081 by S. García-Burillo et al. (2024). β, as anticipated, increases with radial distance before leveling out and becoming relatively constant. Informed by the results of our LTE fits to the circumnuclear apertures (Figure 6), we take $\beta = 5.5$ as the threshold at which the proportions of warm and cool molecular gas becomes indistinguishable to any portion of the circumnuclear region. Following this, we estimate the extent at which the ionization cone is a relevant contributor to the excitation of H_2 to be ≈330 pc on sky. Outside of this range, we anticipate the photoionization from the AGN to have a minimal impact on the circumnuclear molecular gas.

5.4.2. NGC 5506: LTE Analysis

Figure 8 depicts the apertures used for investigation of molecular gas (top-left panel) and associated integrated spectra (bottom panel) for NGC 5506. For display purposes, the integrated spectra for the rotational disk regions are omitted from the figure due to their relatively low level of continuum emission. We select two arbitrary apertures of the rotating disk to the east and west to form a baseline for the analysis (orange and gray apertures, respectively). We select an aperture of the northern ionization bicone (blue aperture) with a 40° half-opening angle and inclined at 22° to the east to match the geometry of the ionization cone (Table 1). Additionally, we select an aperture along the western edge of the northern bicone in which H_2 displays a nonrotational outflowing component, an aperture capturing the southern warm arm coincident with the ionization cone (green aperture), an aperture along the southern warm arm coincident with the southern ionization cone (red aperture), and a nuclear aperture (black aperture). The nuclear aperture is a circular aperture projected at 80° to match the inclination of the galaxy and

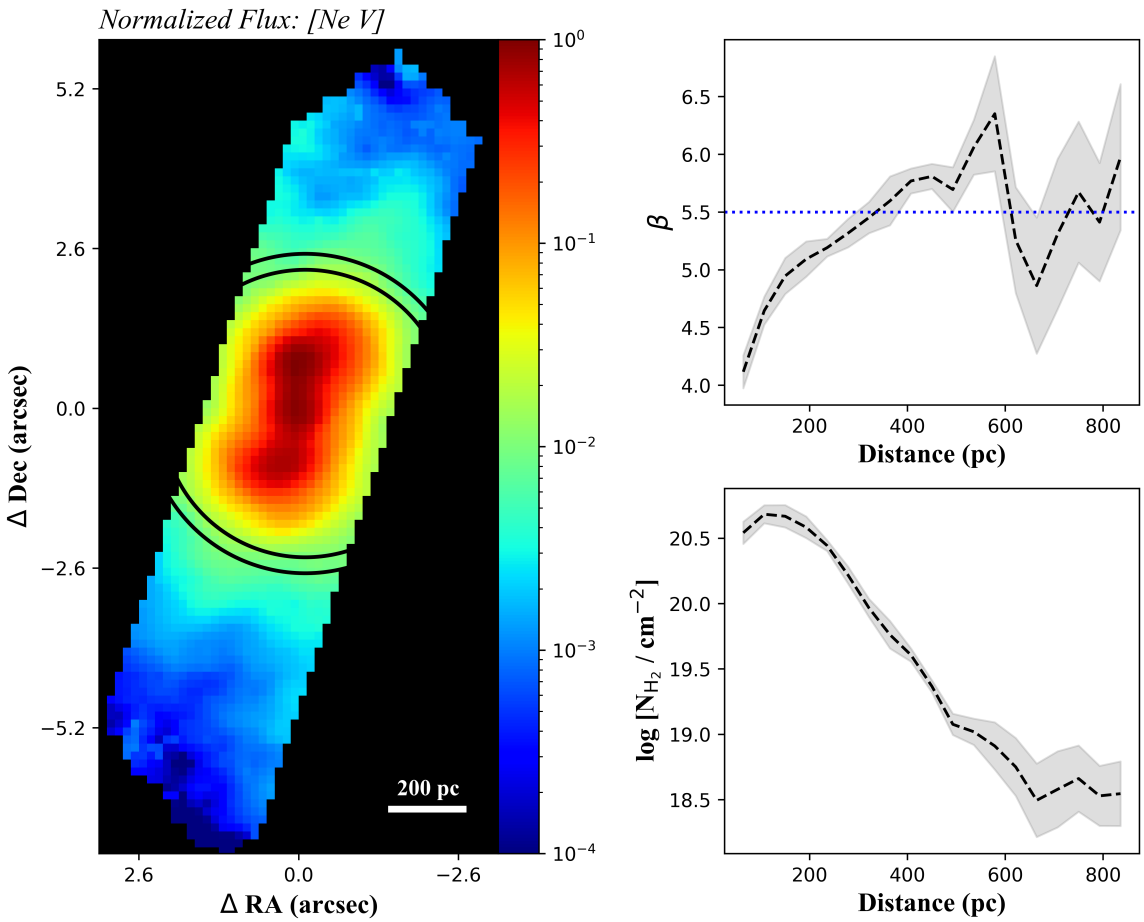

Figure 7. Radial LTE analysis for the ionization bicone of NGC 3081. The left panel presents the wide-slit aperture encompassing the $[\mathrm{Ne\ V}]_{14.322\mu\mathrm{m}}$ emission. The black outline highlights an example integration aperture for the LTE modeling. The top-right panel presents the best value of the thermal scaling parameter β as a function of radial distance. The bottom-right panel presents the LTE model best-fit $\log[N_{\mathrm{H_2}}/\mathrm{cm}^{-2}]$ as a function of radial distance from the nucleus. Shaded gray regions indicate the standard error of the LTE fit parameters.

aligned with the position angle of the rotational disk. The semimajor axis of the resulting ellipse was expanded to ensure the FWHM of the PSF is captured.

Table 3 presents the measured line flux for the eight H_2 emission lines visible in the MIR. Following the methodology outlined in Sections 4.2 and 4.3, we estimate the N_i/g_i for each rotational transition and model the population curve assuming LTE. Figure 8 depicts the resultant relative population levels as well as the best-fit LTE curve for each aperture; the model best-fit parameters are included in Table 3. Again, we opt to exclude the S(3) population level from the model fit to mitigate impacts from the 10 μm silicate absorption feature. The nuclear region holds the highest proportion of warm H_2, with $\beta = 4.0$. The regions associated with the outflows and the ionization bicone (northern ionization cone, entrained region, and southern warm arm) yield values of β in a range from 4.5 to 5.4. Finally, the apertures within the rotational disk are more likely dominated by lower-temperature molecular gas, yielding fits with β in a range from 5.6 to 5.7. Overall, we take this stratification of the parameter β throughout the different apertures as evidence that the AGN is transferring excitation energy to the circumnuclear material. Again, we note these values are consistent with the range of measurements reported in previous works (N. L. Zakamska 2010; M. Pereira-Santaella et al. 2014; A. Togi & J. Smith 2016; L. Zhang & L. C. Ho 2023; R. Davies et al. 2024). The estimated $\log[N_{\mathrm{H_2}}/\mathrm{cm}^{-2}]$ from the LTE modeling is highest for the nuclear region, followed by the entrained and west rotational disk apertures.

Within the entrained outflow region of NGC 5506, we observe clearly bifurcated emission for the S(1) through S(5) emission lines, resulting in easily distinguishable rotational and outflowing components of the observed molecular gas. We analyze molecular hydrogen within this region displaying nonrotational behavior (which we presume to be entrained in the outflow) compared to the molecular gas of the rotating disk. Figure 9 depicts the results for the two-component Gaussian fitting of the emission lines as well as the resulting LTE analysis. Generally, the rotational component presents greater flux than the nonrotational outflowing counterpart, and persists into the higher rotational emission lines. To exploit these separable components, we again utilize our single power-law LTE model to fit the relative population levels. Table 4 provides the measured flux for each component (rotational and nonrotational) and the associated LTE fit parameters. We find slight differences in LTE fit to population curves for each component, with a slightly lower value of β and increased estimated $\log[N_{\mathrm{H_2}}/\mathrm{cm}^{-2}]$ for the rotational component relative to the outflowing component (Figure 9).

Because the LTE model provides an estimate of the column density within the aperture, we estimate the outflowing warm (>200 K) H_2 within the aperture (Table 4) to calculate the

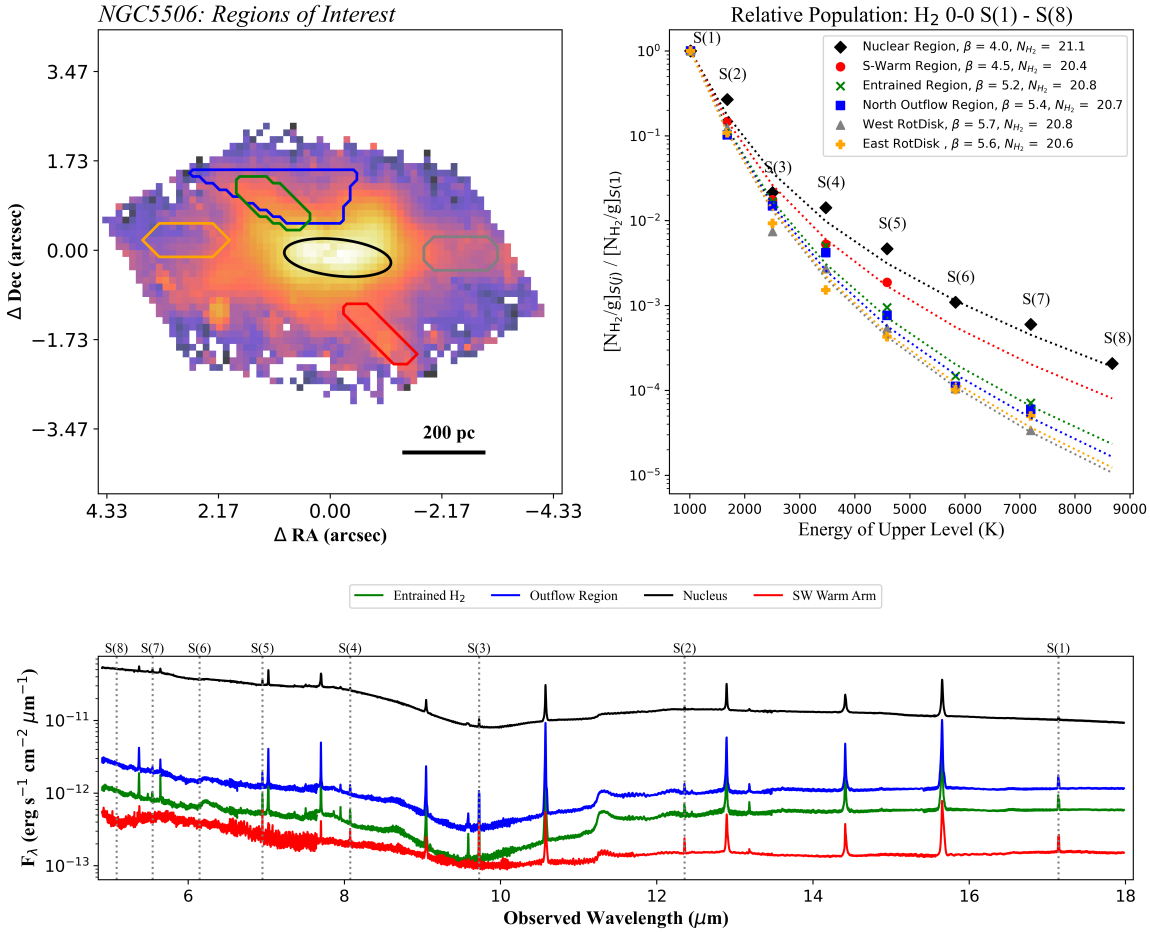

Figure 8. The top-left panel depicts the NGC 5506 H_2 0–0 S(5) normalized line flux and apertures utilized for analysis. The bottom panel depicts the integrated spectra for the associated apertures. Integrated spectra for the rotational disk regions are not displayed as the continuum level is significantly lower than in other apertures. The top-right panel depicts the estimated population levels for each of the associated eight MIR rotational H_2 emission lines and the LTE best fit for each aperture of interest.

warm molecular mass outflow rate. Following A. A. Alonso-Herrero et al. (2023) and F. Esposito et al. (2024), we assume a simple shell geometry for the outflow and calculate the mass outflow rate as

$$\dot{M}_{\rm out}^{\rm mol} = \frac{M_{\rm out}^{\rm mol} v_{\rm out}^{\rm mol}}{R_{\rm out}^{\rm mol}}, \quad (9)$$

where $v_{\rm out}^{\rm mol}$ is the molecular gas velocity and $R_{\rm out}^{\rm mol}$ is the radial distance between the nucleus and the outflowing gas. Because we analyze the flux within a given aperture, we estimate $R_{\rm out}^{\rm mol} \approx$ 245 pc by deprojecting the distance from the galactic center (obtained by fitting a two-dimensional Gaussian to the full continuum spectrum) by 50° (10° outflow inclination angle + the 40° half-opening angle; T. Fischer et al. 2013) and the centroid of the aperture. For $v_{\rm out}^{\rm mol}$, we deproject the average velocity of the S(1) through S(5) nonrotational component (178 km s^{-1}). In doing so, we estimate the mass outflow rate of warm molecular hydrogen to be 0.05 $M_\odot$ yr^{-1}. Applying a correction factor of 1.36 to the total estimated mass to account for helium and heavy metals (see R. Dickman et al. 1986; F. Bigiel et al. 2011), we estimate the total warm molecular mass outflow rate to be 0.07 $M_\odot$ yr^{-1}. This is markedly lower than the average outflow rate of cold molecular gas (8 ± 3 $M_\odot$ yr^{-1}) reported by F. Esposito et al. (2024) for NGC 5506, who used a Galactic CO-to-H_2 conversion factor that may result in an overestimation of the molecular mass, but greater than the hot molecular outflow rate of 0.3 × 10^{-3} $M_\odot$ yr^{-1} estimated by R. A. Riffel et al. (2023). Nonetheless, this could indicate that the majority of outflowing mass is relatively cold gas. We estimate the kinetic power ($\dot{K}$) of the warm molecular outflow as

$$\dot{K}_{\rm out}^{\rm mol} = \frac{1}{2}\dot{M}\, v_{\rm out}^{\rm mol\,2}. \quad (10)$$

Using our estimated mass outflow rate and the deprojected average velocity of the nonrotational component, we estimate the kinetic power of the warm molecular mass to be $\log[\dot{K}/{\rm erg\ s^{-1}}] = 38.8$. With $[L_{\rm AGN}/{\rm erg\ s^{-1}}] = 44.1$ (Table 1; R. Davies et al. 2020), we estimate $\log(\dot{K}/L_{\rm AGN}) = -5.3$. These estimates are lower than those reported for ionized gas by R. Davies et al. (2020) for NGC 5506, who estimated via the ionized gas $\dot{M} = 0.21$ $M_\odot$ yr^{-1}, $\log[\dot{K}_{\rm ion}/{\rm erg\ s^{-1}}] = 40.6$, and $\log[\dot{K}_{\rm ion}/L_{\rm AGN}] = -3.5$. We note that our analysis estimates $M_{\rm H_2} > 200$ K, therefore the inferred molecular mass and AGN warm molecular kinetic power are dependent on the lower-limit temperature selected.

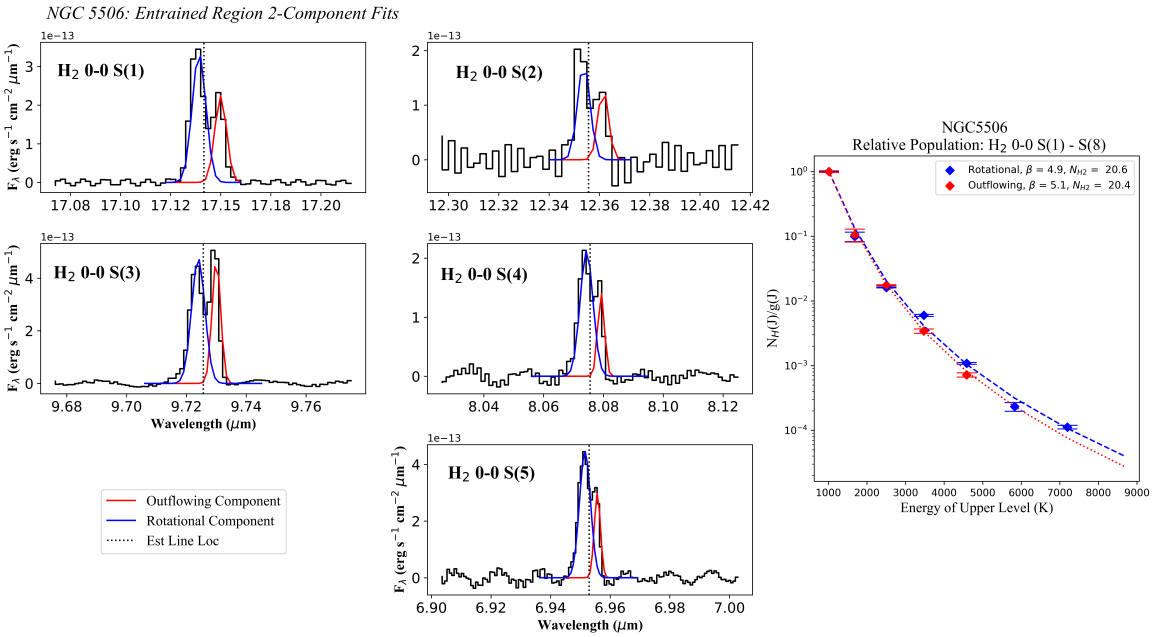

Figure 9. Emission-line fits for the H_2 0–0 S(1) through S(5) two-component Gaussian fits for the entrained aperture in NGC 5506 are displayed in the left panels. The red line indicates the Gaussian fit to the rotational component and the blue line highlights the fit for the nonrotational component. The right panel presents the NGC 5506 estimated population levels for the seven detected MIR rotational H_2 emission lines (we report S(8) as an upper limit) and the LTE best fit for the individual rotational and nonrotational fit components within the entrained aperture.

5.5. The Nuclear Excitation Environment

Emission associated with purely rotational transitions (i.e., tracing the warm gas phase) is likely more representative of the bulk of the molecular material which occupies lower energy levels. Therefore, the warm gas emission is better for tracing the bulk of the molecular material and estimating total molecular mass. While the fraction of molecular mass associated with rovibrational emission (i.e., the hot gas phase) is relatively small, we anticipate it to be more likely tracing H_2 impacted by shocks or harsh radiation fields. Therefore, inclusion of this emission provides a crucial insight into higher-energy interactions between the AGN and molecular gas. We therefore extend our analysis of the nuclear aperture to include the seven rovibrational H_2 NIR emission lines present in VLT/SINFONI observations. Table 5 presents the measured flux for each rovibrational line observed by VLT/SINFONI for NGC 3081 and NGC 5506 within the same nuclear apertures utilized in Section 4.3. Using the methodology described in Section 4.6, we correct for the differential extinction between the NIR and MIR using the T. K. Fritz et al. (2011) extinction curve. Following the same methodology as for the rotational lines (Section 4.2), we estimate the N_j/g_j for each transition. Because of the relatively higher critical densities associated with the rovibrational emission lines, the assumption of LTE is insufficient to model the population levels as it is unlikely that the gas is simply thermalized (R. I. Davies et al. 2005). Therefore, for the full 15 population levels, we employ a non-LTE radiative transfer model (Section 4.4) and compare our estimates to the L. Kristensen et al. (2023) library of shock models (Section 4.5).

5.5.1. NGC 3081: Non-LTE and Shock Model Analysis

For analysis of the nuclear region, incorporating the rovibrational lines from SINFONI/VLT, we correct for the differential extinction between the NIR and MIR following the methodology outlined in Section 4.6. We utilize the observed flux ratio of Pf-α (23.3×10^{-16} erg s^{-1} cm^{-2}) at 7.4599 μm and the Br-γ (18.6×10^{-16} erg s^{-1} cm^{-2}), and estimate $A_{\mathrm{Br}\gamma} = 0.37$. The S(3) emission is most significantly affected, which is impacted by the 10 μm silicate absorption feature. The ratio, S(3)/S(1), is adjusted by a factor of $\approx$1.6. Otherwise, corrections are relatively small, with a differential reddening of $\approx$1.15 between the H_2 1–0 S(1) and H_2 0–0 S(1) emission lines. Figure 10 presents the relative population level estimates including the additional rovibrational lines as well as the best-fit non-LTE radiative transfer modeling (Figure 10, left) and shock models which present a reasonable fit to the data (Figure 10, right). The $\nu = 2$–1 transition lines fail to meet the 3σ S/N threshold for consideration in this analysis, and instead we include estimated upper limits by assuming the average dispersion of the $\nu = 1$–0 emission lines and 3 times the standard deviation of the continuum window as the assumed amplitude of the emission line. Upper limits were not included in the model fitting (Table 5). The non-LTE model provides a relatively good fit to the full suite of estimated population levels (Figure 10, top left) and yields a similar estimate as the LTE model for β (4.3) and the same estimate for $\log[N_{\mathrm{H}_2}/\mathrm{cm}^{-2}] = (20.6)$ for the nuclear region. The non-LTE model suggests an environment in which the number densities of free molecular and atomic hydrogen are $\log[n_{\mathrm{H}_2}/\mathrm{cm}^{-3}] = 6.5$ and $\log[n_{\mathrm{H}}/\mathrm{cm}^{-3}] = 2.1$, respectively.

Comparison with the L. Kristensen et al. (2023) shock models also provides a reasonable fit to the data. The shock model best fit (lowest χ^2) yields a J-type shock scenario which propagates at a velocity $V_s = 5$ km s^{-1} through an environment with a hydrogen density $\log[n_{\mathrm{H}} / \mathrm{cm}^{-3}] = 3$. The best-fit model indicates a transverse magnetic field ($b = 0.1$, $B = 3.2$ μG) and a UV radiation field ($G_0 = 100$). This model provides a relatively good fit for both the rotational

Table 4
NGC 5506 Measured Line Flux for the H_2 0–0 S(1) through S(8) Emission for the Rotational and Nonrotational Fit Components

Emission Line	λ_{rest} (μm)	Rotational Component	Entrained	Rotational Component	Entrained
		Flux (10^{-16} erg s^{-1} cm^{-2})		Velocity (km s^{-1})	
H_2 0–0 S(1)	17.035	28.94 ± 0.45	16.63 ± 0.48	−42 ± 1	147 ± 1
H_2 0–0 S(2)	12.279	9.80 ± 1.65	5.97 ± 1.24	−44 ± 7	141 ± 14
H_2 0–0 S(3)	9.6649	26.52 ± 0.42	16.52 ± 0.30	−51 ± 1	135 ± 1
H_2 0–0 S(4)	8.0251	12.51 ± 0.43	4.11 ± 0.29	−44 ± 2	139 ± 2
H_2 0–0 S(5)	6.9095	20.29 ± 0.54	7.72 ± 0.52	−59 ± 3	119 ± 3
H_2 0–0 S(6)	6.1086	3.60 ± 0.54	⋯	−48 ± 23	⋯
H_2 0–0 S(7)	5.5112	11.32 ± 0.91	⋯	−43 ± 10	⋯
LTE Fit Parameters					
β	⋯	4.9 ± 0.2	5.1 ± 0.1	⋯	⋯
$\log[N_{H_2}/\mathrm{cm}^{-2}]$	⋯	20.6 ± 0.1	20.4 ± 0.04	⋯	⋯
$\log[M_{H_2}/M_\odot]$	⋯	$5.0^{+0.5}_{-0.6}$	$4.7^{+1.0}_{-1.1}$	⋯	⋯

Note. The associated LTE model best-fit parameters, as well as the total estimated molecular mass, are also included.

Table 5
Measured Emission-line Flux for Each of the NIR Rovibrational Lines within the Nuclear Apertures for NGC 3081 and NGC 5506 (1.46 and 1.16 sq. ″, Respectively)

Emission Line	λ_{rest} (μm)	NGC 3081	NGC 5506
		Flux (10^{-16} erg s^{-1} cm^{-2})	
H_2 1–0 S(0)	2.2235	5.39 ± 0.49	47.01 ± 6.50
H_2 1–0 S(1)	2.1218	20.42 ± 0.63	77.56 ± 5.14
H_2 1–0 S(2)	2.0338	9.16 ± 1.36	24.78 ± 6.99
H_2 1–0 S(3)	1.9576	26.32 ± 1.55	57.71 ± 9.96
H_2 2–1 S(1)	2.2477	<1.69	<27.42
H_2 2–1 S(2)	2.1542	<4.29	<41.69
H_2 2–1 S(3)	2.0735	<1.82	7.53 ± 2.48

and $\nu = 1$–0 rovibrational transition lines; however, the model struggles to fully incorporate the $\nu = 1$–0 population levels. The shock model fits the rotational lines reasonably well. A secondary shock scenario, which models our observations, is presented in the top-right panel of Figure 10 as blue × points. This represents an environment in which a faster CJ-type shock (V_s = 60 km s^{-1}) driven by a stronger transverse magnetic field (b = 3.0, B = 30 μG) permeates through hydrogen gas of density $\log[n_H/\mathrm{cm}^{-3}] = 2$ with a significantly weaker UV radiation field ($G_0 = 0.1$). This secondary scenario does a better job at matching our observations of the $\nu = 1$–0 population levels, but poorly matches the S(7) and S(8) rotational population levels.

Both the non-LTE radiative transfer and shock models provide a relatively good fit to our observations. This suggests that excitation of H_2 within the nuclear region could be explained by a non-LTE radiative transfer environment, as a result of shock excitation, or a combination of the two. Informed by the strong correlation between nuclear excitation energy and [Ne V]$_{14.322\mu m}$ (Section 5.2) and relatively weak correlation with [Fe II]$_{5.34\mu m}$ (Section 5.2), we favor the interpretation that excitation is primarily the result of the AGN photoionizing the local molecular gas. Shock excitation may also contribute, as our measurements integrate over an extended region that may encompass multiple excitation mechanisms. Recent JWST/MIRI imaging of the extended dust indicates that AGN illumination alone is not enough to account for extended dust up to 100 pc from the nucleus, indicating the presence of additional heating mechanisms (H. Haidar et al. 2025, in preparation).

5.5.2. NGC 5506: Non-LTE and Shock Model Analysis

We incorporate the seven additional rovibrational lines visible to VLT/SINFONI to further assess excitation within the nuclear aperture of NGC 5506. Table 5 provides the measured line flux for each of the rovibrational H_2 emission lines. We again attempt to address the differential extinction between the MIR and NIR using the T. K. Fritz et al. (2011) extinction curve and the ratio of the observed Br-γ (719.2 ± 15.6 × 10^{-16} erg s^{-1} cm^{-2}) to Pf-α (177.9 × 10^{-16} erg s^{-1} cm^{-2}) line flux. However, as a result of the abnormally elevated ratio of Br-γ to Pf-α, this provides an unsatisfactory correction to the differential extinction. We suggest this to be the result of high levels of AGN photoionization in the nuclear region boosting Br-γ emission. Previous work has highlighted the potential for AGN photoionization to drive hydrogen recombination emission in a postshock nuclear environment (L. R. Holden et al. 2023). We expect this effect may be present and impacting our extinction correction. To adjust for this, we assume the T. K. Fritz et al. (2011) curve to be valid, but instead calculate the relative extinction using Br-γ and the observed Pa-α line flux (4271.0 ± 161.8 × 10^{-16} erg s^{-1} cm^{-2}), both NIR hydrogen recombination lines which we assume will be similarly affected by AGN photoionizing radiation. Following this, we estimate $A_{Br\gamma} = 0.77$. This results in an adjustment of ≈2.7 to S(3)/S(1). Otherwise, corrections are relatively minor, with a differential reddening of ≈1.31 between the H_2 1–0 S(1) and H_2 0–0 S(1) emission lines.

The bottom panels of Figure 10 depict the relative population levels as well as the best non-LTE fit and best-fit shock models. Through visual inspection of the S(3) population level (impacted by a silicate absorption feature), we infer that our extinction correction is valid. We note the $\nu = 1$–0 S(0) population level is significantly elevated in relation to the other rovibrational population levels. This staggered

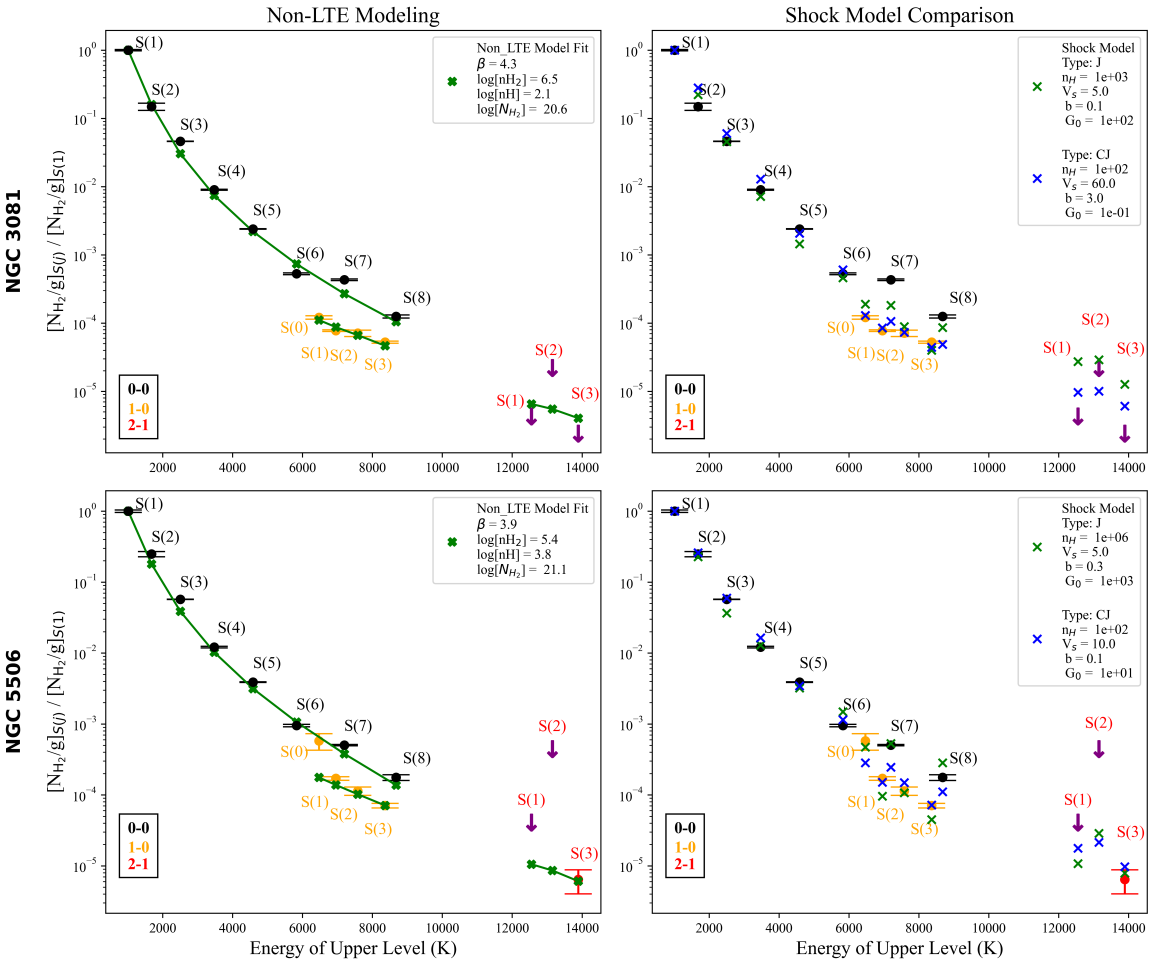

Figure 10. The top panels present NGC 3081 relative population levels estimated for the full set of rotational and rovibrational emission. The left panel presents the best-fit non-LTE radiative transfer model. The right panel depicts two shock scenarios which provide a reasonably good fit to the population level estimates. In this figure, the modeled $\nu = 2$–1 transition lines have been included although no measurements above the 3σ S/N threshold are available. The bottom panels present NGC 5506 relative population levels estimated for the full set of rotational and rovibrational emission. The left panel presents the best-fit non-LTE radiative transfer model. The right panel depicts two shock scenarios which provide a reasonably good fit to the population level estimates.

presentation of the $\nu = 1$–0 S(0) population level could be indicative of a nuclear environment in which the OPR < 3, suggesting that an external excitation mechanism is likely present. One potential explanation that has been previously suggested (R. I. Davies et al. 2005; R. Davies et al. 2024) could be photoionization from AGN radiative energy making the nucleus a photon-dominated region (PDR). In this case, within the nuclear PDR UV and X-ray radiation from the AGN photoionizes the hot molecular gas and provides a significant contribution to emission in the NIR. However, we would also anticipate an elevated S(2) population level, which we do not observe in our data. The warm molecular gas phase, emitting in the MIR, exhibits a smooth curve consistent with an OPR $\approx$ 3 and well modeled by both our single power-law LTE and non-LTE radiative transfer models. This could suggest that the warm molecular gas is located in a denser region further from the SMBH and relatively shielded from the AGN radiative feedback. As a result, thermalization and radiative transfer processes may be the dominant excitation mechanism for molecular hydrogen emitting in the MIR. A nuclear PDR is consistent with previous studies which highlighted a nuclear deficiency of cool molecular material (S. García-Burillo et al. 2021, 2024) and with our observed elevated ratio of Br-γ and Pf-α resulting in an inadequate measurement of the relative extinction parameter $A_{\mathrm{Br}\gamma}$.

With the inclusion of the NIR emission-line measurements, we compare our estimated population levels to the non-LTE radiative transfer model (Figure 10, bottom left) and to the L. Kristensen et al. (2023) library of shock models (Figure 10, bottom right). The best-fit non-LTE model results in a somewhat steeper curve ($\beta = 3.9$) and the same column density ($\log[N_{\mathrm{H}_2}/\mathrm{cm}^{-2}] = 21.1$) as to what was estimated by assuming LTE. This fit requires an environment with atomic and molecular hydrogen densities of $\log[n_{\mathrm{H}}/\mathrm{cm}^{-3}] = 3.8$ and $\log[n_{\mathrm{H}_2}/\mathrm{cm}^{-3}] = 5.4$, respectively. The model does a reasonable job at fitting the rotational lines and much of the rovibrational lines, but fails to explain the elevated $\nu = 1$–0 S(0) population level.

The best-fit shock models from the L. Kristensen et al. (2023) library fit the estimates relatively well and are more successful at incorporating the rovibrational population levels. The shock model best fit (lowest χ^2; green $\times$ points in Figure 10, bottom-right panel) yields a J-type shock scenario which propagates ($V_s = 5$ km s^{-1}) through a hydrogen environment ($\log[n_{\mathrm{H}} / \mathrm{cm}^{-3}] = 6$) with a transverse magnetic field ($b = 0.3$, $B = 3$ μG) and an environment with a UV

radiation field ($G_0 = 1000$). Population level estimates are relatively well fit, with some deviation for the ν =1–0 S(1) and S(3) populations. Again, because of the number of model free parameters, we highlight a secondary shock scenario which fits our observations (blue × points in Figure 10, bottom-right panel). In contrast, this CJ-type shock scenario propagates with a slower velocity ($V_s = 10$ km s^{-1}) through a less dense hydrogen environment ($\log[n_{\rm H} / {\rm cm}^{-3}] = 2$) with a weaker UV radiation field ($G_0 = 10$) and transverse magnetic field ($b = 0.1$, $B = 3.2$ μG).

While both the non-LTE radiative transfer and shock models are capable of reproducing the full set of 15 rotational and rovibrational population levels, a shock scenario is better at explaining the observed $\nu = 1$–0 S(0) population level. From this observation, in concert with the spatial correlation between [Fe II]$_{5.34\mu{\rm m}}$ and radio emission with higher rotational H_2 emission and the apparently bolstered hydrogen recombination emission (Br-γ), we conclude that shocks are a dominant excitation mechanism within the nuclear region of NGC 5506. It is challenging to fit the full suite of rotational and rovibrational population levels as the nuclear aperture that we utilize may integrate over changing environments with alternative excitation mechanisms. The warm H_2, being well modeled by both the LTE and non-LTE models, may indicate that this gas is thermalized and that shocks primarily impact higher excitation states. We speculate that the postshock environment may be similar to that proposed by L. R. Holden et al. (2023), in which the postshock gas has stratified excitation phases (see Figure 16 of L. R. Holden et al. 2023), the first of which (most distant from the AGN) is the postshock warm ionized gas, followed by warm H_2 (rotational emission), then cold molecular gas, and finally warm/hot gas being irradiated by the AGN (pumping the emission of hydrogen recombination lines in a PDR). We find this to be a plausible schematic for the postshock environment and congruent with our observations. Further, this scenario, with molecular gas in the most central region being irradiated and heated by the AGN, provides a potential explanation for the contrast of very low CCI (indicating a nuclear deficiency of cold molecular gas) and relatively high HCI (indicating no nuclear deficiency of hot molecular gas) reported for NGC 5506 by S. García-Burillo et al. (2021, 2024). In this scenario, the cool molecular gas which would be in the immediate postshock nuclear region ($r < 50$ pc) is being heavily irradiated and heated by the AGN, resulting in an apparent nuclear deficiency of cold gas and a surplus of hot molecular gas.

6. Summary and Discussion

NGC 3081 and NGC 5506, while both local Universe Seyfert-type galaxies (Seyfert 2 and 1.9/1i, respectively), show marked behavioral differences in their interactions between the circumnuclear H_2 and the central AGN. Despite NGC 3081 and NGC 5506 being similar in Seyfert type, distance, and L_{14-195} keV X-ray luminosity, the underlying mechanisms through which the AGN transfers excitation energy to the surrounding molecular material is inherently different. NGC 3081, based on the flux distribution of molecular and ionized gas, appears to be relatively orderly, largely exciting H_2 via photoionization within a limited range (≈330 pc). In contrast, the excitation derived from the AGN of NGC 5506 (based on the correlated flux distribution of [Fe II]$_{5.34\mu{\rm m}}$ and H_2 0–0 S(1) through S(8) emission, the elevated ratio of Br-γ and Pf-α, and nuclear population level modeling) is largely shock associated and motivates the postshock environment proposed by L. R. Holden et al. (2023). We find that these conclusions complement previous studies of these targets, and provide further insight into disentangling the impacts of AGN feedback—be they molecular outflows driven by an interaction between the ionization cone and disk of NGC 5506 (F. Esposito et al. 2024), the physical conditions of a postshock environment (L. R. Holden et al. 2023), regions of highly disturbed gas as identified by L. Zhang et al. (2024b), or a potential coupling between the CCI and HCI (S. García-Burillo et al. 2021, 2024) and feedback mechanisms. We find the last of these particularly interesting, with the reported deficiency of cool and particularly hot molecular gas for NGC 3081 compared to the deficiency of cool gas and excess hot gas in the nuclear region of NGC 5506. We speculate that AGN-driven shocks may be a control on these distributions.

In this work, we have utilized observations from both JWST/MIRI and VLT/SINFONI to investigate the behavior and excitation of circumnuclear molecular gas in NGC 3081 and NGC 5506, two Seyfert galaxies from the GATOS sample. We have analyzed N_i/g_i for a suite of rotational and rovibrational H_2 emission lines in the MIR and NIR, and compared population level estimates for different circumnuclear apertures to LTE, non-LTE, and shock modeling. Our work shows as follows:

1. NGC 3081 presents a centrally concentrated excitation energy with some elongation along the axis of the ionization cones. The molecular gas temperature in the nuclear region is well traced by [Ne V]$_{14.322\mu{\rm m}}$, suggesting that AGN radiative feedback is the primary excitation mechanism for the molecular gas.
2. NGC 5506 presents a centrally concentrated excitation energy with significant elongation along the ionization cone. The molecular gas temperature in the circumnuclear gas appears to be spatially correlated with [Fe II]$_{5.34\mu{\rm m}}$ emission, suggesting that shock excitation is a dominant mechanism in the nuclear region.
3. LTE modeling for the nuclear and circumnuclear regions of NGC 3081 yield values of β consistent with previous studies on similar-type objects (M. Pereira-Santaella et al. 2014; A. Togi & J. Smith 2016; L. Zhang & L. C. Ho 2023; R. Davies et al. 2024). We find that β values become consistent for apertures outside the nuclear region, indicating a limited range of AGN influence on the circumnuclear material. LTE modeling along the axis of the ionization bicone indicates the extent of the influence of the ionization bicone to be ≈330 pc with a relatively smoothly decreasing $\log[N_{\rm H_2}/{\rm cm}^{-2}]$ gradient.
4. LTE modeling for the nuclear and circumnuclear regions of NGC 5506 yield thermal scaling parameters β consistent with what has been observed in other nearby Seyfert galaxies (M. Pereira-Santaella et al. 2014; A. Togi & J. Smith 2016; R. Davies et al. 2024). We report clear stratification for the best-fit β for the nuclear region, ionization/outflow cone associated regions, and regions within the rotational disk, indicating the AGN is actively transferring excitation energy to the circumnuclear gas.

5. The nuclear population levels NGC 3081 generated from the eight rotational and four measured rovibrational emission lines are well modeled by a single power-law non-LTE radiative transfer model and relatively well by a shock scenario.
6. The non-LTE radiative transfer model yields a moderate fit for population levels estimated from the eight rotational and five measured rovibrational lines for the nuclear region of NGC 5506, poorly incorporating the population levels of the rovibrational emission. The L. Kristensen et al. (2023) shock models provide a good fit to the population levels and is better at incorporating the rovibrational derived population levels, indicating that shocks are a likely excitation mechanism within the nuclear region.
7. We identify nonrotational behavior of H_2 spatially coincident with the northeastern edge of the ionization bicone of NGC 5506. We suggest that this H_2 is entrained within the AGN outflow, resulting from weak coupling between the northern ionization cone and the rotational disk, as was proposed in F. Esposito et al. (2024) using ALMA observations of the cold H_2. We estimate a lower-limit deprojected velocity of 178 km s^{-1} for the nonrotational gas, and assuming a shell geometry estimate a mass outflow rate of 0.07 $M_{\odot}$ yr^{-1}, consistent with ionized outflow rates reported in the literature (R. Davies et al. 2020; M. Bianchin et al. 2022; R. A. Riffel et al. 2023).

At this juncture, it is not clear what environmental conditions result in shock events, or if shock events are a necessity for facilitating molecular outflows. While this work has made strides in understanding the AGN's relationship to the circumnuclear molecular gas, the two objects selected for this analysis highlight different types of AGN behavior which influence the circumnuclear gas. In subsequent work, we will expand this analysis to the full GATOS sample in an effort to constrain what sort of behavior is typical. A more general understanding across a larger sample may reveal a new axis of physical characteristics along which AGN can be segregated, such as those in which shock events strongly impact the circumnuclear environment (e.g., NGC 5506) and those which display more consistent orderly behavior (e.g., NGC 3081). The underlying driving mechanisms behind AGN shocks are still largely unknown. Thus, constraining the type and prevalence of nuclear shock environments across a broader sample may yield insights into the underlying mechanisms which mediate AGN activity.

Acknowledgments

We thank the referee for their detailed and useful comments, which have greatly improved this article. This research utilized the unique and powerful tools included within Astropy, a community-developed python package (T. P. Robitaille et al. 2013). D.D., L.Z., C.P., and E.K.S.H acknowledge grant support from the Space Telescope Science Institute (ID: JWST-GO-01670). D.D. and E.K.S.H. acknowledge support from the NASA Astrophysics Data Analysis Program (22-ADAP22-0173). M.P.S. acknowledges support under grant Nos. RYC2021-033094-I, CNS2023-145506, and PID2023-146667NB-I00, funded by MCIN/AEI/10.13039/501100011033 and the European Union NextGenerationEU/PRTR. A.A.H. and L.H.M. acknowledge support from grant No. PID2021-124665NB-I00 funded by MCIN/AEI/10.13039/501100011033 and by ERDF, "A way of making Europe." E.B. acknowledges support from Spanish grant Nos. PID2022-138621NB-I00 and PID2021-123417OB-I00, funded by MCIN/AEI/10.13039/501100011033/FEDER, EU. A.A. acknowledges support from the European Union (Widening Participation, ExGal-Twin, GA 101158446). C.R.A. and A.A. acknowledge support from the Agencia Estatal de Investigación of the Ministerio de Ciencia, Innovación y Universidades (MCIU/AEI) under the grant "Tracking active galactic nuclei feedback from parsec to kiloparsec scales," with reference PID2022-141105NB-I00 and the European Regional Development Fund (ERDF). S.G.B., acknowledges support from Spanish grant No. PID2022-138560NB-I00, funded by MCIN/AEI/10.13039/501100011033/FEDER, EU. I.G.B. is supported by the Programa Atracción de Talento Investigador "César Nombela" via grant No. 2023-T1/TEC-29030 funded by the Community of Madrid. D.E.A. is supported by the "Becas Estancias Posdoctorales por México" EPM(1) 2024 (CVU: 592884) program of SECIHTI and acknowledges financial support from PAPIIT UNAM IN109123 and "Ciencia de Frontera" CONAHCyT CF2023-G100.

Facilities: JWST (MIRI), VLT:Yepun (SINFONI).

Software: Astropy (T. P. Robitaille et al. 2013).

Appendix
Appendix A

This appendix acts to supplement the manuscript by presenting the flux, velocity, and σ maps for each of the rotational H_2 and emission lines measured as well as neon lines. Figures A1–A20 present both the primary and secondary components of the fitting algorithm described in Section 4.1. In the presented line maps and velocity fields, spaxels with line fluxes below three times the local noise were masked. Additionally, spaxels with velocity and σ measurements in excess of ± 800 km s^{-1} have been masked. For the H_2 0–0 S(7) emission and kinematic maps, a more stringent blueward velocity threshold has been imposed in order to mitigate contamination of the [Mg VII]$_{5.503\mu m}$ emission line, which is adjacent to the H_2 0–0 S(7) emission line.

A.1. NGC 3081 Additional Line Maps

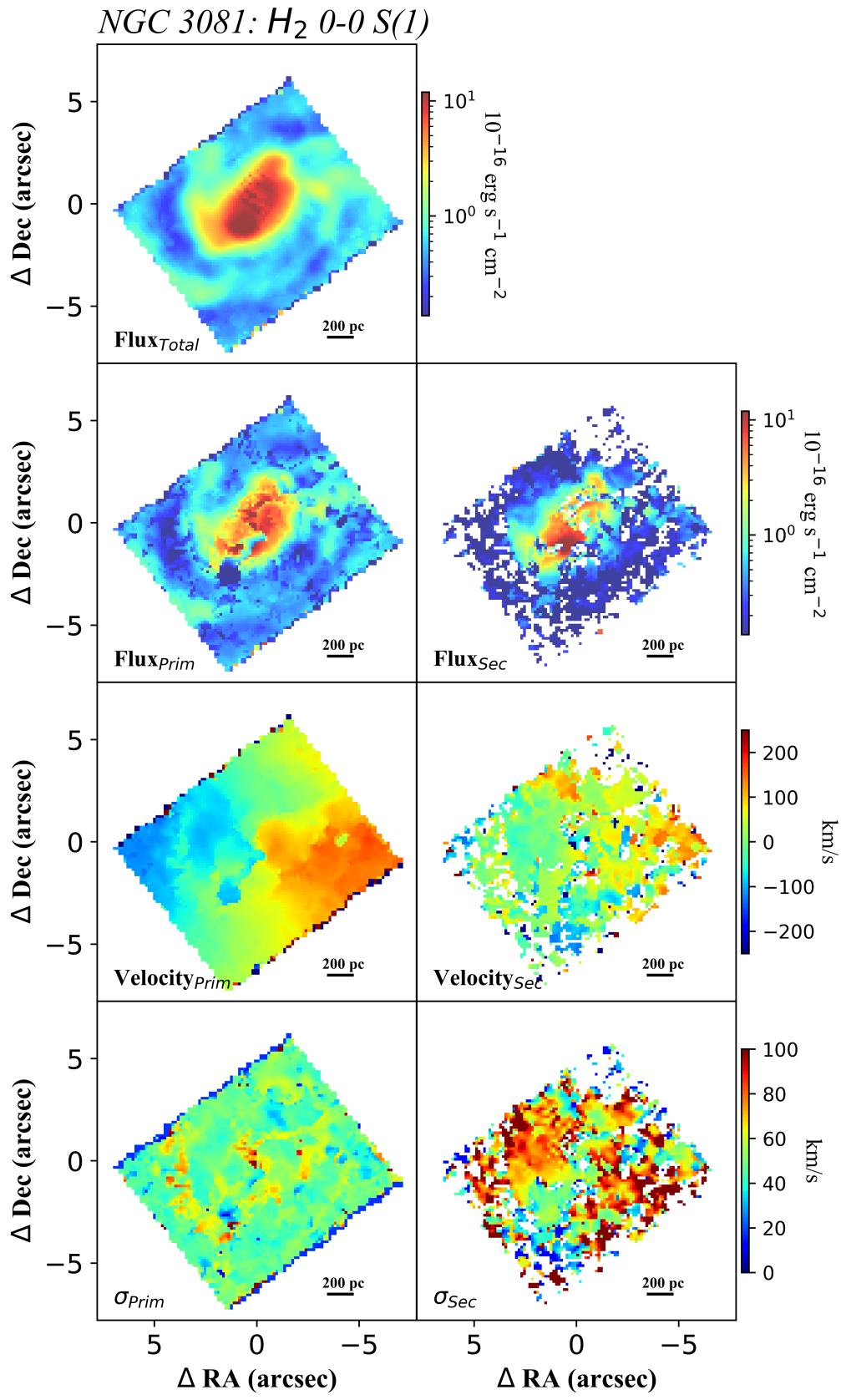

Figure A1. Flux distribution and kinematics for NGC 3081 H_2 0–0 S(1) emission. The left column presents the primary/rotational component for the two-component fit, and the right column presents the secondary/outflowing fit component.

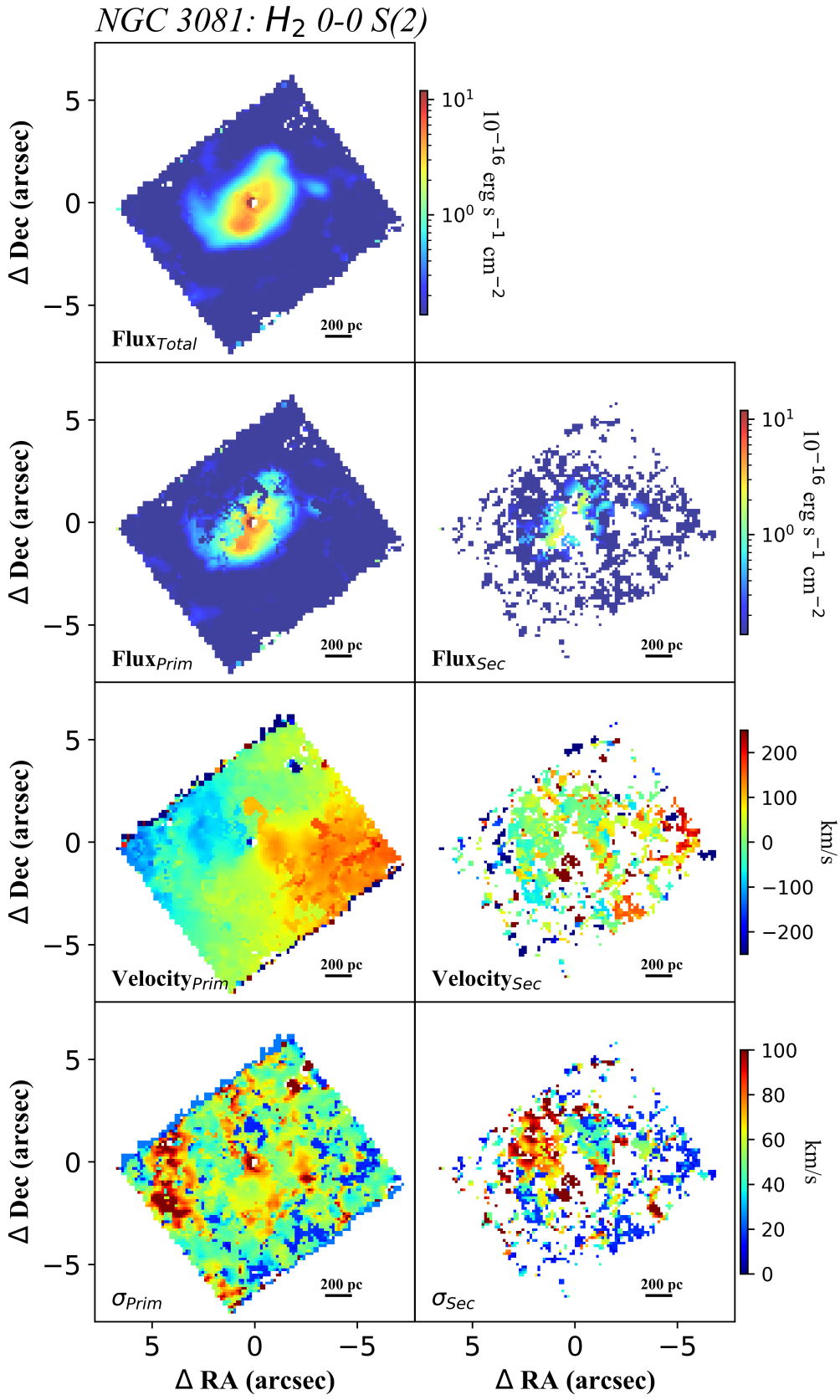

Figure A2. Flux distribution and kinematics for NGC 3081 H_2 0–0 S(2) emission. The left column presents the primary/rotational component for the two-component fit, and the right column presents the secondary/outflowing fit component.

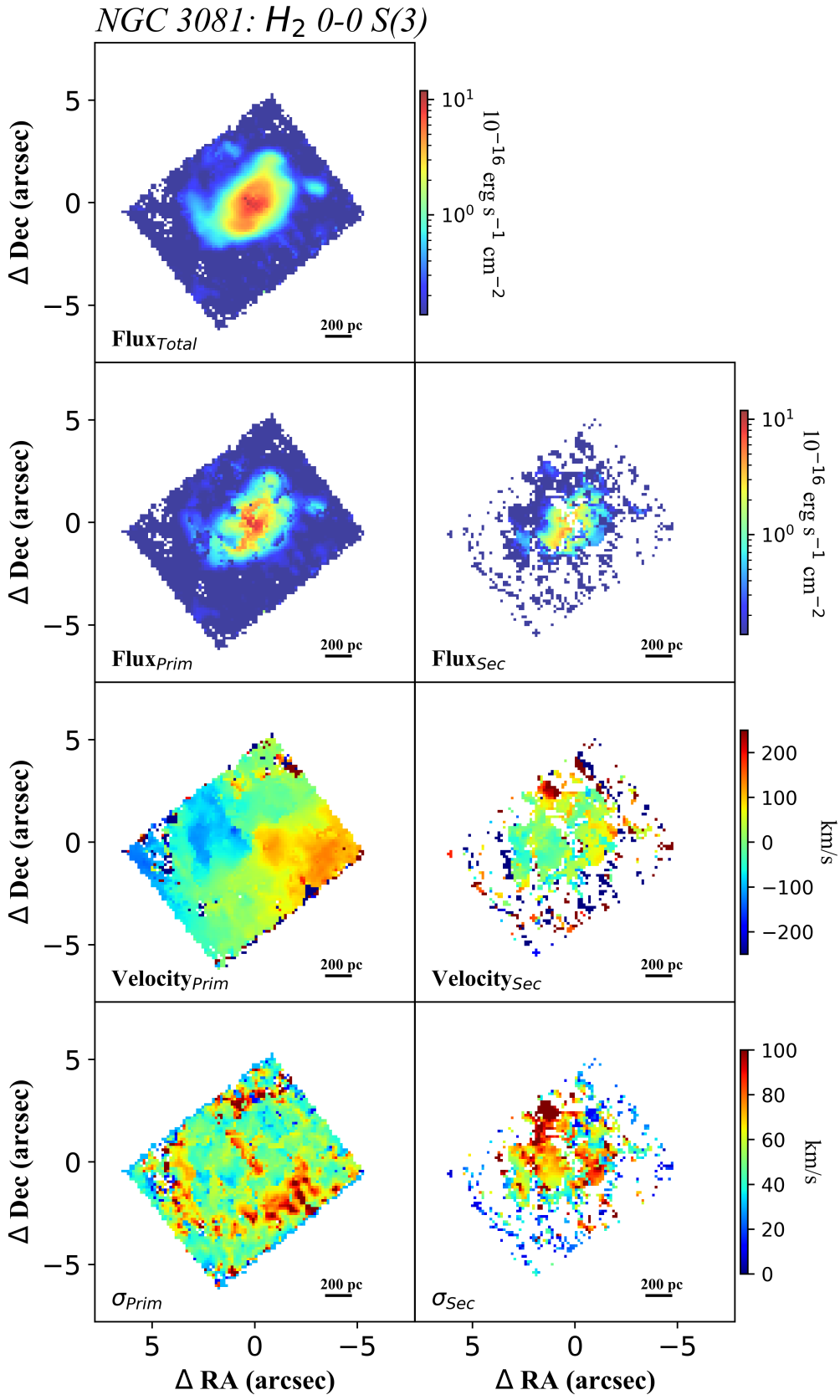

Figure A3. Flux distribution and kinematics for NGC 3081 H_2 0–0 S(3) emission. The left column presents the primary/rotational component for the two-component fit, and the right column presents the secondary/outflowing fit component.

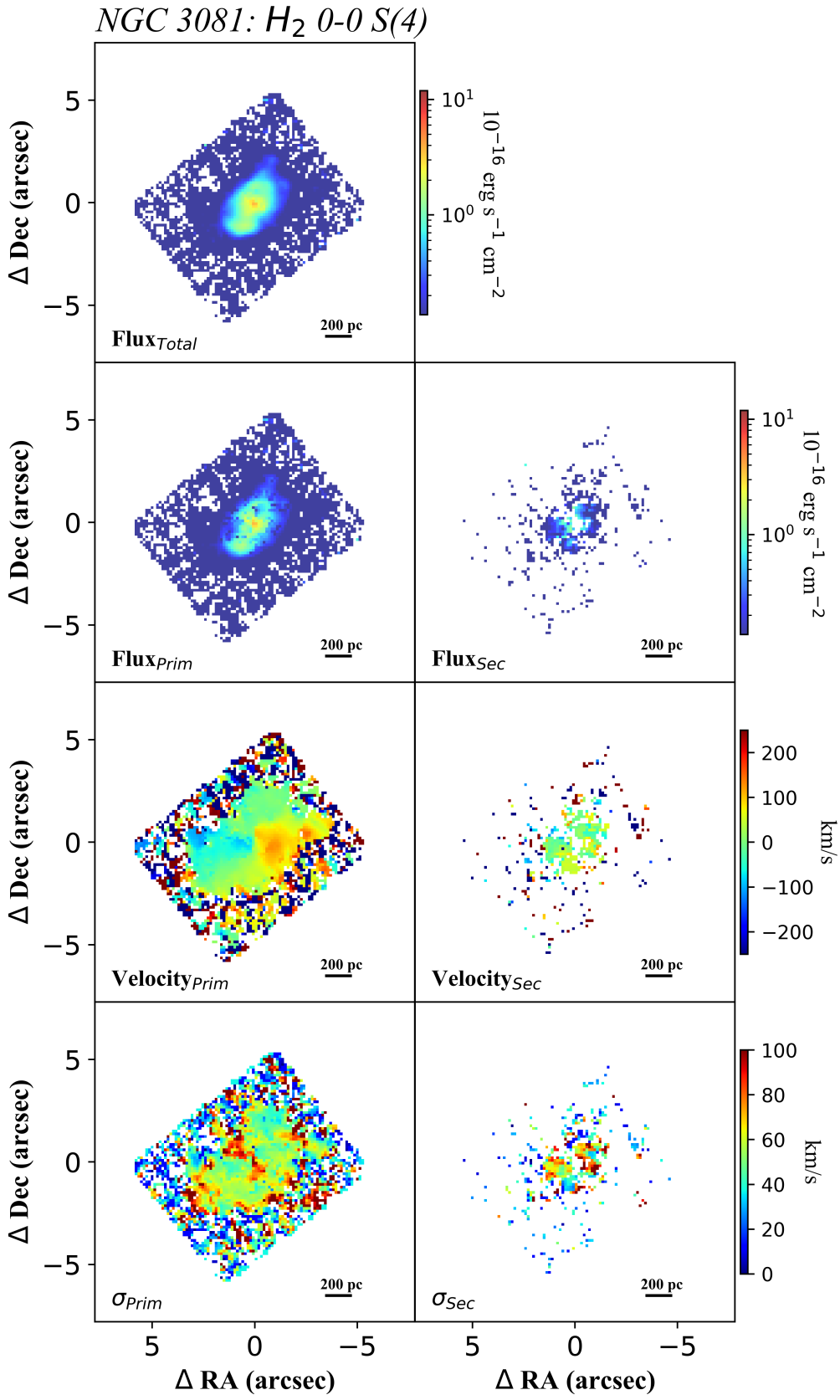

Figure A4. Flux distribution and kinematics for NGC 3081 H_2 0–0 S(4) emission. The left column presents the primary/rotational component for the two-component fit, and the right column presents the secondary/outflowing fit component.

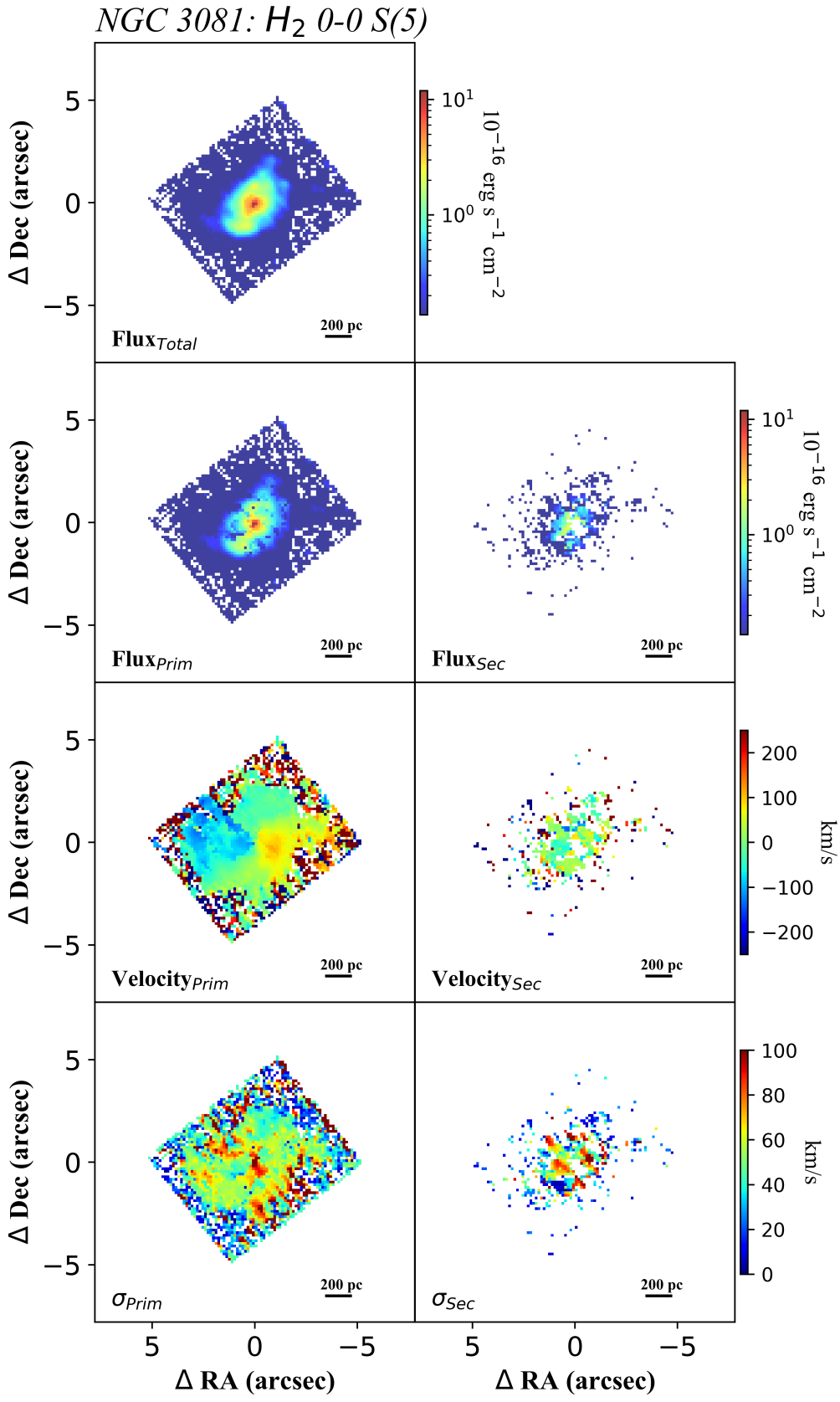

Figure A5. Flux distribution and kinematics for NGC 3081 H_2 0–0 S(5) emission. The left column presents the primary/rotational component for the two-component fit, and the right column presents the secondary/outflowing fit component.

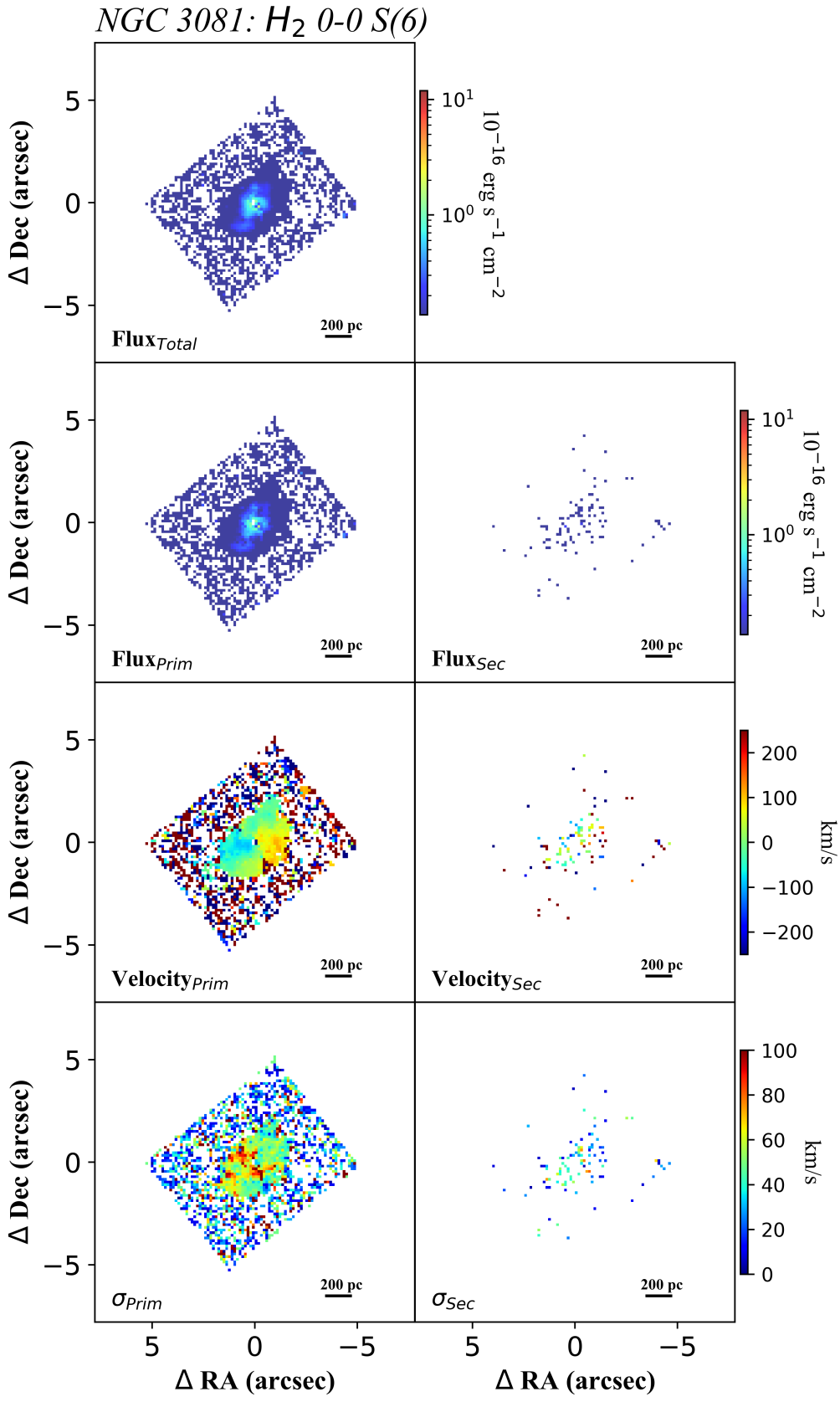

Figure A6. Flux distribution and kinematics for NGC 3081 H_2 0–0 S(6) emission. The left column presents the primary/rotational component for the two-component fit, and the right column presents the secondary/outflowing fit component.

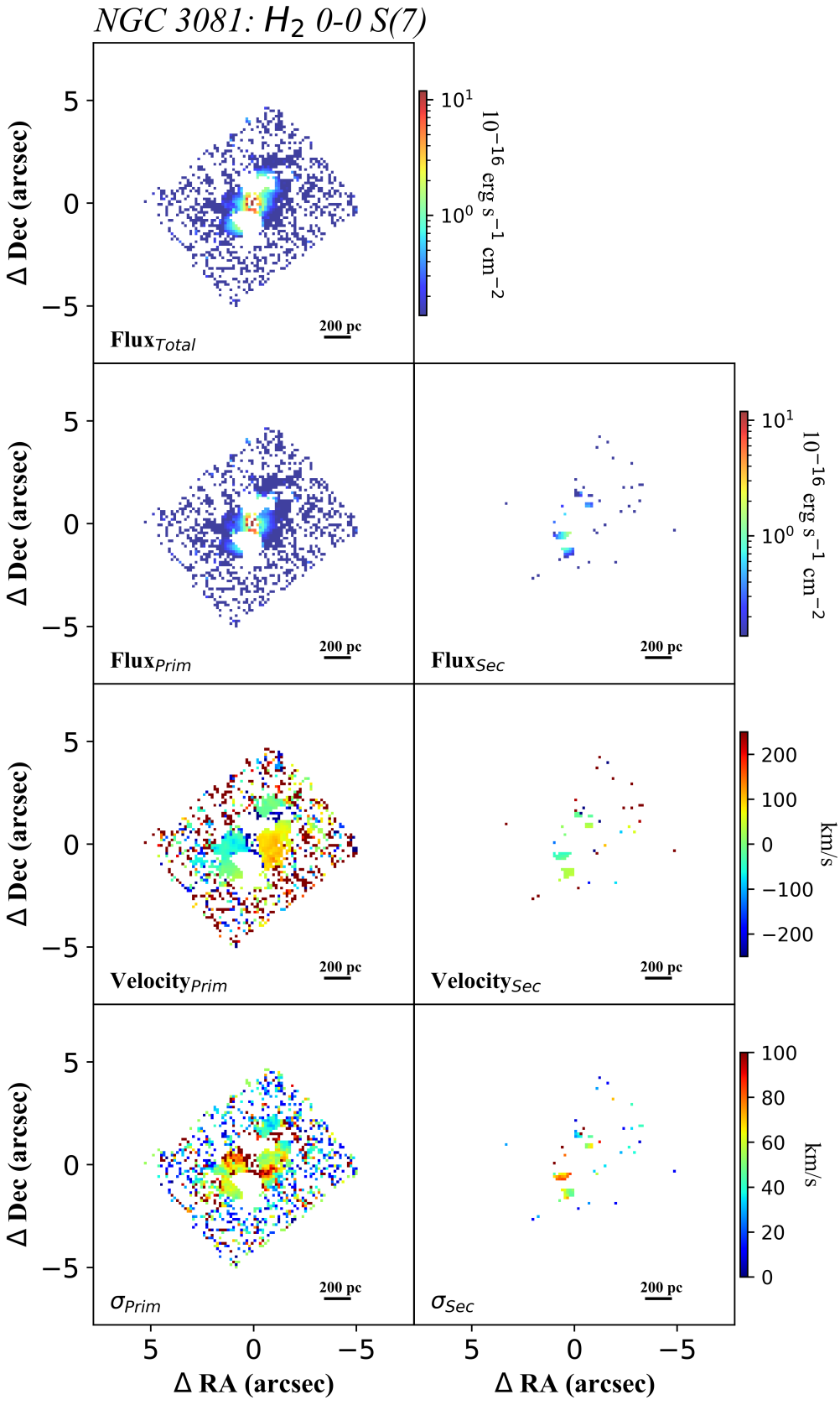

Figure A7. Flux distribution and kinematics for NGC 3081 H_2 0–0 S(7) emission. The left column presents the primary/rotational component for the two-component fit, and the right column presents the secondary/outflowing fit component.

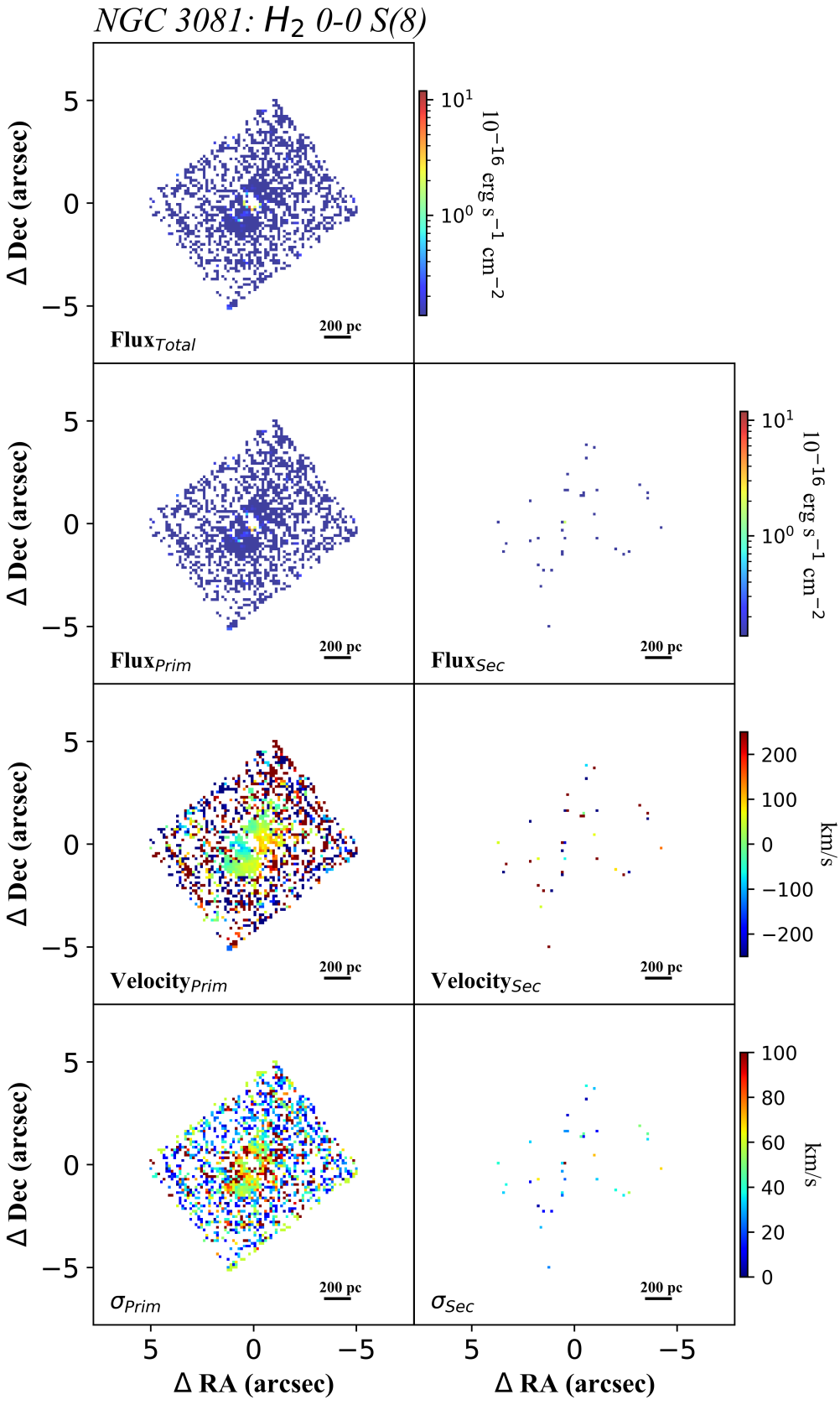

Figure A8. Flux distribution and kinematics for NGC 3081 H_2 0–0 S(8) emission. The left column presents the primary/rotational component for the two-component fit, and the right column presents the secondary/outflowing fit component.

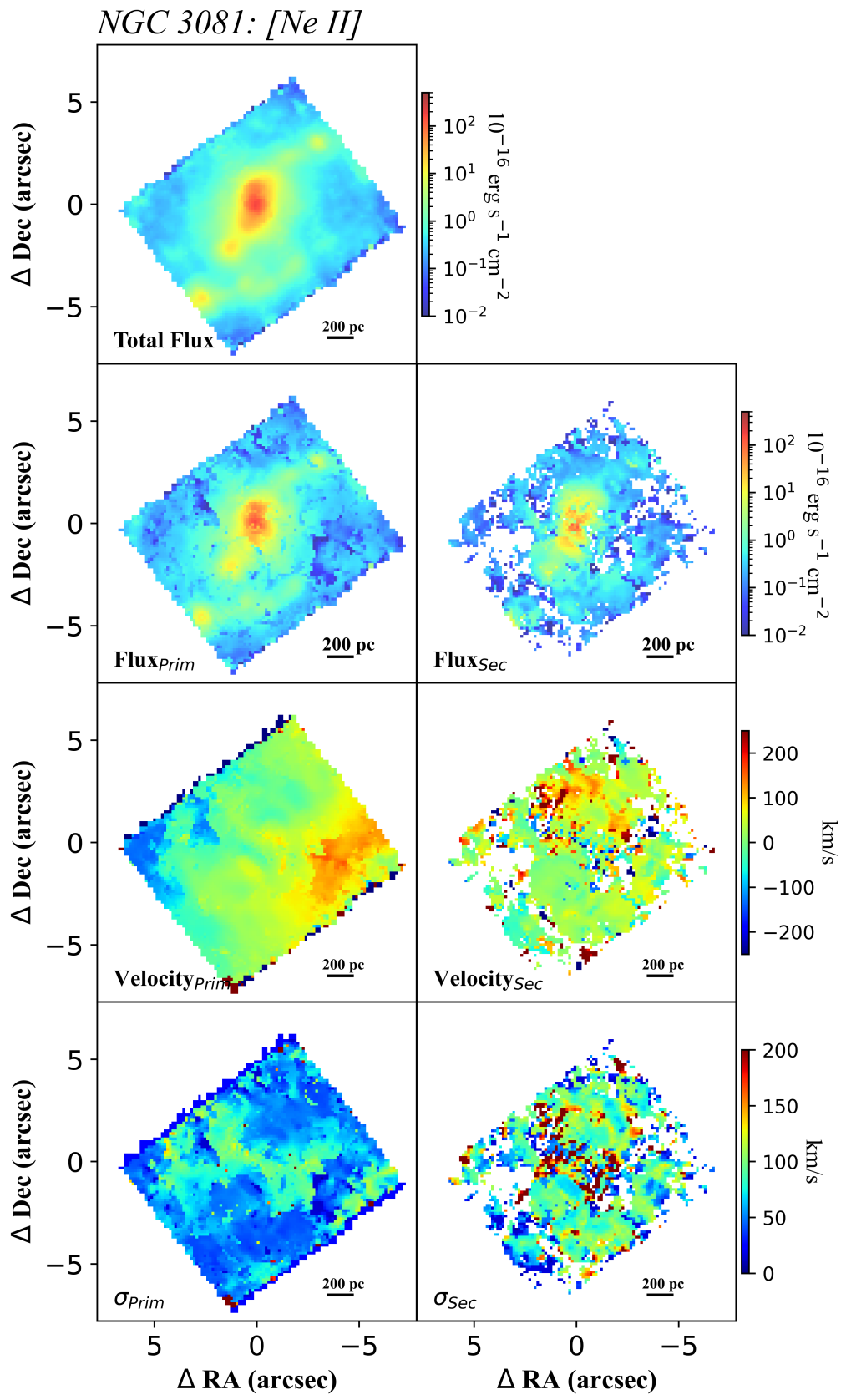

Figure A9. Flux distribution and kinematics for NGC 3081 [Ne II]$_{12.814\mu m}$ emission. The left column presents the primary/rotational component for the two-component fit, and the right column presents the secondary/outflowing fit component.

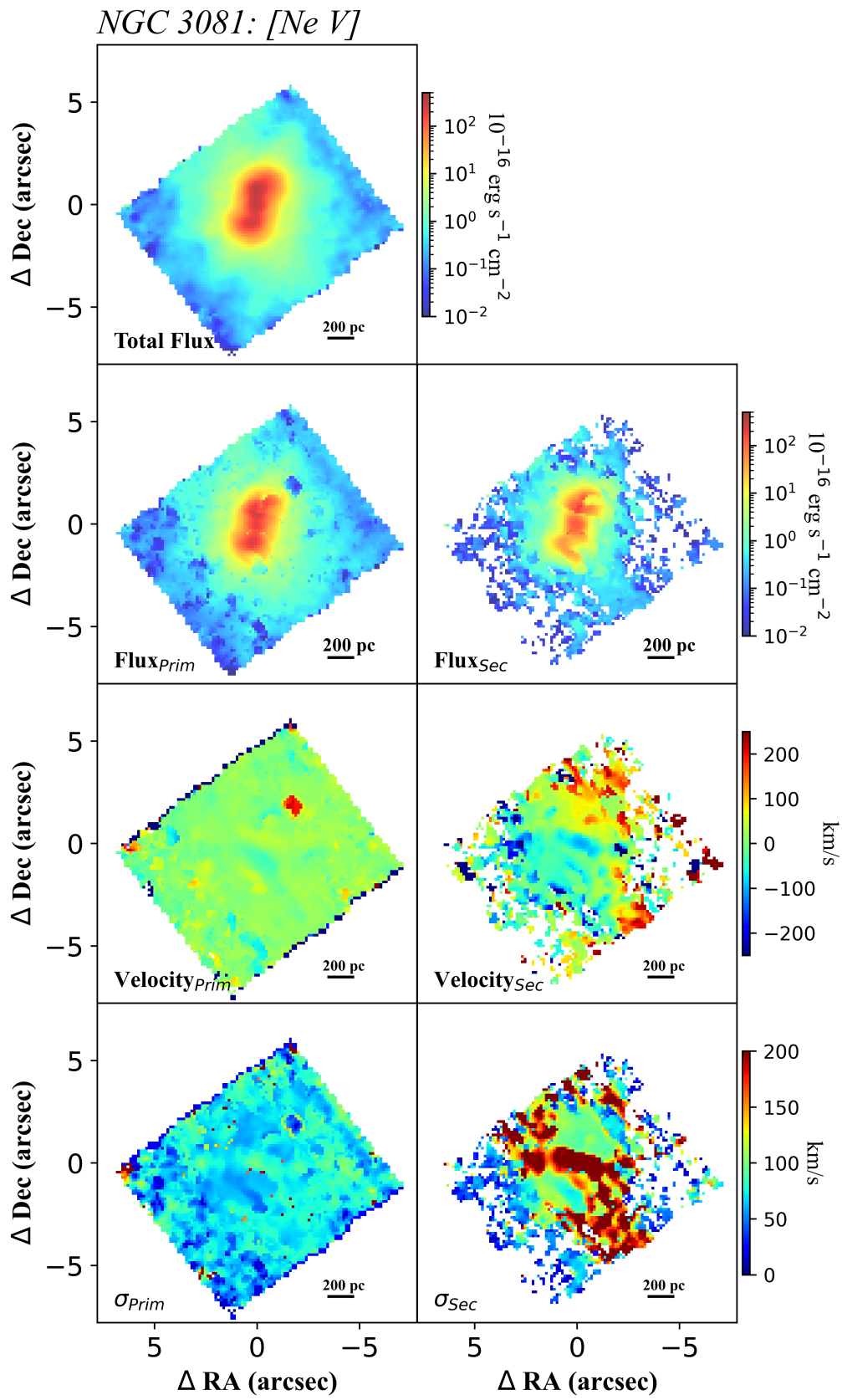

Figure A10. Flux distribution and kinematics for NGC 3081 [Ne V]$_{14.322\mu m}$ emission. The left column presents the primary/rotational component for the two-component fit, and the right column presents the secondary/outflowing fit component.

A.2. NGC 5506 Additional Line Maps

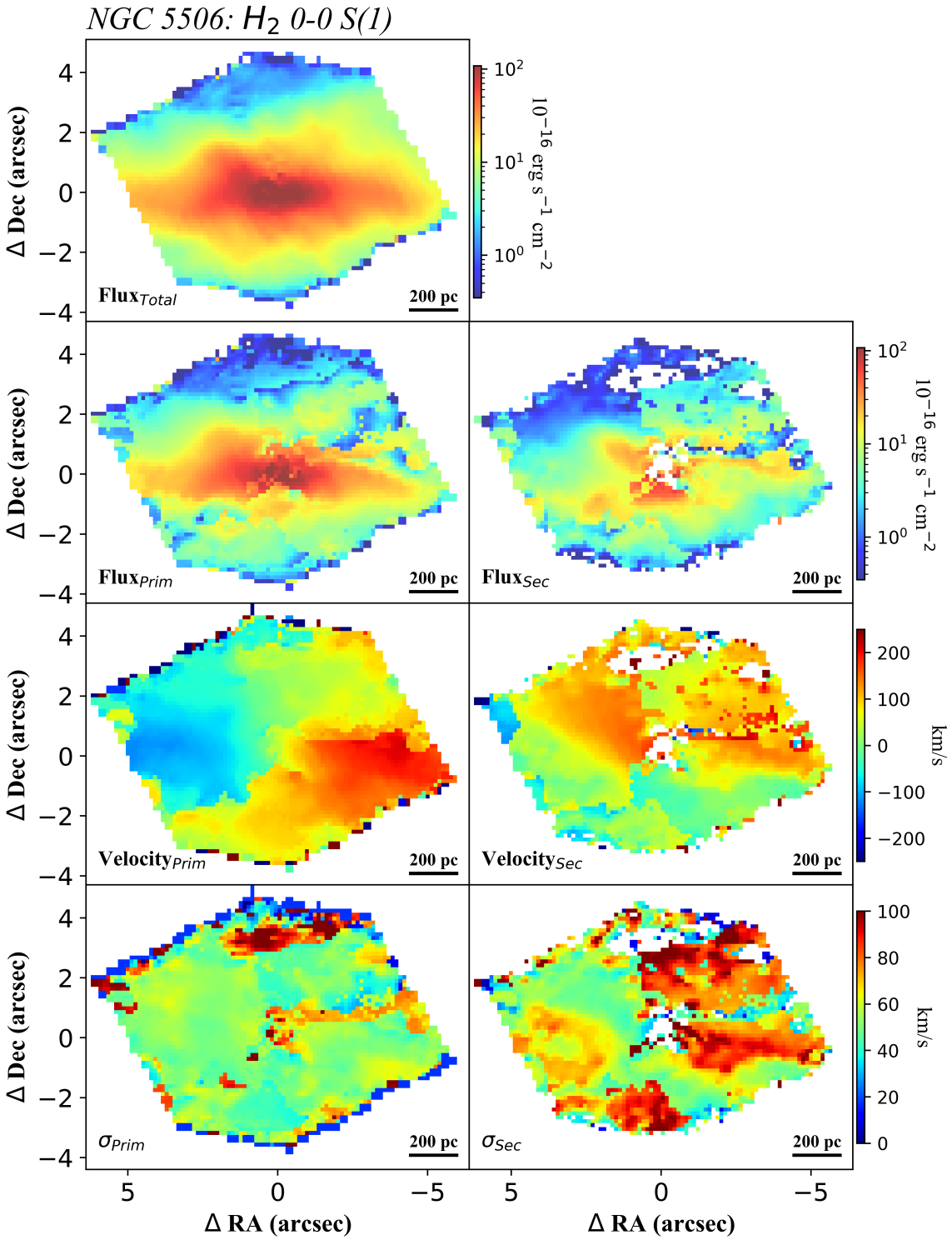

Figure A11. Flux distribution and kinematics for NGC 5506 H_2 0–0 S(1) emission. The left column presents the primary/rotational component for the two-component fit, and the right column presents the secondary/outflowing fit component.

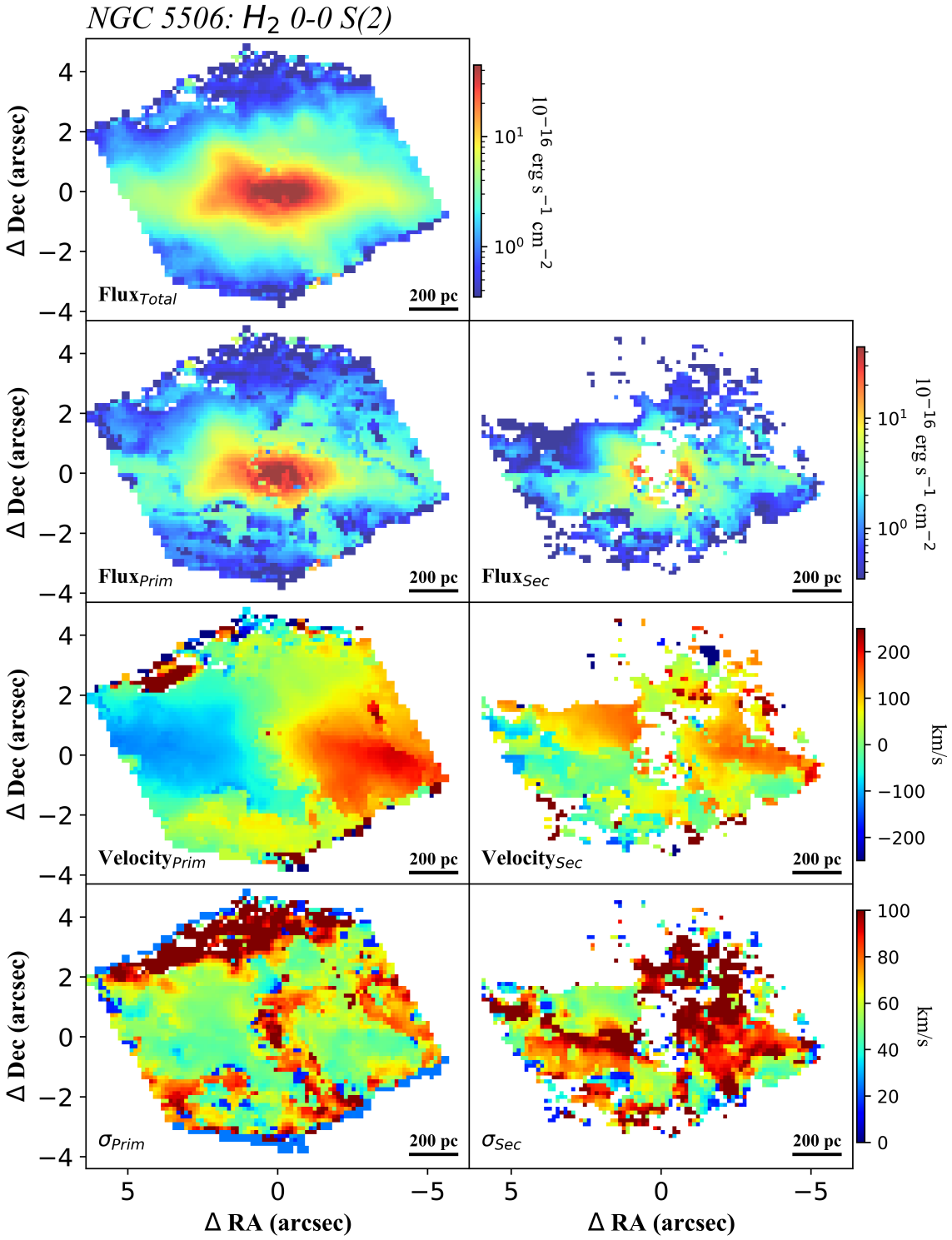

Figure A12. Flux distribution and kinematics for NGC 5506 H_2 0–0 S(2) emission. The left column presents the primary/rotational component for the two-component fit, and the right column presents the secondary/outflowing fit component.

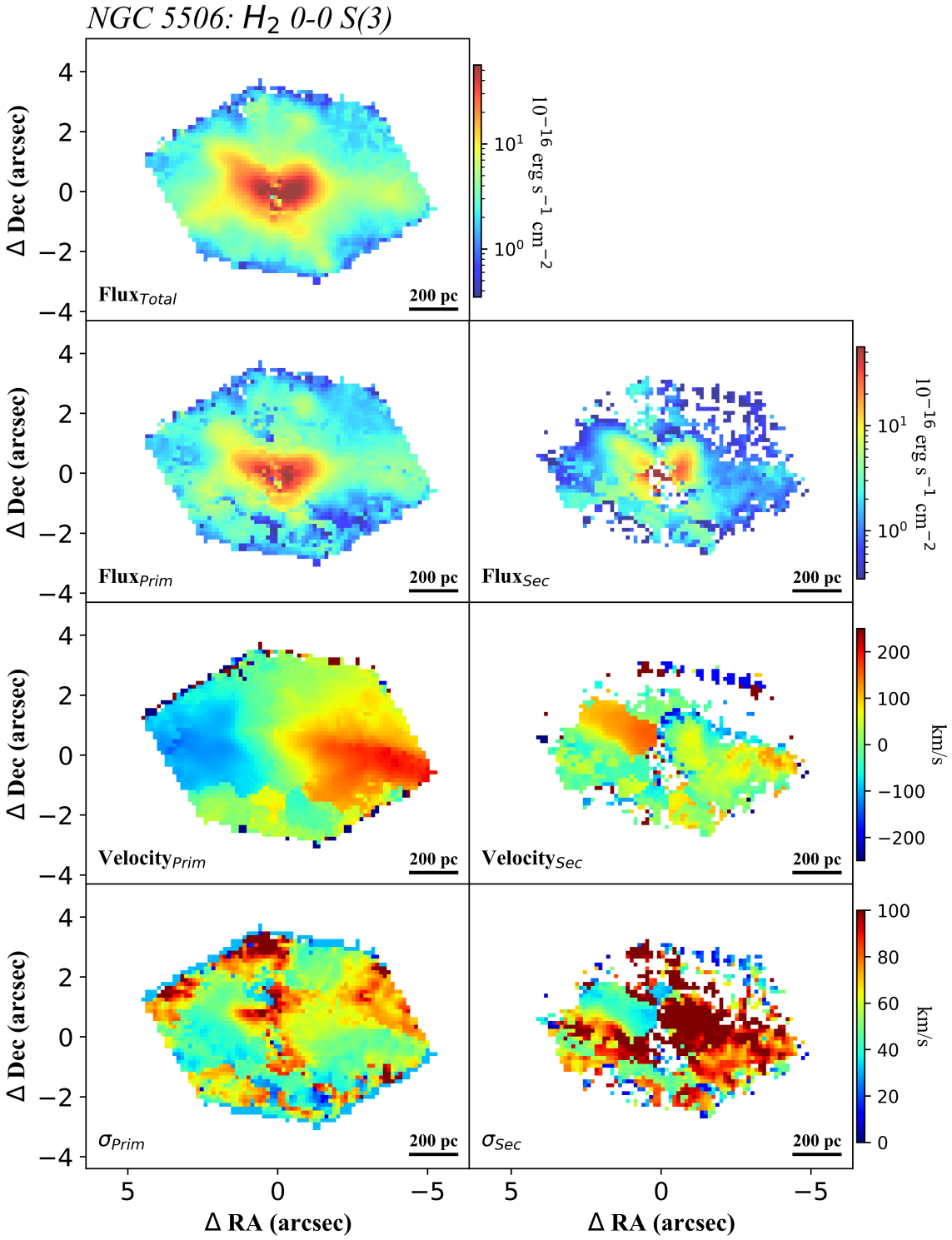

Figure A13. Flux distribution and kinematics for NGC 5506 H_2 0–0 S(3) emission. The left column presents the primary/rotational component for the two-component fit, and the right column presents the secondary/outflowing fit component.

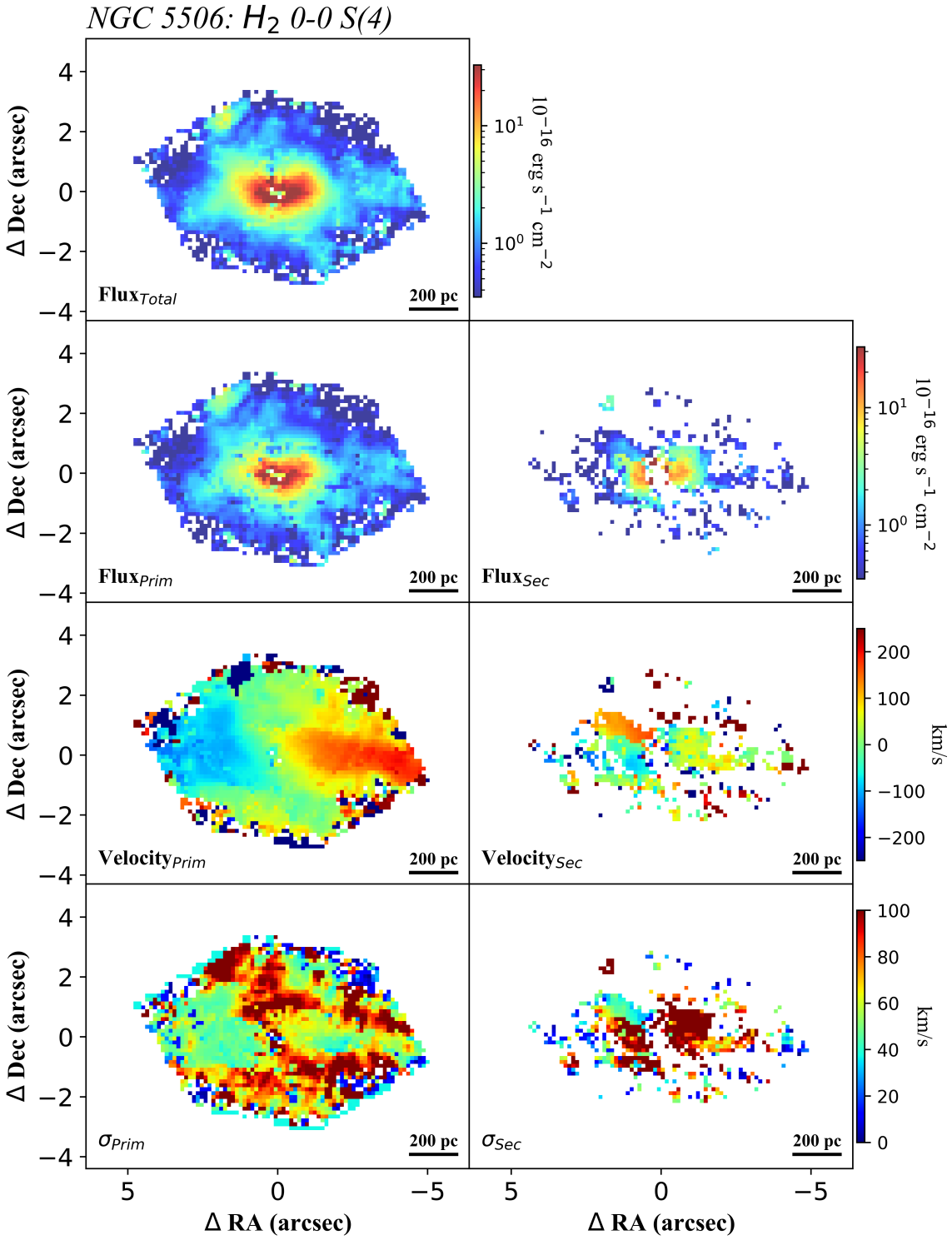

Figure A14. Flux distribution and kinematics for NGC 5506 H_2 0–0 S(4) emission. The left column presents the primary/rotational component for the two-component fit, and the right column presents the secondary/outflowing fit component.

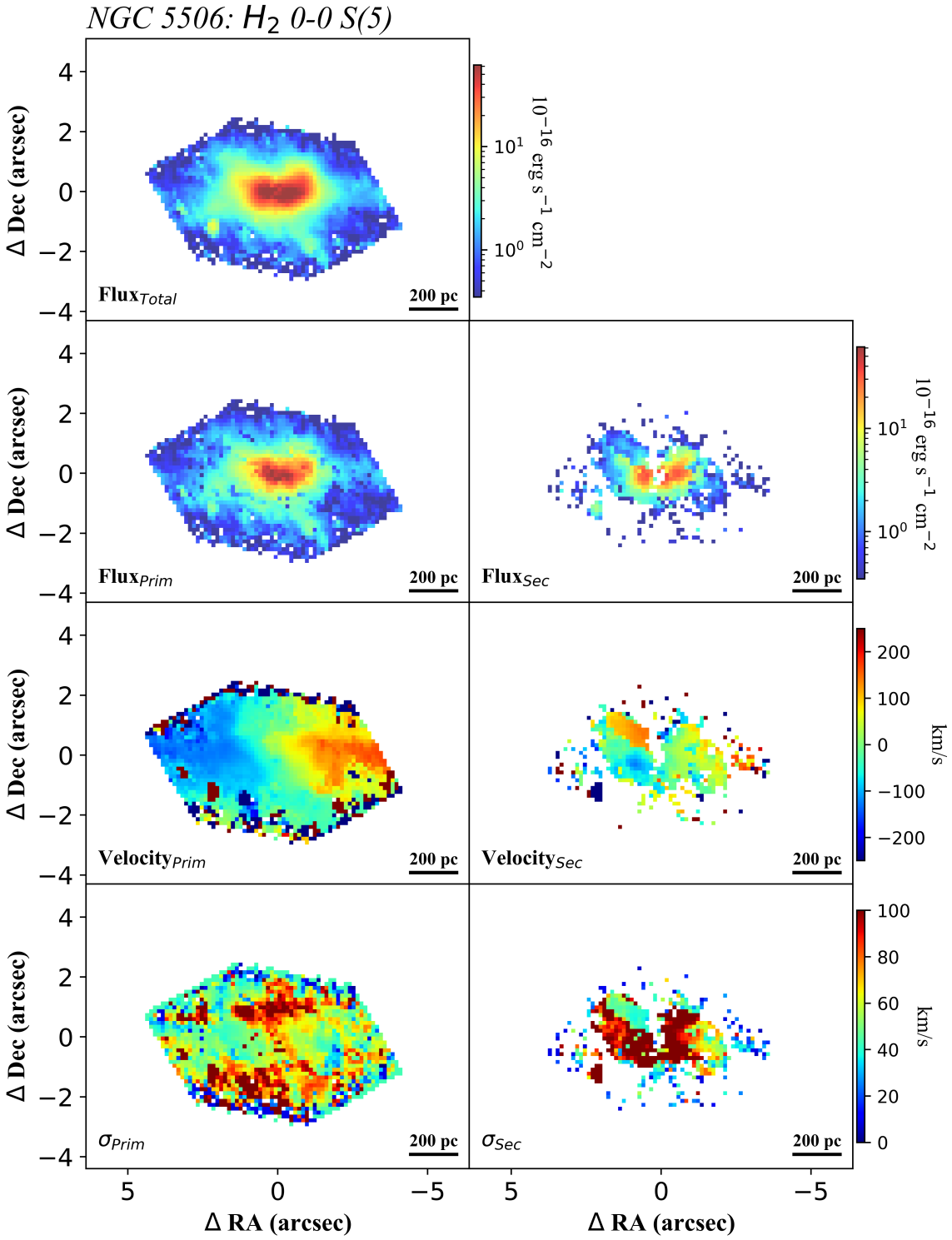

Figure A15. Flux distribution and kinematics for NGC 5506 H_2 0–0 S(5) emission. The left column presents the primary/rotational component for the two-component fit, and the right column presents the secondary/outflowing fit component.

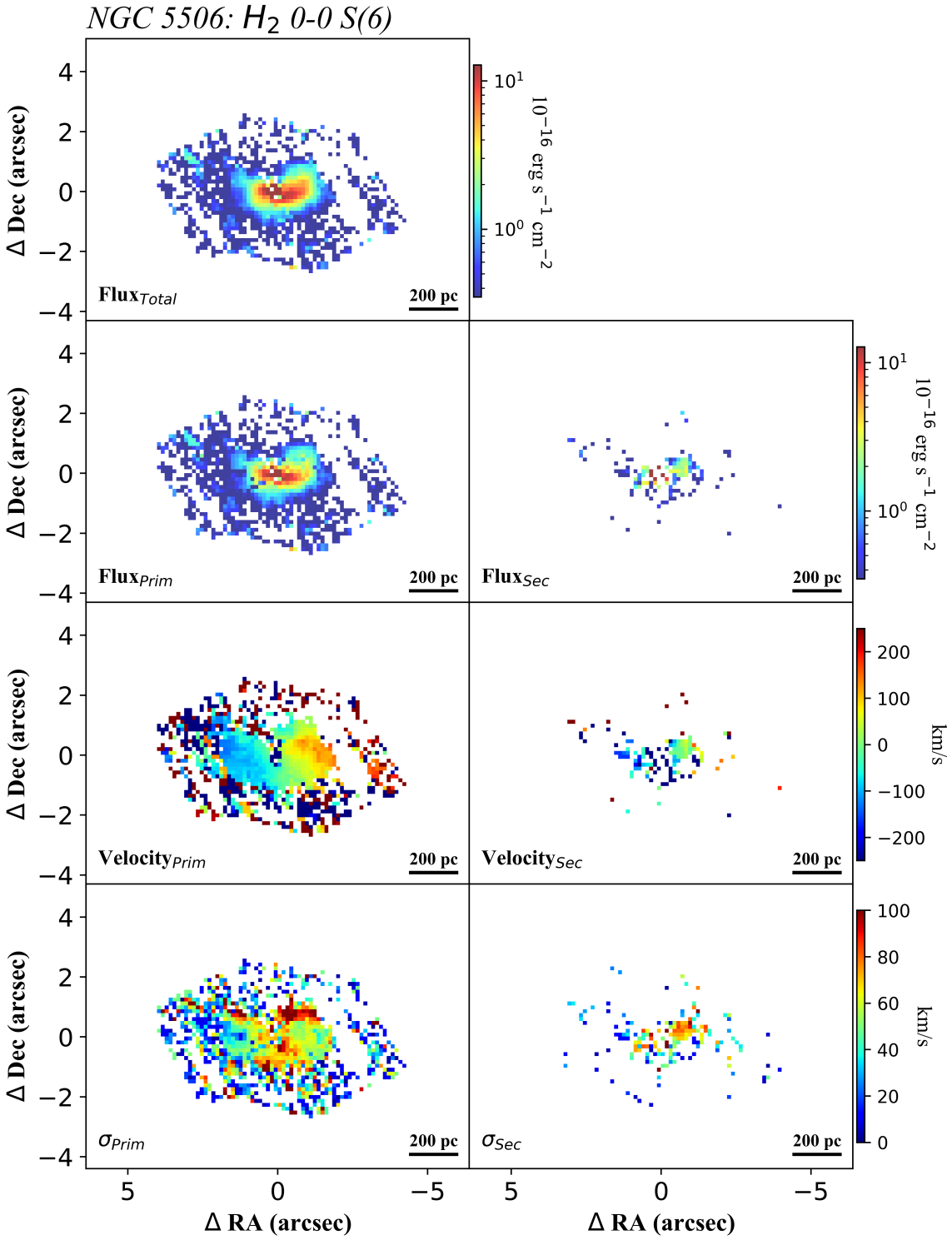

Figure A16. Flux distribution and kinematics for NGC 5506 H_2 0–0 S(6) emission. The left column presents the primary/rotational component for the two-component fit, and the right column presents the secondary/outflowing fit component.

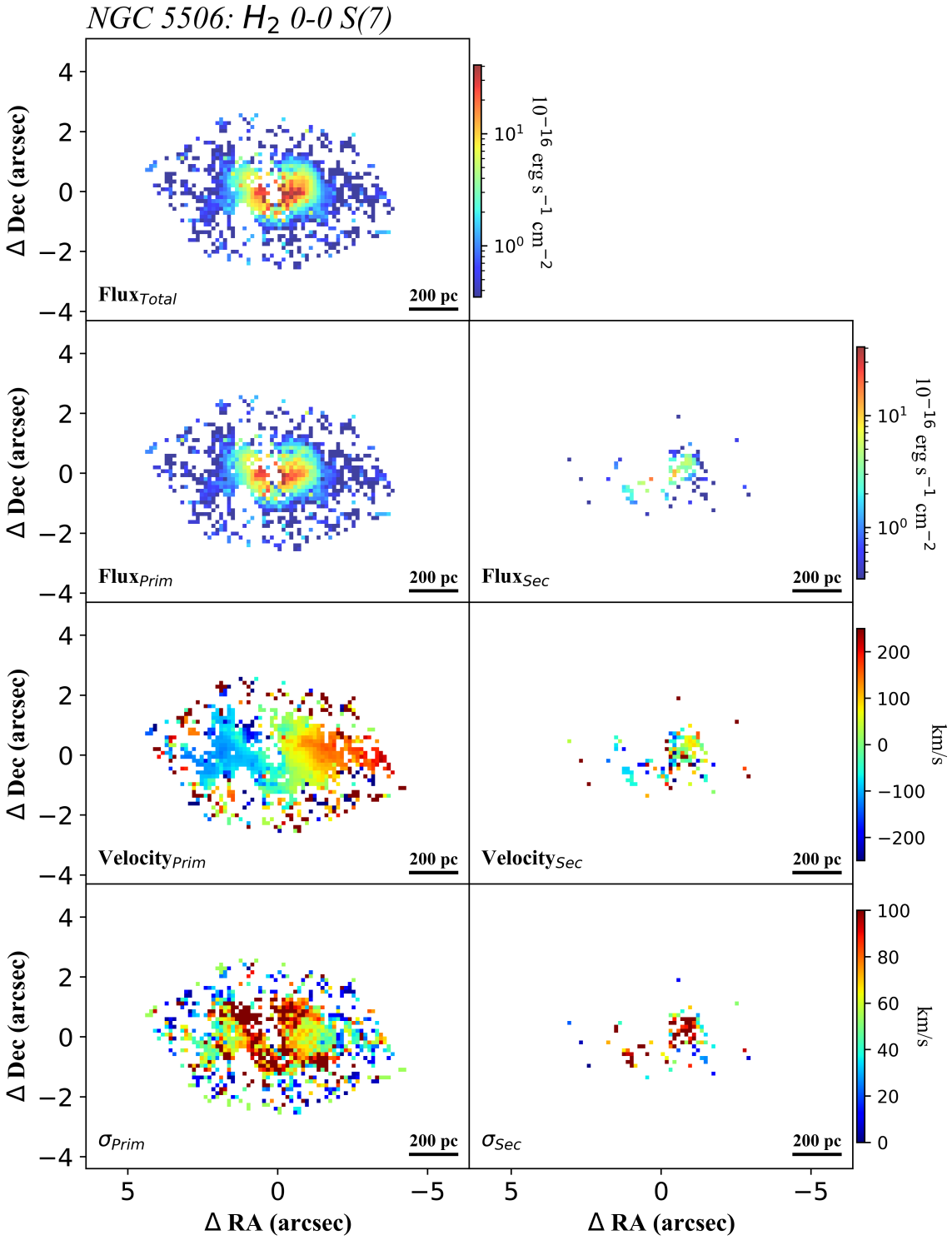

Figure A17. Flux distribution and kinematics for NGC 5506 H_2 0–0 S(7) emission. The left column presents the primary/rotational component for the two-component fit, and the right column presents the secondary/outflowing fit component.

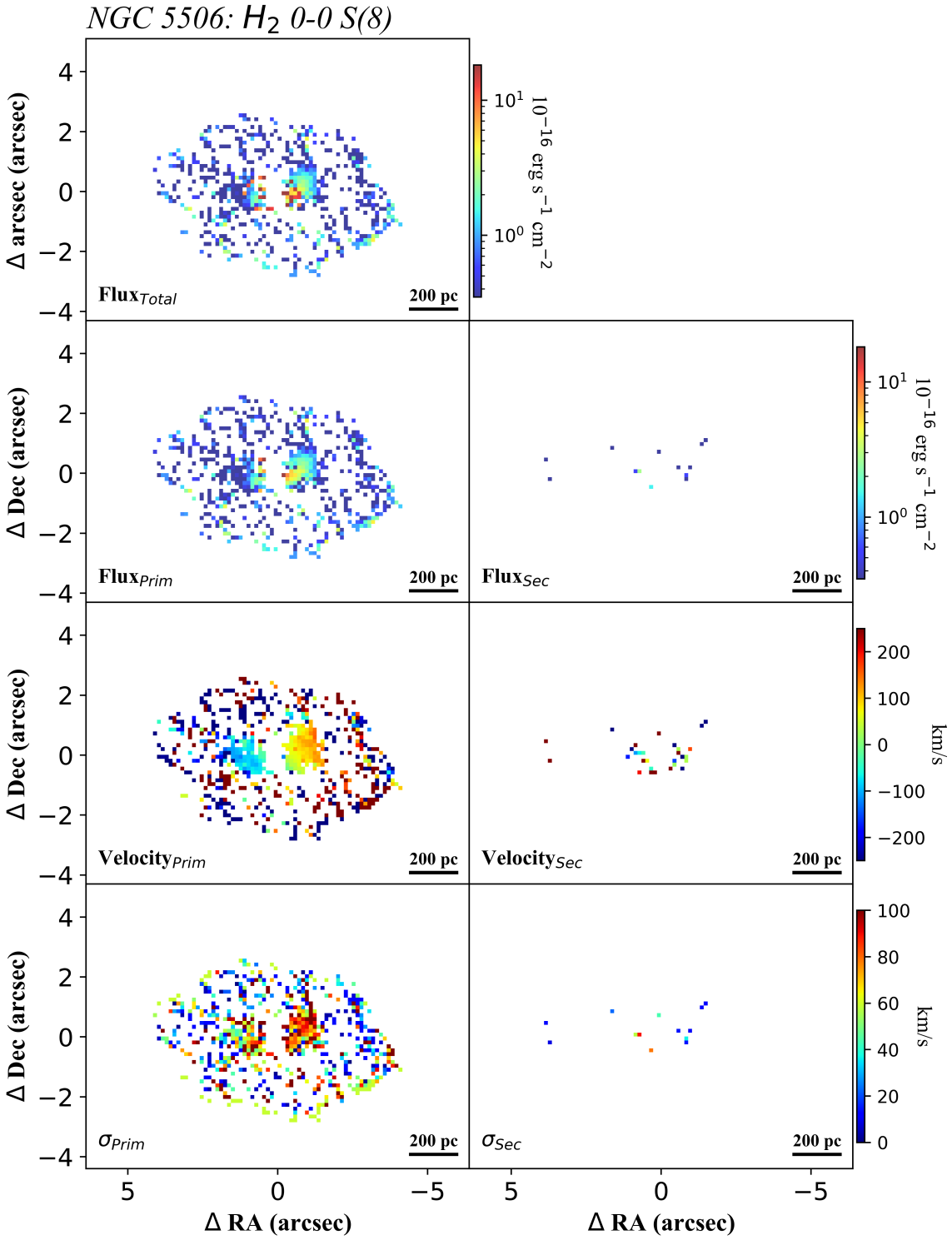

Figure A18. Flux distribution and kinematics for NGC 5506 H_2 0–0 S(8) emission. The left column presents the primary/rotational component for the two-component fit, and the right column presents the secondary/outflowing fit component.

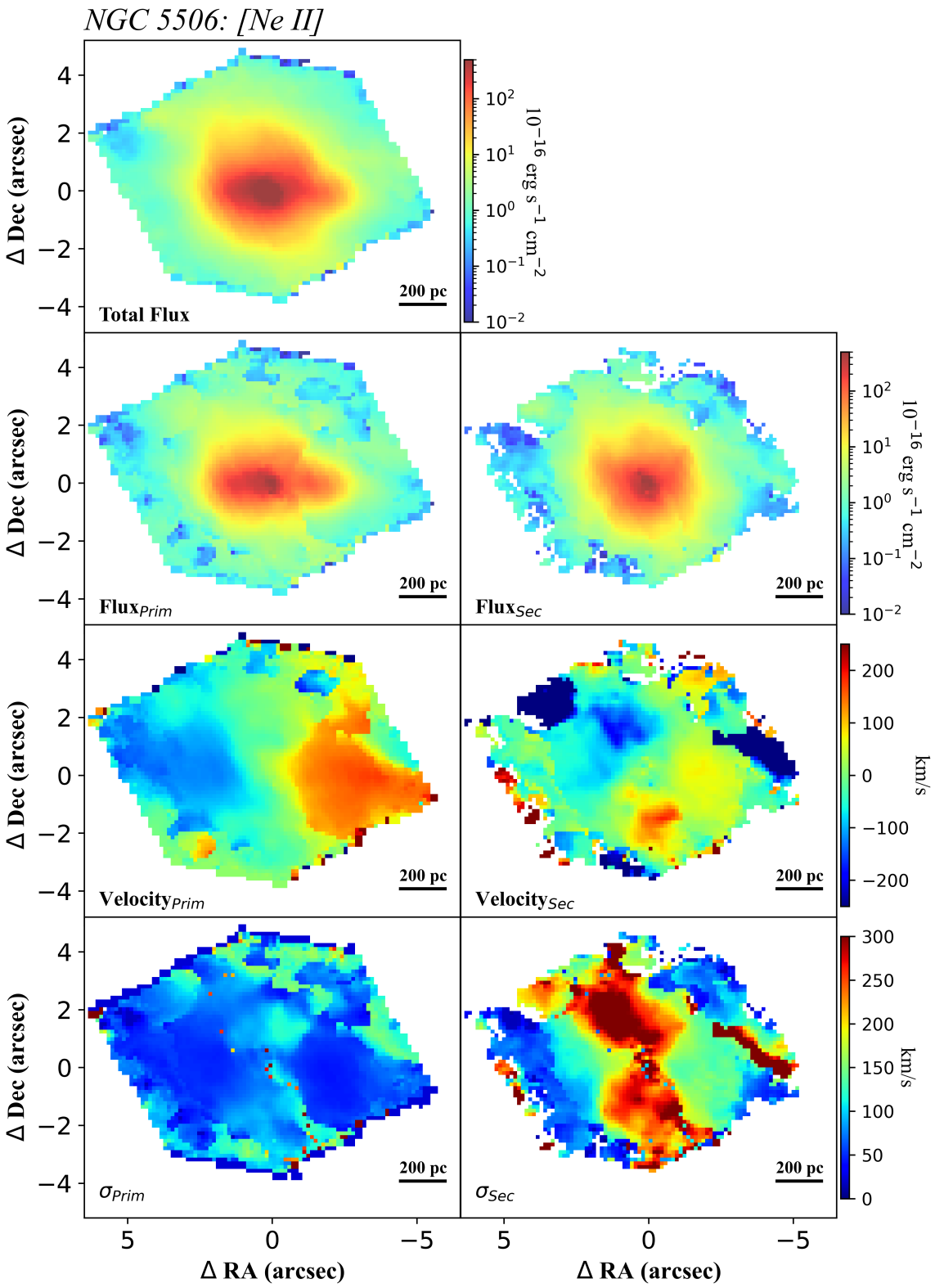

Figure A19. Flux distribution and kinematics for NGC 5506 [Ne II]$_{12.814\mu m}$ emission. The left column presents the primary/rotational component for the two-component fit, and the right column presents the secondary/outflowing fit component.

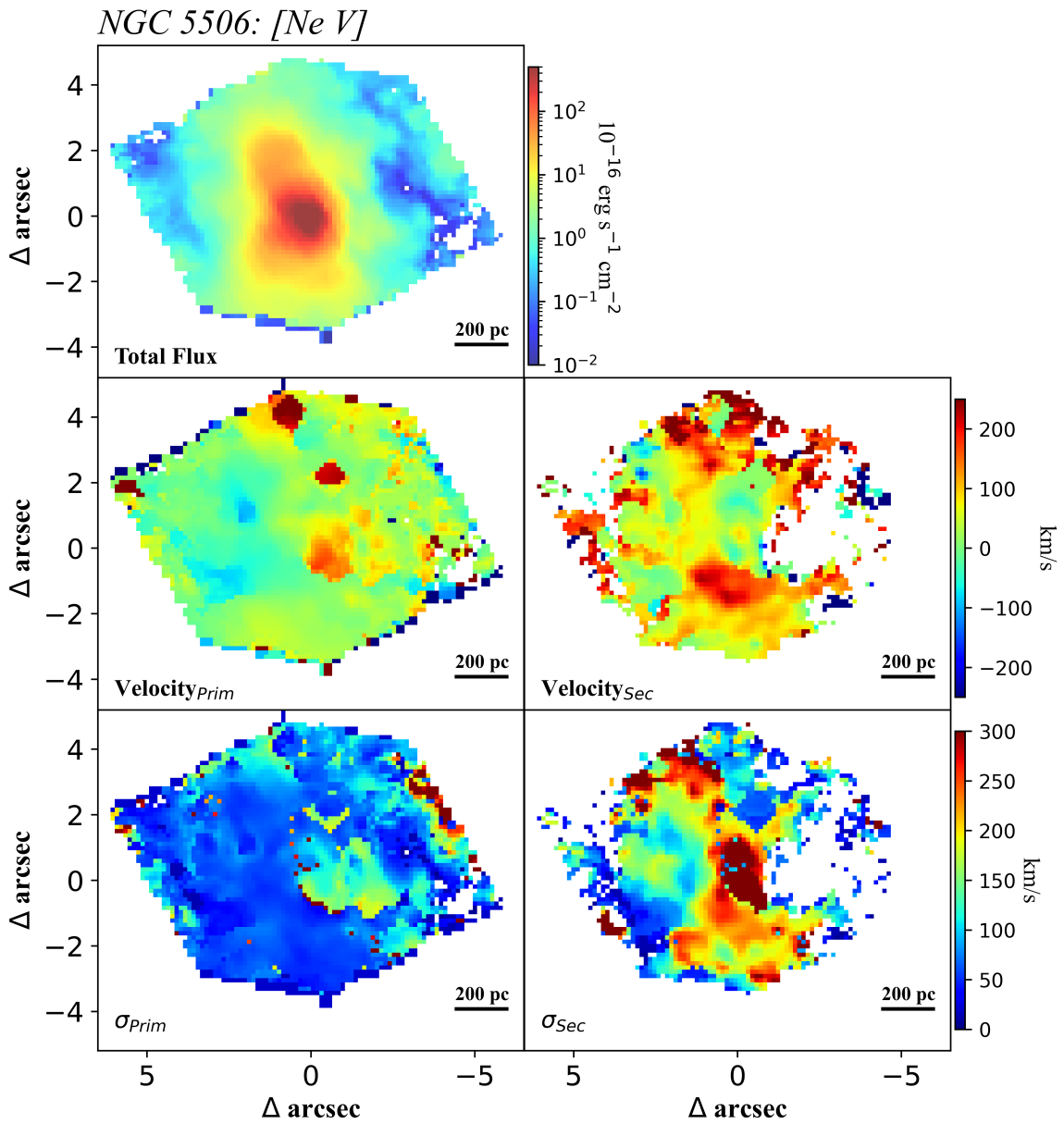

Figure A20. Flux distribution and kinematics for NGC 5506 $[\mathrm{Ne\ V}]_{14.322\mu m}$ emission. The left column presents the primary/rotational component for the two-component fit, and the right column presents the secondary/outflowing fit component.

ORCID iDs

Daniel E. Delaney https://orcid.org/0009-0007-6992-2555
Erin K. S. Hicks https://orcid.org/0000-0002-4457-5733
Lulu Zhang https://orcid.org/0000-0003-4937-9077
Chris Packham https://orcid.org/0000-0001-7827-5758
Ric Davies https://orcid.org/0000-0003-4949-7217
Miguel Pereira Santaella https://orcid.org/0000-0002-4005-9619
Enrica Bellocchi https://orcid.org/0000-0001-9791-4228
Nancy A. Levenson https://orcid.org/0000-0003-4209-639X
Steph Campbell https://orcid.org/0000-0001-9520-7765
David J. Rosario https://orcid.org/0000-0002-0001-3587
Houda Haidar https://orcid.org/0000-0002-3741-6136
Cristina Ramos Almeida https://orcid.org/0000-0001-8353-649X
Anelise Audibert https://orcid.org/0000-0003-3589-3294
Claudio Ricci https://orcid.org/0000-0001-5231-2645
Laura Hermosa Muñoz https://orcid.org/0000-0002-9610-0123
Francoise Combes https://orcid.org/0000-0003-2658-7893
Almudena Alonso-Herrero https://orcid.org/0000-0001-6794-2519
Santiago García-Burillo https://orcid.org/0000-0003-0444-6897
Federico Esposito https://orcid.org/0000-0002-5775-6285
Ismael García-Bernete https://orcid.org/0000-0002-9627-5281
Taro Shimizu https://orcid.org/0000-0002-2125-4670
Martin Ward https://orcid.org/0000-0003-1810-0889
Omaira Gonzalez Martin https://orcid.org/0000-0002-2356-8358

Alvaro Labiano https://orcid.org/0000-0002-0690-8824
Enrique Lopez-Rodriguez https://orcid.org/0000-0001-5357-6538
Dimitra Rigopoulou https://orcid.org/0000-0001-6854-7545
Marko Stalevski https://orcid.org/0000-0001-5146-8330
Sebastian F. Hönig https://orcid.org/0000-0002-6353-1111
Donaji Esparza-Arredondo https://orcid.org/0000-0001-8042-9867
Takuma Izumi https://orcid.org/0000-0001-9452-0813
Lindsay Fuller https://orcid.org/0000-0003-4809-6147

References

Abuter, R., Schreiber, J., Eisenhauer, F., et al. 2006, NewAR, 50, 398
Alonso-Herrero, A., García-Burillo, S., Pereira-Santaella, M., et al. 2019, A&A, 628, A65
Alonso-Herrero, A. A., García-Burillo, S., Pereira-Santaella, M., et al. 2023, A&A, 675, A88
Argyriou, I., Glasse, A., Law, D. R., et al. 2023, A&A, 675, A111
Audibert, A., Almeida, C. R., García-Burillo, S., et al. 2023, A&A, 671, L12
Audibert, A., Almeida, C. R., García-Burillo, S., et al. 2025, A&A, 699, A83
Baldovin-Saavedra, C., Audard, M., Carmona, A., et al. 2012, A&A, 543, A30
Baumgartner, W., Tueller, J., Markwardt, C., et al. 2013, ApJS, 207, 19
Bessiere, P. S., & Ramos Almeida, C. 2022, MNRAS: Letters, 512, L54
Bianchin, M., Riffel, R. A., Storchi-Bergmann, T., et al. 2022, MNRAS, 510, 639
Bigiel, F., Leroy, A., Walter, F., et al. 2011, ApJL, 730, L13
Bohn, T., Inami, H., Togi, A., et al. 2024, ApJ, 977, 36
Burton, M. G., Hollenbach, D., & Tielens, A. 1992, ApJ, 399, 563
Buta, R., & Purcell, G. B. 1998, AJ, 115, 484
Buta, R. J., Byrd, G. G., & Freeman, T. 2004, AJ, 127, 1982
Caglar, T., Burtscher, L., Brandl, B., et al. 2020, A&A, 634, A114
Cicone, C., Maiolino, R., Sturm, E., et al. 2014, A&A, 562, A21
Cleri, N. J., Yang, G., Papovich, C., et al. 2023, ApJ, 948, 112
Davies, R. 2007, MNRAS, 375, 1099
Davies, R., Baron, D., Shimizu, T., et al. 2020, MNRAS, 498, 4150
Davies, R., Maciejewski, W., Hicks, E., et al. 2014, ApJ, 792, 101
Davies, R., Sánchez, F. M., Genzel, R., et al. 2007, ApJ, 671, 1388
Davies, R., Shimizu, T., Pereira-Santaella, M., et al. 2024, A&A, 689, A263
Davies, R. I., Sternberg, A., Lehnert, M., & Tacconi-Garman, L. 2005, ApJ, 633, 105
Dickman, R., Snell, R. L., Schloerb, F. P., et al. 1986, ApJ, 309, 326
Eguchi, S., Ueda, Y., Awaki, H., et al. 2011, ApJ, 729, 31
Eisenhauer, F., Abuter, R., Bickert, K., et al. 2003, Proc. SPIE, 4841, 1548
Ellison, S. L., Sánchez, S. F., Ibarra-Medel, H., et al. 2018, MNRAS, 474, 2039
Esparza-Arredondo, D., Almeida, C. R., Audibert, A., et al. 2025, A&A, 693, A174
Esposito, F., Alonso-Herrero, A., García-Burillo, S., et al. 2024, A&A, 686, A46
Esquej, P., Alonso-Herrero, A., González-Martín, O., et al. 2013, ApJ, 780, 86
Fabian, A. C. 2012, ARA&A, 50, 455
Ferruit, P., Wilson, A. S., & Mulchaey, J. 2000, ApJS, 128, 139
Fischer, T., Crenshaw, D., Kraemer, S., & Schmitt, H. 2013, ApJS, 209, 1
Fritz, T. K., Gillessen, S., Dodds-Eden, K., et al. 2011, ApJ, 737, 73
Gallimore, J. F., Elitzur, M., Maiolino, R., et al. 2016, ApJL, 829, L7
García-Bernete, I., Alonso-Herrero, A., García-Burillo, S., et al. 2021, A&A, 645, A21
García-Bernete, I., Alonso-Herrero, A., Rigopoulou, D., et al. 2024, A&A, 681, L7
García-Bernete, I., Ramos Almeida, C., Landt, H., et al. 2017, MNRAS, 469, 110
García-Bernete, I., Rigopoulou, D., Alonso-Herrero, A., et al. 2022, A&A, 666, L5
García-Burillo, S., Alonso-Herrero, A., Almeida, C. R., et al. 2021, A&A, 652, A98
García-Burillo, S., Combes, F., Almeida, C. R., et al. 2016, ApJL, 823, L12
García-Burillo, S., Combes, F., Almeida, C. R., et al. 2019, A&A, 632, A61
García-Burillo, S., Combes, F., Usero, A., et al. 2014, A&A, 567, A125
García-Burillo, S., Hicks, E., Alonso-Herrero, A., et al. 2024, A&A, 689, A347
Gardner, J. P., Mather, J. C., Abbott, R., et al. 2023, PASP, 135, 068001
Glassgold, A. E., Najita, J. R., & Igea, J. 2007, ApJ, 656, 515
Gofford, J., Reeves, J., McLaughlin, D., et al. 2015, MNRAS, 451, 4169
Haidar, H., Rosario, D. J., Alonso-Herrero, A., et al. 2024, MNRAS, 532, 4645
Harrison, C. 2017, NatAs, 1, 0165
Harrison, C., Costa, T., Tadhunter, C., et al. 2018, NatAs, 2, 198
Harrison, C. M., & Ramos Almeida, C. 2024, Galax, 12, 17
Herbst, T., Beckwith, S., Glindemann, A., et al. 1996, AJ, 111, 2403
Hermosa-Muñoz, L., Alonso-Herrero, A., Pereira-Santaella, M., et al. 2024, A&A, 690, A350
Hickox, R. C., & Alexander, D. M. 2018, ARA&A, 56, 625
Holden, L. R., Tadhunter, C., Audibert, A., et al. 2024, MNRAS, 530, 446
Holden, L. R., Tadhunter, C. N., Morganti, R., & Oosterloo, T. 2023, MNRAS, 520, 1848
Hollenbach, D., & Gorti, U. 2009, ApJ, 703, 1203
Hummer, D., & Storey, P. 1987, MNRAS, 224, 801
Imanishi, M., Nakanishi, K., Izumi, T., & Wada, K. 2018, ApJL, 853, L25
Impellizzeri, C. V., Gallimore, J. F., Baum, S. A., et al. 2019, ApJL, 884, L28
Izotov, Y. I., Thuan, T., & Privon, G. 2012, MNRAS, 427, 1229
Kinney, A., Schmitt, H., Clarke, C., et al. 2000, ApJ, 537, 152
Koo, B.-C., Raymond, J. C., & Kim, H.-J. 2016, JKAS, 49, 109
Kristensen, L., Godard, B., Guillard, P., Gusdorf, A., & Des Forêts, G. P. 2023, A&A, 675, A86
Lien, A. Y., Krimm, H., Markwardt, C., et al. 2025, ApJ, 989, 161
Maiolino, R., Stanga, R., Salvati, M., & Rodriguez Espinosa, J. 1994, A&A, 290, 40
Molina, J., Ho, L. C., Wang, R., et al. 2023, ApJ, 944, 30
Morganti, R., Tsvetanov, Z., Gallimore, J., & Allen, M. 1999, A&AS, 137, 457
Mutie, I. M., Williams-Baldwin, D., Beswick, R. J., et al. 2024, MNRAS, 527, 11756
Nagar, N. M., Wilson, A. S., Mulchaey, J. S., & Gallimore, J. F. 1999, ApJS, 120, 209
Napier, P. J., Thompson, A. R., & Ekers, R. D. 1983, IEEEP, 71, 1295
Peralta de Arriba, L., Alonso-Herrero, A., García-Burillo, S., et al. 2023, A&A, 675, A58
Pereira-Santaella, M., Álvarez-Márquez, J., García-Bernete, I., et al. 2022, A&A, 665, L11
Pereira-Santaella, M., Spinoglio, L., van der Werf, P. P., & López, J. P. 2014, A&A, 566, A49
Ramos Almeida, C., Bischetti, M., García-Burillo, S., et al. 2022, A&A, 658, A155
Ramos Almeida, C., Garcia-Bernete, I., Pereira-Santaella, M., et al. 2025, A&A, 698, A194
Ramos Almeida, C., & Ricci, C. 2017, NatAs, 1, 679
Ricci, C., Trakhtenbrot, B., Koss, M. J., et al. 2017, ApJS, 233, 17
Rieke, G. H., Wright, G., Böker, T., et al. 2015, PASP, 127, 584
Riffel, R. A., Souza-Oliveira, G. L., Costa-Souza, J. H., et al. 2025, ApJ, 982, 69
Riffel, R. A., Souza-Oliveira, G. L., Costa-Souza, J. H., et al. 2025, ApJ, 982, 69
Riffel, R. A., Storchi-Bergmann, T., Riffel, R., et al. 2023, MNRAS, 521, 1832
Rigby, J., Perrin, M., McElwain, M., et al. 2023, PASP, 135, 048001
Robitaille, T. P., Tollerud, E. J., Greenfield, P., et al. 2013, A&A, 558, A33
Rodríguez-Ardila, A., Fonseca-Faria, M., Dahmer-Hahn, L., et al. 2025, MNRAS, 538, 2800
Rosario, D., Burtscher, L., Davies, R. I., et al. 2018, MNRAS, 473, 5658
Roussel, H., Helou, G., Hollenbach, D., et al. 2007, ApJ, 669, 959
Roy, A., Wrobel, J., Wilson, A., et al. 2001, in IAU Symp. 205, Galaxies and their Constituents at the Highest Angular Resolutions, ed. R. T. Schilizzi (Cambridge: Cambridge Univ. Press), 70
Ruiz, J., Crenshaw, D., Kraemer, S., et al. 2005, AJ, 129, 73
Salomé, Q., Krongold, Y., Longinotti, A. L., et al. 2023, MNRAS, 524, 3130
Sarkar, K. C. 2024, A&ARv, 32, 1
Schmitt, H., Ulvestad, J., Antonucci, R., & Kinney, A. 2001, ApJS, 132, 199
Schnorr-Müller, A., Storchi-Bergmann, T., Robinson, A., Lena, D., & Nagar, N. M. 2016, MNRAS, 457, 972
Shang, H., Glassgold, A. E., Lin, W.-C., & Liu, C.-F. J. 2010, ApJ, 714, 1733
Tarchi, A., Castangia, P., Columbano, A., Panessa, F., & Braatz, J. 2011, A&A, 532, A125
Thompson, A. R., Moran, J. M., & Swenson, G. W. 1980, Interferometry and Synthesis in Radio Astronomy (1st ed.; New York: Wiley)

Togi, A., & Smith, J. 2016, ApJ, 830, 18
Ueda, Y., Eguchi, S., Terashima, Y., et al. 2007, ApJL, 664, L79
Van der Tak, F., Black, J. H., Schöier, F., Jansen, D., & Van Dishoeck, E. F. 2007, A&A, 468, 627
Veilleux, S., Cecil, G., & Bland-Hawthorn, J. 2005, ARA&A, 43, 769
Veilleux, S., Meléndez, M., Sturm, E., et al. 2013, ApJ, 776, 27
Véron-Cetty, M.-P., & Véron, P. 2006, A&A, 455, 773
Wada, K. 2012, ApJ, 758, 66
Wells, M., Pel, J.-W., Glasse, A., et al. 2015, PASP, 127, 646
Yang, H.-Y. K., Ruszkowski, M., & Zweibel, E. G. 2022, NatAs, 6, 584
Zakamska, N. L. 2010, Natur, 465, 60
Zeimann, G. R., Ciardullo, R., Gebhardt, H., et al. 2014, ApJ, 798, 29
Zhang, L., García-Bernete, I., Packham, C., et al. 2024a, ApJL, 975, L2
Zhang, L., & Ho, L. C. 2023, ApJL, 953, L9
Zhang, L., Packham, C., Hicks, E. K., et al. 2024b, ApJ, 974, 195
Zhuang, M.-Y., Ho, L. C., & Shangguan, J. 2019, ApJ, 873, 103